Investigation of Dual Three-Phase IPMSM

Analyzing PWM Strategies' Impact on Common Mode Voltage Reduction

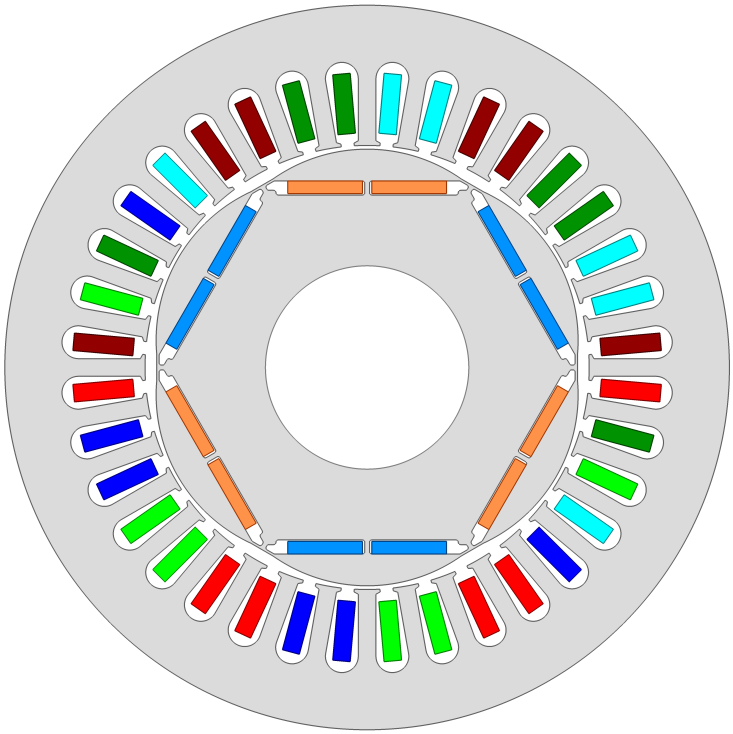

Master's Thesis

Aalborg University
AAU Energy

Summary

Grundfos is a Danish pump manufacturer that searches to use two inverters to control a IPMSM for potential cost savings on hardware development. In addition, the literature suggests that using two inverters may include the benefit of being able to reduce CM voltage. This is of interest, as CM voltage can be a main source of bearing currents, which can decrease the lifetime, performance and reliability of the machine.

The focus of this thesis is the machine model of a Dual-Three-Phase IPMSM, parameters determination, FOC implementation and CM voltage reducing PWM strategies. A machine model describing the inductances in such machine is outlined and the model is validated by inductance measurements and FEA simulation. The measurements and FEA simulation share the same characteristics and the parameters from the measurements was chosen as machine parameters. The machine model had to be validated and FOC was chosen as operation implementation. First, FOC was validated in a Simulink model and then it was deployed on the test bench setup. The simulation and implementation had to fulfill the same test criteria and was tested in steady state and under a dynamic speed ramp, as well as a load step. Both the simulation and experimental results passed the test criteria and show equivalent characteristics and therefore the machine model and FOC implementation is validated.

The investigation into CM voltage starts by outlining what CM voltage is and how it appears in a DTP machine. Then three PWM schemes are tested: synchronized SVM, interleaved SVM, and Zero CMV (ZCMV). The simulations show that SVM generates to highest amount of CM voltage, which aligns with the theory. The interleaved SVM showed a reduced amount of CM voltage, with pulses of $\pm V_{dc}/6$. Lastly, the ZCMV strategy shows eliminated CM voltage when simulated under ideal conditions. When different dead times was included in the simulation, this strategy showed CM voltage pulses with amplitude of $\pm V_{dc}/6$ and are dependent of the dead time duration. The alignment of opposite polarity pulse edges is critical for ZCMV, as the method uses inverter pulse cancellation to reduce CM voltage.Experimental measurements on the test bench highlighted some synchronization issues between the inverters. Furthermore, some current balancing issues between the inverters was also observed, which is mentioned the literature to be a common challenge. No CM voltage reducing strategy was implemented on the test setup, but some measurements of the CM voltage and the leakage current was performed. Clearly, both phenomenons were present in the prototype under operation. The future work involves implementing the PWM strategies to investigate if CM voltage is reduced on the experimental setup.

AAU Energy
Aalborg University
http://www.aau.dk

AALBORG UNIVERSITY
STUDENT REPORT

Title:
Investigation of Dual Three-Phase IPMSM

Theme:
Electric Motor Control

Project Period:
Spring Semester 2024

Project Group:
MSc PED4-1047

Participant(s):
Magnus Borg Wissing
Viktor Ferm

Supervisor(s):
Kaiyuan Lu

Copies: 1

Page Numbers: 88

Date of Completion:
May 31, 2024

Abstract:

This thesis investigates a DTP machine controlled by a dual inverter setup for potential CM voltage reduction. The machine parameters is validated by FEA simulation and experimental measurements. The machine is operated using FOC in Simulink and on a test bench setup. The machine model and operation is validated by comparing the simulation and measured results. Three PWM schemes are explored: SVM, interleaving SVM and ZCMV. The ZCMV shows a theoretical elimination of CM voltage. When implementing dead time in the simulation ZCMV shows pulses, that are dependent of dead time duration. Future work includes implementing the three strategies experimentally to verify if the CM voltage reduction is present on the physical machine using ZCMV.

The content of this report is freely available, but publication (with reference) may only be pursued due to agreement with the author.

Nomenclature

Acronyms

abc abc reference frame

back EMF back Electromotive Force

CM Common Mode

dq direct-quadrature reference frame

DTP Dual-Three-Phase

FEA Finite Element Analysis

FOC Field Oriented Control

HF High Frequency

IPMSM Interior-Mounted Permanent Magnet Synchronous Machine

MTP Multiple-Three-Phase

PM Permanent Magnet

SPMSM Surface-Mounted Permanent Magnet Synchronous Machine

SPWM Sinusoidal Pulse Width Modulation

SVM Space Vector Modulation

VSI Voltage Source Inverter

ZCMV Zero Common Mode Voltage

Contents

Preface

When citing literature or other material, hard brackets are used, i.e., [10] for the 10th entry in the bibliography. A cross-reference is denoted by chapter number followed by the section number, i.e., 4.2 for Chapter four, Section two. Similarly, an equation, table or figure is denoted by Chapter number followed by the index number, i.e., 4.2 for second equation in Chapter four. Chapters in the appendix are labeled alphabetically.

A great thanks is directed towards our thesis supervisor Kaiyuan Lu for his inspirational guidance and constructive criticism throughout the project period.

Aalborg University, May 31, 2024

Magnus Borg Wissing
<mwissi22@student.aau.dk>

Viktor Ferm
<vferm22@student.aau.dk>

Chapter 1

Introduction

Grundfos is a Danish pump manufacturer that produces a variety of pumps for different applications and power ratings. As the need for power output rises, the rating of the power electronic inverters also increases. In some Grundfos production pumps the winding construction is rated for higher power rating, which points to the inverters as the limiting factor. The power demand is at the brink of needing specially designed boards that are based on busbars instead of PCB's with thick cobber tracing. A solution to the challenge could be to use two inverters to meet the power demand, thereby no new inverter needs to be designed, but the power output can meet the demand. This saves the cost of designing and producing new power electronics and existing hardware can be used instead. Besides meeting the increased power rating, there might be other benefits by using two inverters, as the number of controllable stator phases doubles from three to six. Literature suggests, that with the use of two inverters there might be the possibility of reducing the induced common mode voltage, which is known to be a key factor when it comes to bearing currents.

Each inverter is supplying the motor with three phase power, which effectively categorises the machine as a Dual-Three-Phase synchronous machine. This type of machine configuration is the main scope of this thesis and Grundfos has provided a prototype of the DTP to be studied. In order to understand the characteristics and control of such a machine, an extensive study of literature has been conducted. First, the modelling of the machine and the inherent inductance is studied, which is followed by the implementation of FOC to operate the machine. Lastly, a study on different PWM strategies is presented, aiming to reduce CMV with the potential effect of minimizing bearing currents.

1.1 Literature Study on DTP Machines

Electrical machines with more than three phases is referred to as multi-phase machines. The number of phases can range from a multiple of three phases to machines with $4, 5, 7$ or more phases. Every type of multi-phase machine offers different benefits and drawbacks in terms of cost, production, reduced torque ripple, lower THD, an so forth [1].
The multi-phase machine composed of two three-phase winding sets with isolated neutral points is referred to as a Dual-Three-Phase. An important aspect to note about DTP systems is the electrical angle of the two sets of windings in relation to each other. The winding configuration can be constructed with a spatial shift, offsetting the two systems in terms of phase and common angle displacements are 0, 15° and 30°. The angular displacement can be implemented by placing the sets in different slots in the stator and the resulting angle is a product of the slot offset and slot/pole configuration. The terminology is vastly different in the literature. For example a DTP machine with the windings spatially shifted by 30° can be referred to as *double-star machine*, *split-phase* or *asymmetrical machine* as stated in [2]. In the review on Multi-Phase-Machines [1], it is stated that this spatial offset results in reduced torque ripple at high torque output, which is due to the harmonic reduction capabilities of the winding structure.
The DTP machine studied in this thesis has an angular displacement of 0°. The reason being, the prototype Grundfos provided is made from a conventional three-phase IPMSM that has two sets of three-phase windings that are wound on each half of the stator. The two winding sets are then connected in parallel resulting in a conventional three-phase system. By splitting the parallel connection into the two sets again, the machine becomes a DTP with no angular displacement.
As this machine features parallel current carrying leads, the inductance in the stator voltage equations must differ from a conventional PMSM. In the article [2] the extra couplings from set to set is explored and it is described how the machine model differs from that of a conventional PMSM. Moreover, a simulation underlines how this has an effect on the machine model and the dynamic performance when operating. This thesis does not focus on dynamic performance, as the primary use case is pumping, which often run continuously.

The mutual inductance from set to set has to be described to fully understand the machine and in [3], [4] a general approach to modelling these terms is introduced. Overall, the inductance in the *abc*-domain of the machine is broken into three parts: the self-inductance, the mutual inductance within a single set and the mutual inductance from one set to another.
Moreover, a modified Clark-Park transformation is also introduced that makes it possible to perform reference frame transformation of the 6-by-6 matrix from *abc*

to the *dq*-domain. This makes it possible to describe the stator voltage equations in the rotating reference frame, which is essential for FOC.
Although the machine is currently in production at Grundfos, it has been rewired, requiring some machine parameters to be characterized. Especially the inductances are of interest, since the two sets of windings are to couple with each other with an unknown strength. Various methods from the indirect method of static torque measurement, to the DC method of measuring the time constant of the current reacting to a step change, has been proposed. In the article [5], the estimation of inductances in the DTP is investigated. The method employed is based on a voltage step change. However, this method introduces some current oscillations, as it is challenging to find a DC source that is not capacitor-based to deliver the steep step change. One simple, yet effective method using a simple AC test has been proposed in [6]. Similar to other methods, the proposed approach relies on the relationship between back EMF and flux-linkage. Using this method, the inductance within a single set can be measured, and only minor adjustments to the test setup and post-processing are needed to measure the inductances arising from the coupling between two sets.

With the prototype parameterised it enables vector control of the machine. In the article [2] it is stated that conventional FOC utilizing two off-the-shelf VSI's should be sufficient to run the machine. The two inverters would control a winding set each and they are controlled to apply the same current vector. If every aspect of the system is identical, meaning two identical inverters sharing the same DC link and controlling two identical balanced sets of windings, the same current references can be fed to both controllers. The article underlines how this conventional FOC can achieve correct steady state performance, but shows decreased dynamic performance in the DTP compared to conventional PMSM with the same control. If dynamic performance of the DTP is needed, article [4] suggest a decoupled vector control scheme, where the *dq* transformed quantities are transformed yet again. This second transformation uses a vector space decomposition method called *DQ*-transformation, which decouples the system and represents it mathematically without the cross couplings between the two sets. Once again, this topic is not investigated further as dynamic performance is not within the scope of the project, but the outline of this *dq* to DQ transformation is available in appendix C.

From Grundfos' perspective, the reduction of CM voltage using the DTP system is of interest. The CM voltage produced by the switching action of the inverter is closely linked to system reliability due to its association with bearing degradation. In inverter driven variable speed drives, the PWM generated output voltage induces a common mode voltage that excites parasitic capacitance couplings in the motor. This leads to unwanted shaft voltage and bearing currents that affect the

lifetime of the system [7], [8].

CM voltage suppression methods can be divided into hardware and software implementations. Hardware suppression relies on adding additional components such as filters or a grounding brush to the motor bearing, in order to suppress the CM path in the system. By adding components the cost increases and the power density decreases as stated in [9]. On the other hand, software suppression can be implemented by altering the PWM strategy with the goal of suppressing the source of the CMV.
The article [10] describes a PWM control strategy with a resulting CM voltage of zero, in theory. This control strategy utilizes two VSI's working in parallel. The parallel phase legs on the inverters are connected with a coupling inductor and the combined currents are fed to a three-phase RL load. This ZCMV PWM strategy is tested against the conventional space vector modulation PWM scheme, where gate pulses to the inverters are synchronized and with the gate signals interleaved.
In [11] the ZCMV PWM strategy is further analyzed and implemented on a DTP machine with two identical winding sets. As each winding set is controlled independently by its own VSI the need for coupling inductors is eliminated. This zero CM voltage can only be implemented on a DTP machine that has two identical groups of three phase back EMFs.

1.2 Problem statement

As indicated by the introduction and literature study, this project is centered around the DTP machine. The objective is to describe the theoretical machine model of the DTP and with this knowledge determine the parameters of the prototype. The machine can then be operated in the laboratory using FOC and the machine model can be validated. This enables the investigation of the different PWM strategies and whether any strategy leads to a reduced CMV in this prototype. The objectives can therefore be simplified to:

- Describe and determine the parameters of the DTP prototype
- Describe and implement a FOC on the DTP prototype
- Describe and implement CMV suppressing PWM strategies

This thesis seeks to answer these questions by exploring the related theory, creating simulations and building a test setup to measure and conclude on the problem statement objectives.

1.3 Scope of the project

In order to fulfill the scope of the problem statement, a machine model of the DTP has to be developed. Then the parameters of the DTP prototype is investigated and the inductances of the machine is simulated using FEA and verified by measurements of the prototype. When the machine is characterised, the laboratory test setup must be rebuild to fit the needs of the project. This includes rewiring the inverters of an existing two-motor test setup, to use both inverters for supplying the DTP. The load machine, which is normally inverted fed, is connected to a resistor bank and transformer configuration, thereby acting as a variable load. A simulation of FOC on the DTP machine model is created and this control is implemented on the test setup. The performance of the speed- and current loop is verified by comparing the simulation results to the test setup results.

Lastly, the verified model of the DTP is used to simulate the different CM voltage reduction PWM schemes. Due to time- and laboratory constraints these PWM schemes can not be realised in the test setup. Some CM voltage measurements on the physical system underlines the existence of the problem and the missing implementation is discussed in the 'Future Work' section.

1.4 Limitation and assumptions

This thesis will exclude or not consider the following list:

- No hardware is produced (Custom PCB's)
- The mechanical machine construction (slot/pole configuration) is not described
- Motor winding layout(winding factor, fill factor etc.) are not covered
- I/F start-up assisted sensorless control algorithm for position estimation is not described
- MTPA for IPMSM is not implemented on the test setup
- Cross-coupling compensation for current loop control is not covered

Chapter 2

Generel Machine Model for DTP

This chapter describes the DTP machines stator voltage equations, details the inductances and explains how to extend the Clarke-Park reference frame transformation to fit a DTP system. Lastly, the voltage equations is related to the electric torque equation such the machine operation can be simulated.

2.1 Voltage Equations DTP Machine *abc*-domain

The DTP machine can be visualised as six phases consisting of a phase inductance L_s and phase resistance R_s in series. This equivalent electrical circuit shown in figure 2.1. The three *abc*-currents runs in two sets of three phase windings which are connected in two neutral points. The angle β describes the angular displacement between the two winding sets, which in this machine is 0° as the winding's are parallel wound. The voltage equation and machine variables as seen from the stator terminals are:

$$\begin{bmatrix} v_{a1} \\ v_{b1} \\ v_{c1} \\ v_{a2} \\ v_{b2} \\ v_{c2} \end{bmatrix} = \begin{bmatrix} R_s & 0 & 0 & 0 & 0 & 0 \\ 0 & R_s & 0 & 0 & 0 & 0 \\ 0 & 0 & R_s & 0 & 0 & 0 \\ 0 & 0 & 0 & R_s & 0 & 0 \\ 0 & 0 & 0 & 0 & R_s & 0 \\ 0 & 0 & 0 & 0 & 0 & R_s \end{bmatrix} \begin{bmatrix} i_{a1} \\ i_{b1} \\ i_{c1} \\ i_{a2} \\ i_{b2} \\ i_{c2} \end{bmatrix} + \begin{bmatrix} p\lambda_{a1} \\ p\lambda_{b1} \\ p\lambda_{c1} \\ p\lambda_{a2} \\ p\lambda_{b2} \\ p\lambda_{c2} \end{bmatrix} \tag{2.1}$$

Which can be compressed into the following equation, where the bold values symbolizes a matrix.

$$\mathbf{v}_{abc(1,2)} = \mathbf{R}_s \mathbf{i}_{abc(1,2)} + p\boldsymbol{\lambda}_{abc(1,2)} \tag{2.2}$$

Where the subscript $abc(1,2)$ refers to the two sets of three phase windings and p

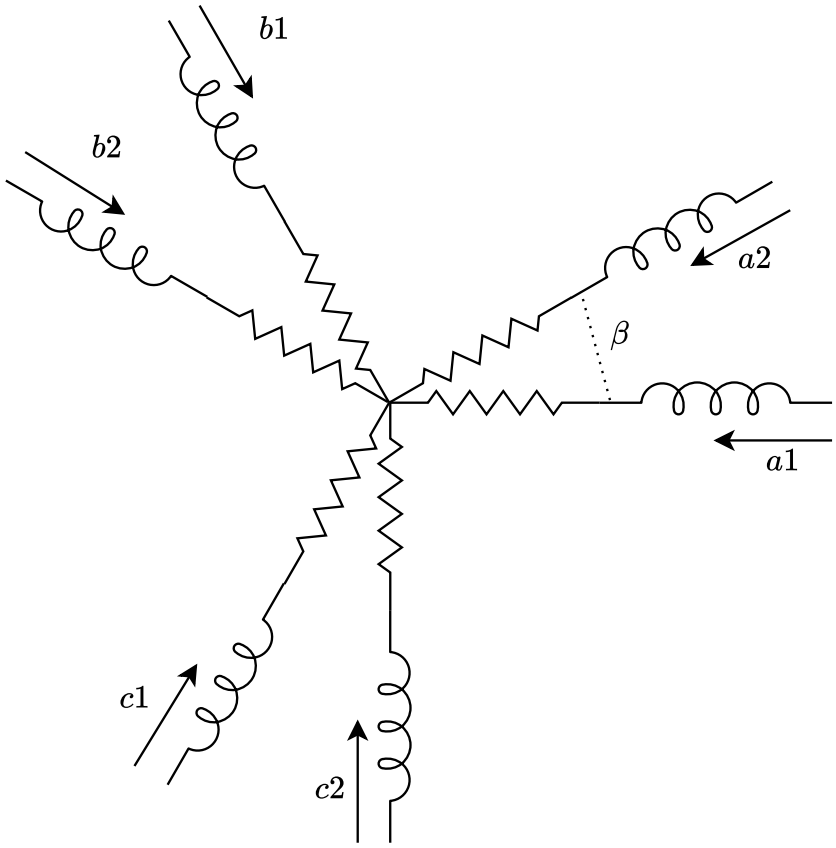

Figure 2.1: Equivalent electrical diagram of an DTP machine.

describes the derivative. The phase voltage is denoted by v, the currents by i and the flux-linkage by λ. The placement of the PM inside the rotor categorises the machine as a *parallel topology* IPMSM, which is visualised in the simplified rotor structure diagram 2.2

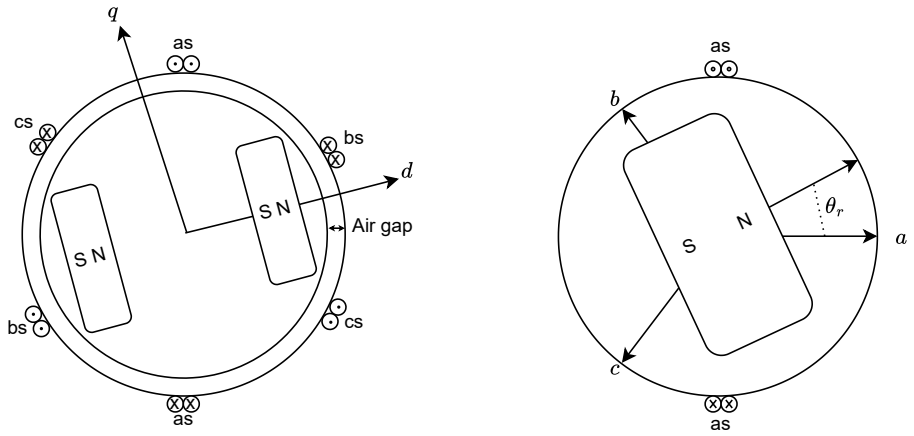

Figure 2.2: Left figure is the simplified rotor structure and right figure is the magnetic equivalent [12].

The *d*-axis is defined as being aligned with the PM north pole and the *q*-axis is defined as leading the *d*-axis by 90° as seen on the rotor structure diagram. The stator windings are marked *as*, *bs* and *cs* and represents both windings sets. The dot represents current flowing out from the plane and the cross is into the plane. Because of this structure the *d*-axis inductance is less than the *q*-axis inductance, $L_d < L_q$. On the simplified magnetic equivalent diagram *a*, *b* and *c* represents the flux vector produced by the currents in the windings. The *a*-axis flux is placed 90° from the *as* winding. The rotor position is defined as the angle θ_r between the *d*-axis and the *a*-axis. This anisotropic magnetic structure makes the inductances of the machine position dependent in the *abc*-domain.

2.2 Inductances in DTP Machine *abc*-domain

To define inductances in the machine, the flux-linkage term from equation 2.1 can be expanded into the following:

$$\boldsymbol{\lambda}_{abc(1,2)}(\theta_r) = \boldsymbol{L}(\theta_r)\mathbf{i}_{abc(1,2)} + \boldsymbol{\lambda}_{mpm,abc(1,2)}(\theta_r) \tag{2.3}$$

Where $\boldsymbol{L}$ is the inductance matrix and $\boldsymbol{\lambda}_{mpm}$ is the flux linkage from the permanent magnets. Assuming the two sets of winding's are balanced and the saturation effects are neglected, the inductances can be described by the following four matrices[3]:

$$\mathbf{L}(\theta_r) = \begin{bmatrix} \mathbf{L}_s(\theta_r) & \mathbf{M}(\theta_r) \\ \mathbf{M}^{\mathbf{T}}(\theta_r) & \mathbf{L}_s(\theta_r) \end{bmatrix} \tag{2.4}$$

Where $\boldsymbol{L_s}$ is the inductances within a single set of windings and $\mathbf{M}$ is the mutual inductance from one set to the other. The inductance of a single set of windings can be described by its self-inductance and the mutual inductance within its own winding's [13]:

$$\boldsymbol{L}_s(\theta_r) = \begin{bmatrix} L_a & M_{ab} & M_{ac} \\ M_{ba} & L_b & M_{bc} \\ M_{ca} & M_{cb} & L_c \end{bmatrix} \tag{2.5}$$

The diagonal describes the self-inductance and can be visualised for each phase as seen on figure 2.3, which represent a full electrical period.

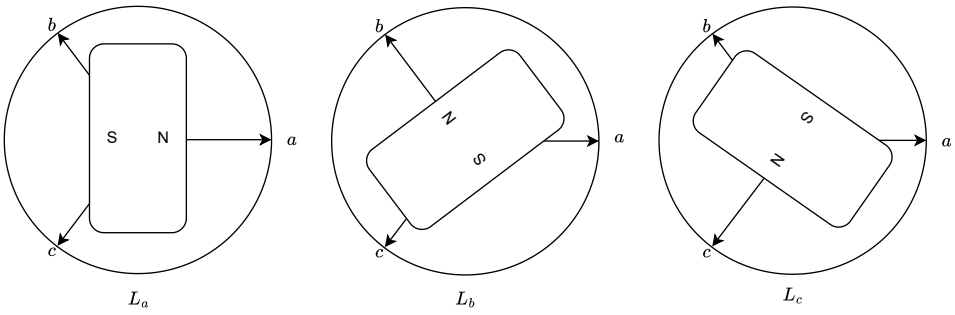

Figure 2.3: Self-inductances in a single set of three phase windings.

The self-inductance of winding *as* becomes minimum when the rotor *d*-axis is aligned with the *a*-axis at position 0° and 180°, because the reluctance is at its maximum at these angles. When the *d*-axis is at 90° and 270°, the phase *as* inductance is at its maximum, because the reluctance is at minimum. This results in the flux linking its own windings to become peak flux linkage value. This is also true for the phase *bs* and *cs* inductances, which are offset by $\frac{2\pi}{3}$ and $-\frac{2\pi}{3}$, respectively. This can be described by the following set of equations:

$$L_a = L_{ls} + L_A - L_B cos(2(\theta_r)) \tag{2.6}$$

$$L_b = L_{ls} + L_A - L_B cos(2(\theta_r - \frac{2}{3}\pi)) \tag{2.7}$$

$$L_c = L_{ls} + L_A - L_B cos(2(\theta_r + \frac{2}{3}\pi)) \tag{2.8}$$

Where L_{ls} is the leakage inductance, L_A is the average magnetization inductance and L_B is the second harmonic peak value. These inductance coefficients represents positive scalars. The second harmonic term describes that the phase inductance peaks twice in an electrical period. The non-diagonal elements of the $\boldsymbol{L_s}$ matrix

describes the mutual inductance's between the phases of a three phase system [14] as seen on figure 2.4.

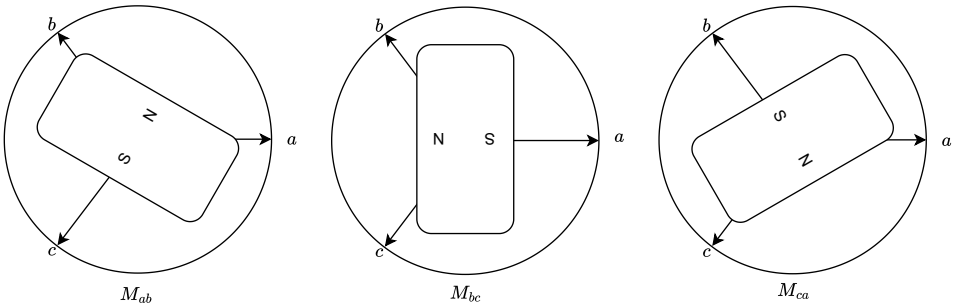

Figure 2.4: Mutual inductances in a single set of three phase windings.

These inductances can be described by the following set of equations:

$$M_{ab} = M_{ba} = L_A cos\left(\frac{2\pi}{3}\right) - L_B cos\left(2\left(\theta_r - \frac{\pi}{3}\right)\right) \tag{2.9}$$

$$M_{bc} = M_{cb} = L_A cos\left(\frac{2\pi}{3}\right) - L_B cos\left(2(\theta_r - \pi)\right) \tag{2.10}$$

$$M_{ca} = M_{ac} = L_A cos\left(\frac{2\pi}{3}\right) - L_B cos\left(2\left(\theta_r + \frac{\pi}{3}\right)\right) \tag{2.11}$$

Where L_A is the average magnetization inductance produced in one inductor acting on the adjacent inductor. In a mutual coupling the L_A term is scaled by a factor of $cos(\frac{2\pi}{3})$, which is the angle displacement between the phases. Again, L_B describes the peak value of the second harmonic part of the coupling and both values are positive scalars. The mutual inductance between two phases is at its minimum when the d-axis is positioned equally between them, which occurs at the angles $\theta_r = 60^\circ = 180^\circ = 300^\circ$. It is assumed that the inductances are symmetrical, therefore $M_{ab} = M_{ba}$ and so forth, and that the average value and second harmonic variation is equal in all three phase to phase mutual couplings.
In addition to the self-inductance and the mutual inductance between phases in a single winding set, there is the magnetic coupling between the two winding sets. This inductance can be described similarly to the mutual inductance within a single set. The matrix **M** describes the mutual inductances between two sets of three phase windings:

$$\mathbf{M}(\theta_r) = \begin{bmatrix} M_{a1a2} & M_{a1b2} & M_{a1c2} \\ M_{b1a2} & M_{b1b2} & M_{b1c2} \\ M_{c1a2} & M_{c1b2} & M_{c1c2} \end{bmatrix} \tag{2.12}$$

The notation M_{a1a2} describes the coupling of phase $a1$ in the first winding set to phase $a2$ in the second winding set. Likewise, M_{a1b2} describes the coupling of phase $a1$ is the first winding set to phase $b2$ in the second winding set. Like the inductance matrix for a single set of windings, the diagonal of the set-to-set inductance also features a form of self-inductance: The mutual inductance between the same phases in the two sets. This is visualised in figure 2.5.

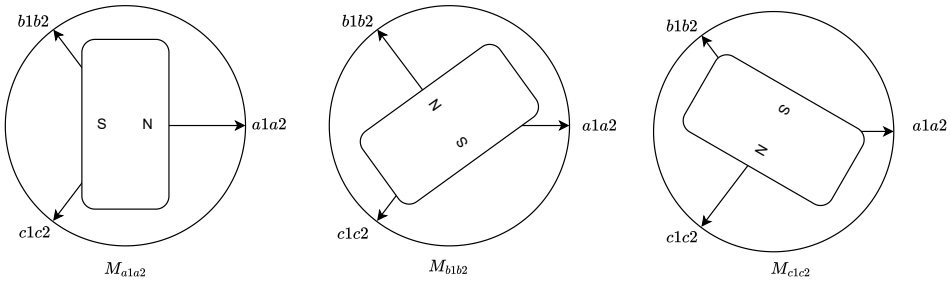

Figure 2.5: Mutual inductance between two identical phases in two sets of three phase windings.

The diagonal elements of the set-to-set inductance can be described as:

$$M_{a1a2} = M_A cos(0) - M_B cos\left(2\theta_r\right) \tag{2.13}$$

$$M_{b1b2} = M_A cos(0) - M_B cos\left(2\left(\theta_r - \frac{2\pi}{3}\right)\right) \tag{2.14}$$

$$M_{c1c2} = M_A cos(0) - M_B cos\left(2\left(\theta_r + \frac{2\pi}{3}\right)\right) \tag{2.15}$$

Where M_A is the average magnetization inductance produced in the inductor of the first set, acting on the identical phase in the other set. This value is not scaled by a factor as the angle difference between them are zero. M_B describes the peak value of the second harmonic part of the coupling and both values are positive scalars. Like the self-inductance in a single set, the M_{a1a2} inductance is at minimum at 0° and 180° rotor position. Similarly, M_{b1b2} and M_{c1b2} is offset by $\frac{2\pi}{3}$ and $-\frac{2\pi}{3}$, respectively.
Figure 2.6 illustrates the three non-diagonal elements of The matrix **M** that couples from one set of windings to the second set of windings.

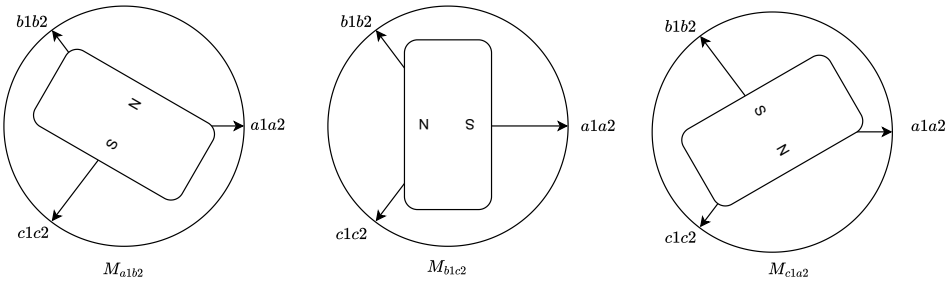

Figure 2.6: Mutual inductance between two sets of three phase windings.

These inductances can be described by the following set of equations:

$$M_{a1b2} = M_{b1a2} = M_A cos\left(\frac{2\pi}{3}\right) - M_B cos\left(2\left(\theta_r - \frac{\pi}{3}\right)\right) \tag{2.16}$$

$$M_{b1c2} = M_{c1b2} = M_A cos\left(\frac{2\pi}{3}\right) - M_B cos\left(2(\theta_r - \pi)\right) \tag{2.17}$$

$$M_{c1a2} = M_{a1c2} = M_A cos\left(\frac{2\pi}{3}\right) - M_B cos\left(2\left(\theta_r + \frac{\pi}{3}\right)\right) \tag{2.18}$$

Where M_A is the average magnetization inductance produced in one inductor acting on the adjacent inductor. Again, the mutual coupling M_A is scaled by a factor of $cos(\frac{2\pi}{3})$, which is the angle displacement between the phases. M_B describes the peak value of the second harmonic part of the coupling and both values are positive scalars. The effect of the mutual inductance between two phases is at its minimum when the *d*-axis is positioned equally between them, which occurs at the angles $\theta_r = 60^\circ = 180^\circ = 300^\circ$. It is assumed that the inductances are symmetrical, therefore $M_{a1b1} = M_{b1a1}$ and so forth, and that the average and second harmonic value are equal in all three phase to phase mutual couplings.

The last element of the flux linkage equation 2.3 is the flux linkage of the permanent magnets. By definition λ_{mpm} is the flux linkage established by the permanent magnets in the rotor, as seen from the stator side. In other words, the differential $p\lambda_{mpm}$ would be the open circuit voltage induced in the stator windings by rotating the shaft[14]. From figure 2.5 it can be seen that the PM flux linkage can be described in the *abc*-domain by the following equations:

$$\boldsymbol{\lambda}_{mpm,abc(1,2)}(\theta_r) = \lambda_{mpm} \begin{bmatrix} cos(\theta_r) \\ cos(\theta_r - \frac{2\pi}{3}) \\ cos(\theta_r + \frac{2\pi}{3}) \\ cos(\theta_r) \\ cos(\theta_r - \frac{2\pi}{3}) \\ cos(\theta_r + \frac{2\pi}{3}) \end{bmatrix} \tag{2.19}$$

The flux linkage between the permanent magnet and the flux vectors from the 6 phases is at its maximum when the vectors are directly aligned. This is true at the angles $\theta_r = 0^\circ = 120^\circ = 240^\circ$. It is assumed that the back EMF produced by the permanent magnets are sinusoidal and have a constant amplitude [14].

2.3 Inductances in DTP Machine *dq*-domain

The transformation from the *abc*-domian to the *dq*-domain is performed using the amplitude invariant Clarke-Park transformation which is defined as [13]:

$$\boldsymbol{T}(\theta) = \frac{2}{3} \begin{bmatrix} cos\,(\theta) & cos\left(\theta - \frac{2\pi}{3}\right) & cos\left(\theta + \frac{2\pi}{3}\right) \\ -sin\,(\theta) & -sin\left(\theta - \frac{2\pi}{3}\right) & -sin\left(\theta + \frac{2\pi}{3}\right) \\ \frac{1}{2} & \frac{1}{2} & \frac{1}{2} \end{bmatrix} \tag{2.20}$$

The transformation is able to transform three vectors in the stator reference frame, into two vectors in a rotating reference frame. The rotor reference frame displacement is defined by the angle θ between the *d*-axis and a known vector in the stator reference frame.
When transforming the voltage equations from *abc*-domain into the *dq*-domain, all the vectors are transformed from three to two vectors. But first, the inductances need to be reference frame transformed, in order to appear as *dq*-quantities in the voltage equations. The value of these terms can be defined by performing transformtion on the inductance matrix [13]. As introduced in equation 2.4 the inductance matrix a 6x6 matrix and the conventional transformation only works for three phase systems, that is described by a 3x3 matrix. Therefore a modified transformation is defined [3]:

$$\boldsymbol{T}_1(\theta) = \begin{bmatrix} \boldsymbol{T}(\theta) & \mathbf{0}_{3,3} \\ \mathbf{0}_{3,3} & \boldsymbol{T}(\theta) \end{bmatrix} \tag{2.21}$$

Where $\mathbf{0}_{3,3}$ is a null matrix. Using the matrix modified for 6x6 transformation on the $\mathbf{L}(\theta_r)$ transforms the inductances to *dq*-quantities[3]:

$$\boldsymbol{L}_{T_1} = \boldsymbol{T_1}(\theta) \cdot \boldsymbol{L} \cdot \boldsymbol{T_1}(\theta)^{-1} \tag{2.22}$$

Which yields the following transformed inductance matrix $\boldsymbol{L}_{T_1}$:

$$\boldsymbol{L}_{T_1} = \begin{pmatrix} \frac{3L_A}{2} + L_{\text{ls}} - \frac{3}{2}L_B\text{Cos}\left[2\left(\theta-\theta_r\right)\right] & \frac{3}{2}L_B\text{Sin}\left[2\left(\theta-\theta_r\right)\right] & 0 & \frac{3}{2}\left(M_A - M_B\text{Cos}\left[2\left(\theta-\theta_r\right)\right]\right) & \frac{3}{2}M_B\text{Sin}\left[2\left(\theta-\theta_r\right)\right] & 0 \\ \frac{3}{2}L_B\text{Sin}\left[2\left(\theta-\theta_r\right)\right] & \frac{3L_A}{2} + L_{\text{ls}} + \frac{3}{2}L_B\text{Cos}\left[2\left(\theta-\theta_r\right)\right] & 0 & \frac{3}{2}M_B\text{Sin}\left[2\left(\theta-\theta_r\right)\right] & \frac{3}{2}\left(M_A + M_B\text{Cos}\left[2\left(\theta-\theta_r\right)\right]\right) & 0 \\ 0 & 0 & L_{\text{ls}} & 0 & 0 & 0 \\ \frac{3}{2}\left(M_A - M_B\text{Cos}\left[2\left(\theta-\theta_r\right)\right]\right) & \frac{3}{2}M_B\text{Sin}\left[2\left(\theta-\theta_r\right)\right] & 0 & \frac{3L_A}{2} + L_{\text{ls}} - \frac{3}{2}L_B\text{Cos}\left[2\left(\theta-\theta_r\right)\right] & \frac{3}{2}L_B\text{Sin}\left[2\left(\theta-\theta_r\right)\right] & 0 \\ \frac{3}{2}M_B\text{Sin}\left[2\left(\theta-\theta_r\right)\right] & \frac{3}{2}\left(M_A + M_B\text{Cos}\left[2\left(\theta-\theta_r\right)\right]\right) & 0 & \frac{3}{2}L_B\text{Sin}\left[2\left(\theta-\theta_r\right)\right] & \frac{3L_A}{2} + L_{\text{ls}} + \frac{3}{2}L_B\text{Cos}\left[2\left(\theta-\theta_r\right)\right] & 0 \\ 0 & 0 & 0 & 0 & 0 & L_{\text{ls}} \end{pmatrix}$$

If the rotor reference frame is rotating with the same electrical speed as the rotor ω_e and the θ angle is measured between the d-axis and the a-axis of the stator, then the statement $\theta = \theta_r$ is true. In other words, the dq-frame is rotating with the rotor speed. The time-varying elements of the inductance is then eliminated and the $\boldsymbol{L}_{T_1}$ can be simplified to:

$$\boldsymbol{L}_{T_1} = \begin{pmatrix} \frac{3L_A}{2} - \frac{3L_B}{2} + L_{\text{ls}} & 0 & 0 & \frac{3}{2}\left(M_A - M_B\right) & 0 & 0 \\ 0 & \frac{3L_A}{2} + \frac{3L_B}{2} + L_{\text{ls}} & 0 & 0 & \frac{3}{2}\left(M_A + M_B\right) & 0 \\ 0 & 0 & L_{\text{ls}} & 0 & 0 & 0 \\ \frac{3}{2}\left(M_A - M_B\right) & 0 & 0 & \frac{3L_A}{2} - \frac{3L_B}{2} + L_{\text{ls}} & 0 & 0 \\ 0 & \frac{3}{2}\left(M_A + M_B\right) & 0 & 0 & \frac{3L_A}{2} + \frac{3L_B}{2} + L_{\text{ls}} & 0 \\ 0 & 0 & 0 & 0 & 0 & L_{\text{ls}} \end{pmatrix}$$

By defining L_{dq} and M_{dq} as

$$\begin{cases} L_d &= \frac{3}{2}(L_A - L_B) + L_{ls} \\ L_q &= \frac{3}{2}(L_A + L_B) + L_{ls} \\ M_d &= \frac{3}{2}(M_A - M_B) \\ M_q &= \frac{3}{2}(M_A + M_B) \end{cases} \tag{2.23}$$

the matrix can be further simplified:

$$\boldsymbol{L}_{T_1} = \begin{bmatrix} L_d & 0 & 0 & M_d & 0 & 0 \\ 0 & L_q & 0 & 0 & M_q & 0 \\ 0 & 0 & L_{ls} & 0 & 0 & 0 \\ M_d & 0 & 0 & L_d & 0 & 0 \\ 0 & M_q & 0 & 0 & L_q & 0 \\ 0 & 0 & 0 & 0 & 0 & L_{ls} \end{bmatrix} \tag{2.24}$$

To finalize the flux linkage in *dq*-domain the flux linkage from the permanent magnets may also be transformed. Using equation 2.19 and the Clarke-Park transform from equation 2.20 the transformation can be described as:

$$\boldsymbol{T}(\theta) \cdot \boldsymbol{\lambda}_{mpm,abc(1)}(\theta_r) \tag{2.25}$$

$$\boldsymbol{T}(\theta) \cdot \boldsymbol{\lambda}_{mpm,abc(2)}(\theta_r) \tag{2.26}$$

Which simplifies 2.252.26 to the following term for both set of windings:

$$\boldsymbol{\lambda}_{mpm,dq} = \begin{bmatrix} \lambda_{mpm} cos(\theta - \theta_r) \\ -\lambda_{mpm} sin(\theta - \theta_r) \\ 0 \end{bmatrix} \tag{2.27}$$

One again, the speed of the rotating frame is set to the electrical speed of the rotor ω_e and the matrix is simplified:

$$\boldsymbol{\lambda}_{mpm,dq} = \begin{bmatrix} \lambda_{mpm} \\ 0 \\ 0 \end{bmatrix} \tag{2.28}$$

The full flux linkage matrix in the *dq*-domain is expressed in its final form, without the zero-sequence vector, as:

$$\begin{bmatrix} \lambda_{d1} \\ \lambda_{q1} \\ \lambda_{d2} \\ \lambda_{q2} \end{bmatrix} = \begin{bmatrix} L_d & 0 & M_d & 0 \\ 0 & L_q & 0 & M_q \\ M_d & 0 & L_d & 0 \\ 0 & M_q & 0 & L_q \end{bmatrix} \begin{bmatrix} i_{d1} \\ i_{q1} \\ i_{d2} \\ i_{q2} \end{bmatrix} + \begin{bmatrix} \lambda_{mpm} \\ 0 \\ \lambda_{mpm} \\ 0 \end{bmatrix} \tag{2.29}$$

From this flux-linkage matrix it is seen that the non-zero off-diagonal elements describes a coupling between the two sets of windings.

2.4 Voltage Equations DTP Machine *dq*-domain

Performing the modified transformation on the stator voltage equation in *abc*-domain 2.2

$$\boldsymbol{T_1}(\theta)\mathbf{v}_{abc(1,2)} = \begin{bmatrix} v_{d1} \\ v_{q1} \\ v_{d2} \\ v_{q2} \end{bmatrix} \tag{2.30}$$

yields the following set of equations [2]:

$$\begin{cases} v_{d1} = R_s i_{d1} + \frac{di_{d1}}{dt} L_d - \omega_e L_q i_{q1} + M_d \frac{di_{d2}}{dt} - \omega_e M_q i_{q2} \\ v_{q1} = R_s i_{q1} + \frac{di_{q1}}{dt} L_q + \omega_e (L_d i_{d1} + \lambda_{mpm}) + M_q \frac{di_{q2}}{dt} + \omega_e M_d i_{d2} \\ v_{d2} = R_s i_{d2} + \frac{di_{d2}}{dt} L_d - \omega_e L_q i_{q2} + M_d \frac{di_{d1}}{dt} - \omega_e M_q i_{q1} \\ v_{q2} = R_s i_{q2} + \frac{di_{q2}}{dt} L_q + \omega_e (L_d i_{d2} + \lambda_{mpm}) + M_q \frac{di_{q1}}{dt} + \omega_e M_d i_{d1} \end{cases} \tag{2.31}$$

Where the subscript $d1$ describes a d-axis component of the first sets of windings and $q2$ describes a q-axis component of the second set. Looking at the first equation of v_{d1} voltage the set-to-set coupling terms are identified as the second to last and last term, where currents from the other set is featured. This is the case for all the stator dq-voltages, which suggest that the two sets are indeed influencing each other.
The electrical torque produced by the machine can be described by the conventional three-phase torque equations [2]. The sum of the torque from each set yields the total torque produced.

$$T_e = \frac{3}{2} N_{pp} (\lambda_{pm}(i_{q1} + i_{q2}) + (L_d - L_q)(i_{d1} i_{q1} + i_{d2} i_{q2}) + (M_d - M_q)(i_{d1} i_{q2} + i_{d2} i_{q1})) \tag{2.32}$$

The first term represents the magnetic toque produced by the permanent magnets and is only dependent on the q-axis currents. The other terms are the torque generated by the reluctance, that is present in the machine because of the salient pole construction of the rotor. To utilize the reluctance torque both dq-axis currents are required in both winding sets and since $L_d > L_q$, $M_d > M_q$ the d-axis currents must be of negative polarity, resulting in positive contribution from both the magnetic and reluctance torque in the combined electrical torque [13]. This must be taken into account when designing a suitable control strategy for running the DTP machine.

Chapter 3

Common Mode Voltage in a DTP

This chapter aims to describe the common mode voltage and which problems it may cause such as shaft voltage and bearing currents. The literature claims that 25% of all bearing faults are due to high-frequency switching and high dv/dt [15]. The problems from CM voltage and how to solve them have gained huge interest from the industry due to impact of the reliability of the system. In the litterature study it was outlined that both hardware and software solutions can be implemented to suppress the problems created from CM voltage.

This project focus on migitating the CM voltage from the software side by analyzing different PWM schemes. A total of three different PWM schemes and their performance in suppressing common mode voltage in a DTP will be covered:

1. Conventional Space Vector Modulation (SVM), where gate signals to both inverters are synchronized.
2. Conventional Space Vector Modulation with interleaving.
3. A proposed Zero CM voltage PWM scheme (ZCMV).

First a review of inverter induced bearing currents and the parasitic elements in the DTP is conducted. Afterwords the definition of the common mode voltage in the DTP is presented and lastly an analysis of the three mentioned PWM schemes will be outlined.

3.1 Inverter induced bearing currents and parasitics

Faults in the motor bearings can stem from either a mechanical or electrical side. On the electrical side shaft voltage and current are a main factor for degradation of

the bearing. When an inverter is operating a motor it can be viewed as a high frequency voltage source in the common mode circuit. The consequences are different inverter induced bearing currents that can be classified as[16]:

1. Capacitive bearing current caused by dv/dt over the bearings and the bearing capacitance. This current amplitude is small compared to other forms and is not dangerous to the drive.

2. Electric discharge machining (EDM) current. The CM voltage will induce a shaft voltage. If this shaft voltage exceeds the dielectric strength of the oil film of the bearings a discharge current will flow though the bearings.

3. HF circulating currents. The high dv/dt at the terminals excites mainly the stator winding to frame parasitic capacitance, that leads to a high frequency common mode current. The ground current excites a magnetic flux around the shaft which induces shaft voltage along the shaft. If the shaft voltage is large enough to puncture the insulating properties of the lubricating film it causes a circulating current in the bearings. Size of the current peaks vary with the size of the motor.

4. Bearing currrent due to rotor ground currents. If the motor frame is poorly grounded and the rotor is connected to earth potential via the load that has lower impedance grounding, the overall common mode current may arc through the bearings, though the shaft and pass as rotor ground current. The size of this can reach great magnitudes and destroy bearing within a short period.

The current types (1) and (2) are related to the CM voltage on the bearing voltage while (3) and (4) are caused by HF common mode currents that comes from the interaction of the CM voltage with high dv/dt and parasitics capacitance between stator winding and the motor frame.

When analyzing the motor, there are different parasitic capacitances that can be excited. Figure 3.1 shows the simplified common mode circuit for the DTP where the pole voltage are viewed as a HF voltage source. Z_{dg} is the grounding impedance and Z_{cable} is the transmission impedance of the cable for each phase. C_{sf} is the parasitic capacitance between the stator winding and the motor frame, C_{sr} is between the stator winding and the rotor and C_{rf} is between the rotor and the motor frame [11]. R_{sf}, R_{sr} and R_{rf} are expressing the iron core losses for the high-frequency leakage current. In the simplified CM circuit the bearings consists of the resistance R_b, a variable capacitance C_b and a switch S_b.

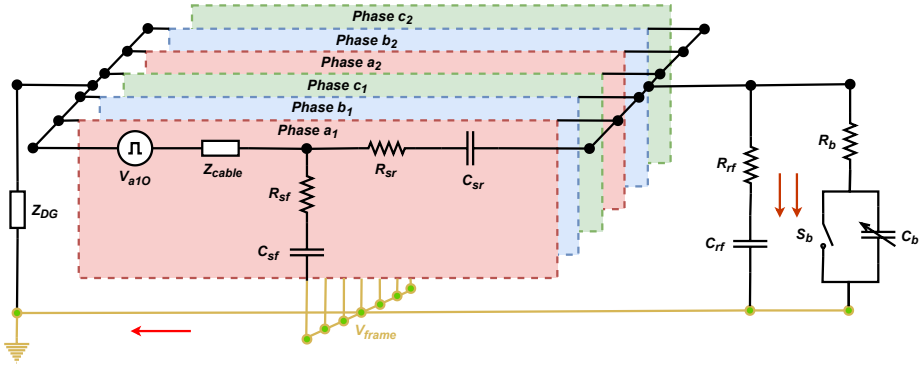

Figure 3.1: CM equivalent model for the dual three phase machine [11].

3.2 Common mode voltage

As the consequences of the CM voltage have been described, this section will give a description of the definition of the CM voltage. In ideal motor operation with three phases the voltage applied to the motor is sinusoidal waveforms that are complete symmetric in amplitude, have same frequency and are 120° phase shifted. The average voltage of the 3 voltage components would then at all time be zero.
With the introduction of variable speed drive where a PWM-driven inverter is used to ensure that the motor is operating as efficient as possible at different torque and speed profiles, the sum of all voltage in a single three-phase system cannot be assumed to be 0 due to its square pulse waveforms.

The CM voltage is defined as the average instantaneous voltage of each phase with respect to the DC link midpoint.

$$V_{cm} = \frac{1}{3}(V_{aO} + V_{bO} + V_{cO}) \tag{3.1}$$

The voltage V_{aO}, V_{bO} and V_{cO} for a 2-level inverter can have two voltage levels: $V_{dc}/2$ or $-V_{dc}/2$. Three of these voltage values together can therefore never be zero and the CM voltage cannot be eliminated for a standard three phase two-level inverter. To achieve zero CM voltage, more control freedoms should be introduced. This is where the DTP machine is introduced. The dual inverter configuration and DTP can be seen visualised in figure 3.2.

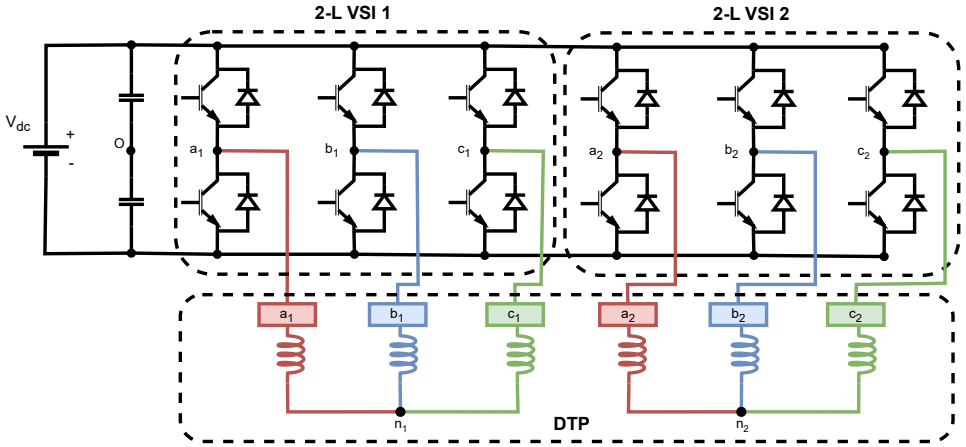

Figure 3.2: Dual inverter and DTP configuration.

For a DTP setup with two isolated neutral points two sub-CM voltage for each system exist:

$$V_{cm1} = \frac{1}{3}(V_{a1O} + V_{b1O} + V_{c1O}) \tag{3.2}$$

$$V_{cm2} = \frac{1}{3}(V_{a2O} + V_{b2O} + V_{c2O}) \tag{3.3}$$

Even with isolated neutral points, both of the two sub-CM voltages can influence the CM related performance at the same time through the stray capacitance in the motor and the generalized total common mode voltage is [17]:

$$V_{cm} = \frac{1}{2}(V_{cm1} + V_{cm2}) = \frac{1}{6}(V_{a1O} + V_{a2O} + V_{b1O} + V_{b2O} + V_{c1O} + V_{c2O}) \tag{3.4}$$

As the number of elements accountable for producing CM voltage is 6 and thereby an equal number, it can be easily deduced that the common voltage can be removed with a dual inverter setup. The criterion for zero CM voltage is that three upper switches of the half bridges are ON, while the lower switches are ON in the 3 remaining half bridges. These state must be met at all time in order to produce zero CM voltage. In order to do so, the chosen PWM strategy is essential for the CM voltage mitigation.

3.3 PWM schemes

The following section will outline the three different PWM schemes. The two first schemes are based on the space vector modulation PWM strategy, while the last scheme is a modulation strategy that theoretically can eliminate the CM voltage.
One important note for the following description is, that in a 2-level VSI having the upper switch in the half bridge active, while the lower is inactive is defined as "1". The opposite is defined as "0". The gate signal controlling the half bridge of each phase are notated as S_a, S_b and S_c. All PWM schemes are visualised as modelling the same reference, which is passed to both inverters.
As there are 6 switches in one standard 2 level VSI, a total of 8 legal switching states are possible . Thereby there exist 8 different voltage vectors $V_0, V_1....V_7$. Here $V_1 - V_6$ are called the active voltage vectors and V_0, V_7 are called zero vectors, as they do not produce a voltage difference across the load. All voltage vectors and their corresponding switch states are shown in table 3.1.

Voltage Vector	State	$\mathbf{V_{aO}}$	$\mathbf{V_{bO}}$	$\mathbf{V_{cO}}$	Space vector
V_0	000	$-V_{dc}/2$	-$V_{dc}/2$	-$V_{dc}/2$	-
V_1	100	$V_{dc}/2$	-$V_{dc}/2$	-$V_{dc}/2$	2/3 $V_{dc}\angle 0°$
V_2	110	$V_{dc}/2$	$V_{dc}/2$	-$V_{dc}/2$	2/3 $V_{dc}\angle 60°$
V_3	010	-$V_{dc}/2$	$V_{dc}/2$	-$V_{dc}/2$	2/3 $V_{dc}\angle 120°$
V_4	011	-$V_{dc}/2$	$V_{dc}/2$	$V_{dc}/2$	2/3 $V_{dc}\angle 180°$
V_5	001	-$V_{dc}/2$	-$V_{dc}/2$	$V_{dc}/2$	2/3 $V_{dc}\angle 240°$
V_6	101	$V_{dc}/2$	-$V_{dc}/2$	$V_{dc}/2$	2/3 $V_{dc}\angle 300°$
V_7	111	$V_{dc}/2$	$V_{dc}/2$	$V_{dc}/2$	-

Table 3.1: Switching states and the corresponding voltage vectors of a 2-level inverter.

3.3.1 SVM with synchronized pulses

Space vector modulation is a widely used PWM strategy within inverter control. It produces fundamental output voltage 15.5% higher than what can be produced by for example the SPWM method. It also introduces less harmonic distortion of the load current, lower torque ripple in AC motors, and lower switching losses [12]. In SVM the *abc* voltages reference are represented as a space vector V_{ref} in the complex plane and the reference vector is synthesised by the two adjacent vectors of the sector the space vector is positioned at.

For the first presented PWM scheme, the DTP is operated with SVM and PWM signals send to the transistors are synchronized. The switching pattern is therefore identical for VSI 1 and VSI 2. In figure 3.3 (a), V_{ref} is in sector 1 in the hexagon and the active vectors V_1 and V_2 along with the zero vectors are used

to synthesise the space vector by switching between the two adjacent vectors and the zero vectors, in the sector. For example in the first sector, the reference vector is synthesised by a combination of active- and zero vectors in the sequence of: $V_0 \rightarrow V_1 \rightarrow V_2 \rightarrow V_7 \rightarrow V_2 \rightarrow V_1 \rightarrow V_0$. This is a full switching period and the times t_0, t_7, t_1 and t_2 refers to time spent on each vector.

When synchronized operation on VSI 1 and 2 with SVM is applied, the highest CM voltage is generated at the zero voltage vector, where the CM voltage has an amplitude of $V_{dc}/2$ as seen in figure 3.3 (b). Furthermore the CM voltage will never be zero, as the total number of "1" and "0" are never identical. This is due to the fact that both inverters are always using the same voltage vectors during a whole switching cycle.

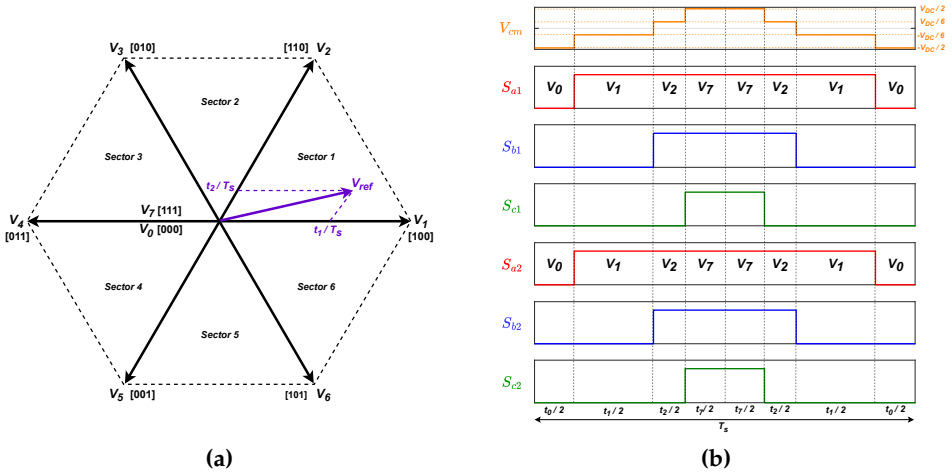

Figure 3.3: a) Hexagon showing the different voltage vector and V_{ref}, b) Convential SVM scheme.

3.3.2 SVM with interleaving

One way of reducing the CM voltage with SVM is by delaying the phase of the carrier wave for one of the inverters by 180°, also known as interleaving. The reference voltage for both in inverters are still the same, thereby also the duty cycle and the SVM algorithm does not change. The interleaved operation of the PWM signals enables the two inverters to use different voltage vectors and opposite zero vectors while still producing the desired reference vector. Figure 3.4 shows the switching pattern for one switching period when operating with interleaving in sector 1. The cycle is started with V_0 operating for inverter 1 and V_7 operating for inverter 2 yielding three "1" and "0" overall. The CM voltage is therefore zero. In the next step V_1 becomes active for inverter 1, while V_2 becomes active for inverter 2. The criterion for zero CM voltage is still met. However as the time spent on V_2 is less

than for V_1, inverter 2 will shift to operate in V_1, while inverter 1 is still producing V_1 and the CM voltage becomes equal to $-V_{dc}/6$. Inverter 1 is then shifted to V_2 for the next phase and zero CM voltage is achieved. The first half of the switching period is ended in the next step where inverter 1 is operating in zero vector V_7 and inverter 2 operates in the other zero vector V_0. The CM voltage remains zero. The same pattern is repeated for the last half cycle, but with reversed sequence.

The CM voltage will thereby have two pulses in one switching period which will have either a positive or negative amplitude of $\pm V_{dc}/6$. The difference between the active times t_1 and t_2 defines the total time of the pulse duration. The duration of t_1 compared to t_2 also defines whether or not the pulses are positive or negative. In the case of the V_{ref} being in sector 1, the CM voltage pulse will be negative if $t_1 > t_2$, while $t_1 < t_2$ will give a positive pulse. Overall, the interleaving scheme can reduce the CM voltage from $V_{dc}/2$ to $V_{dc}/6$ when compared to the conventional SVM scheme, but not eliminate it.

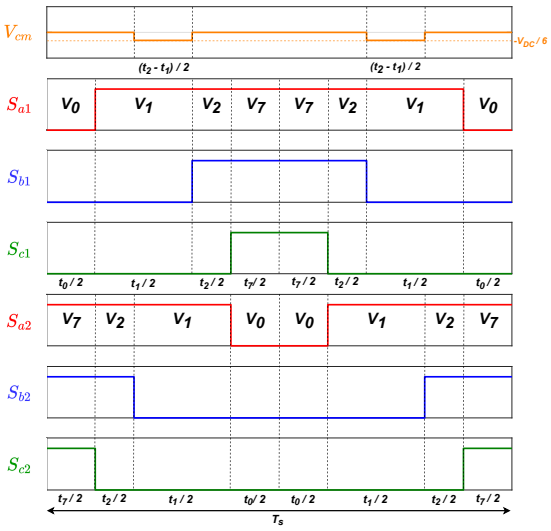

Figure 3.4: Convential SVM scheme with interleaving.

3.3.3 ZCMV PWM

The paper *"Common-Mode Voltage Reduction for Paralleled Inverters"* suggests a PWM strategy for two inverters working in parallel that theoretically would result in zero CM voltage. The article *Dual-Segment Three-Phase PMSM With Dual Inverters for Leakage Current and Common-Mode EMI Reduction* further analyzes the ZCMV PWM strategy by adjusting it and implementing it on a DTP machine with a winding displacement of 0°. The working principle of this scheme based on the two articles will be covered in this section.
If the two voltage vectors from the two inverters through a whole switching cycle contain three "1" and three "0" the resulting common mode voltage would be 0V. The general working principle behind the ZCMV PWM scheme is that the two inverters at all time are not using the same voltage vector but instead are operating with two adjacent voltage vectors pairs. As an example, when VSI 1 is in the state "100" producing V_1 , inverter 2 is either in state "110" to produce V_2 or in state "101" producing V_6 leading to three "1" and three "0". A total of 6 adjacent vectors pairs are possible and they are displayed in the hexagon in figure 3.5(a). Two zero vector pairs $V_1 + V_7$ and $V_7 + V_1$ are also available. When adding their switching states they both result in "111". The notation for a switching state of the adjacent vector pairs is that the vector V_1 "100" added to vector V_2's 110 gives $V_1 + V2$ = "210". E.g "2" means same switch on same half bridge of each inverter is "1". If the values of the vector are added, such that "120" =3, one notices that every one of the new vector pairs add up to three. Therefore, all vectors are a combination of three '1' and three '0' which fulfill the zero CM voltage criterion.
The combination of adjacent voltage pairs and zero vector pairs can be utilized to create the reference voltage vector. In figure 3.5 (a) the adjacent vector pairs also yield 6 new sectors in the vector plane and each sector is between two adjacent vector pairs. The reference voltage will be generated by two adjacent voltage vectors pairs in each sector. The active time spend on the adjacent vector pairs are defined as t_1 and t_2, while time spend on the adjacent zero vector pair is defined as t_0, just as conventional SVM.

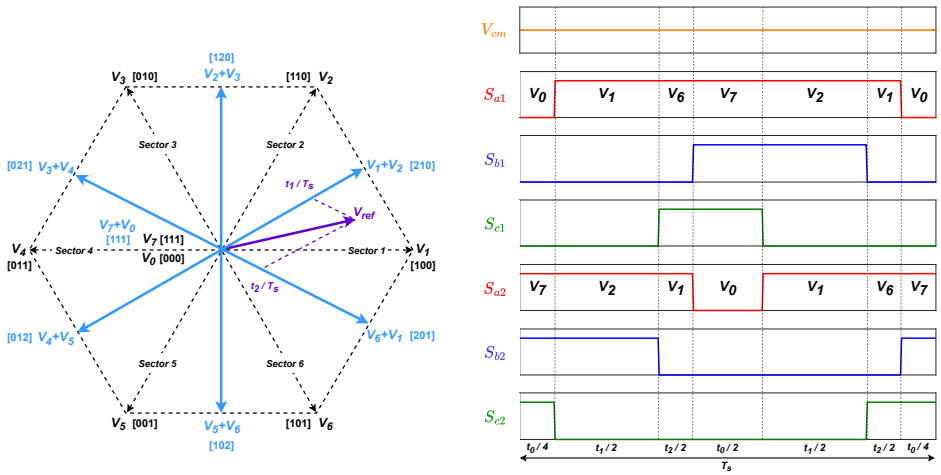

Figure 3.5: (a) Reference voltage synthesis with adjacent voltage vector pairs. (b) ZCMV PWM scheme in sector 1.

Figure 3.5 (b) shows the switching pattern to generate V_{ref} for the ZCMV scheme. The shown switching pattern is for one switching period. As the reference vector is placed in sector 1 adjacent vector pairs $V_1 + V_2$ and $V_6 + V_1$ are used. This leads to both inverters generating 3 active voltage vectors during a whole switching period. The ZCMV differs from SVM as it has asymmetrical pulse arrangement, which is necessary for the ZCMV PWM scheme. One drawback of the presented PWM scheme is that length of the adjacent voltage vector pair has a length that is $\sqrt{3}/2$ of the original voltage vectors, which leads to the maximum length of V_{ref} is reduced to $\sqrt{3}/2$ of SVM.

Vector time calculation and sector judgement

One key step in closed loop operation is to accurately judge which sector the reference voltage vector lies in. In the closed loop control of the motor, the reference vector is obtained from the dq voltages that is outputted from the current controllers. The corresponding abc phase voltage reference for both inverters can be obtained by inverse park transformation. The abc voltage references can be defined as:

$$\begin{cases} V_{a1}^* = V_{a2}^* = d_a^* \cdot V_{dc}/2 \\ V_{b1}^* = V_{b2}^* = d_b^* \cdot V_{dc}/2 \\ V_{c1}^* = V_{c2}^* = d_c^* \cdot V_{dc}/2 \end{cases} \tag{3.5}$$

Where d_a^*, d_b^* and d_c^* are the quasi duty cycles with a range of -1 to 1. The sector

can be determined by using the sign of two quasi duty cycles and the vector time can be calculated. As an example when the reference vector is in sector 1, d_b^* and d_c^* must be negative and the synthesized adjacent voltage vector pairs active times t_1 and t_2 and the time spent on the zero vector pair is calculated as follows:

$$\begin{cases} t_1 = -d_c^* \cdot T_s \\ t_2 = -d_b^* \cdot T_s \\ t_0 = (1 - d_a^*) \cdot T_s \end{cases} \tag{3.6}$$

Here T_s is the time of one switching period. All sector judgement condition and corresponding time calculation are displayed in table 3.2. When t_1, t_2 and t_0 are obtained the pulse generation for the six phase legs can be generated by comparing carrier waves to reference signals based on the t_1 t_2 and t_0.

Sector No.	Condition	Vector time calculation
1	d_b^* <0 & d_c^* <0	$t_1 = -d_c^* \cdot T_s$ $t_2 = -d_b^* \cdot T_s$ $t_0 = (1 - d_a^*) \cdot T_s$
2	d_a^* >0 & d_b^* >0	$t_1 = d_b^* \cdot T_s$ $t_2 = d_a^* \cdot T_s$ $t_0 = (1 + d_c^*) \cdot T_s$
3	d_a^* <0 & d_c^* <0	$t_1 = -d_a^* \cdot T_s$ $t_2 = -d_c^* \cdot T_s$ $t_0 = (1 - d_b^*) \cdot T_s$
4	d_b^* >0 & d_c^* >0	$t_1 = d_c^* \cdot T_s$ $t_2 = d_b^* \cdot T_s$ $t_0 = (1 + d_a^*) \cdot T_s$
5	d_a^* <0 & d_b^* <0	$t_1 = -d_b^* \cdot T_s$ $t_2 = -d_a^* \cdot T_s$ $t_0 = (1 - d_c^*) \cdot T_s$
6	d_a^* >0 & d_c^* >0	$t_1 = d_a^* \cdot T_s$ $t_2 = d_c^* \cdot T_s$ $t_0 = (1 + d_b^*) \cdot T_s$

Table 3.2: Sector judgement and active time calculation.

Pulse generation

Once the times have been calculated, the pulse generation are performed. The generation is done by comparing two carrier waves, one for each inverter, with four reference values calculated from the vector times. The carrier waves have an amplitude from -1 to 1 and they are shifted 180° from each other. The frequency of the carrier wave determines the switching frequency. Each reference value is

assigned to be accountable for the switch state of a phase leg. The state for a phase leg is "1" if the assigned value is bigger than the value of the carrier wave and "0" otherwise. The four values are calculated as follows:

$$\begin{aligned} \text{i} &= 1 - t_0/T_s \\ \text{ii} &= 1 - (t_0 + 2t_2)/T_s \\ \text{iii} &= 1 - (t_0 + 2t_1)/T_s \\ \text{iv} &= 1 - (t_0 + 2t_1 + 2t_2)/T_s \end{aligned}$$

Due to the pulse alignment being asymmetrical the reference value assigned to a gate signal changes between the half cycle with a positive gradient and the half cycle with a negative gradient of the carrier wave. For instance, in sector 1 reference value (i) is assigned to control $S_{a1,2}$ for both half cycles. For $S_{b1,2}$ (ii) is used for the positive gradient half cycle and switched to (iv) in the negative gradient half cycle. Lastly $S_{c1,2}$ uses (iv) for the positive and (iii) for the negative gradient of the half cycle. The division of half cycles of the carrier wave signal ensures optimal switching of the transistor as only the state of a half bridge is changed at a time for one inverter.

Figure 3.6 shows the comparator for sector 1 and the equivalent pulse generation. The reference value assigned to a gate signal also changes according to the sector resulting in different comparators for every sector. The comparator for the rest of the sectors are available in appendix D.

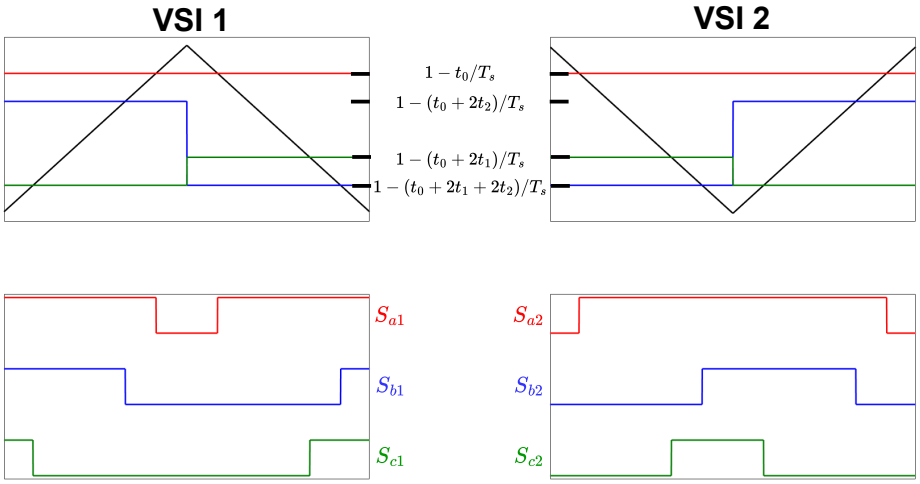

Figure 3.6: Comparator of sector 1.

The full sequence for the ZCMV modulation strategy, when integrating it to the control strategy, is as followed. The *dq* reference voltages from the current controllers are transformed to *abc* reference quantities. The *abc* voltages are used to calculate which sector the reference voltage vector lies in and the corresponding time segments, all according to table 3.2. The sector number and times are then passed on to the two comparators that decides the pulse generation and the gate signals are send to the two VSI's. The full overview can be seen in figure 3.7.

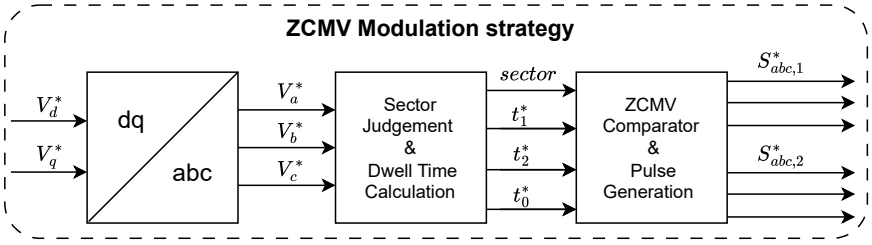

Figure 3.7: Control block diagram ZCMV modulation strategy.

Chapter 4

Prototype DTP Machine Parameter Characterisation

The motor investigated in this project is a Grundfos MGE100-LA Saver2-small, which is pictured in figure 4.1 (a). The Saver2 is a three-phase PMSM with interior mounted magnets, 36 slots and 3 pole pairs, which is in production at Grundfos. This motor was chosen due to its winding configuration, where each set of phase windings has a parallel path around the stator. The two parallel winding patterns are mirrored in the center axis, as seen in Figure 4.1 (b), where the $a1$ and $a2$ phases are positioned on separate halves of the stator, and the same applies to the other phase pairs. In the prototype delivered by Grundfos, this parallel connection has been split, resulting in the motor having two three-phase systems. The electrical phase shift between the two three-phase sets is 0°.

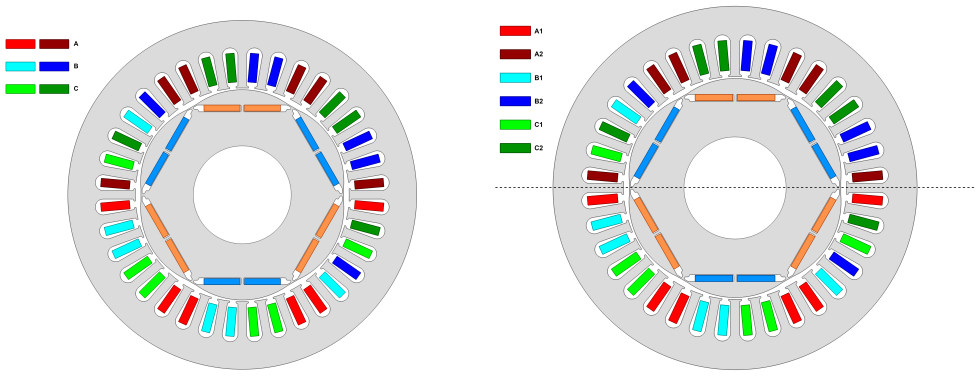

Figure 4.1: Machine structure and winding arrangement of Saver2 and the rewired DTP version.

One of the project objectives is to determine parameters of the machine and since

the machine is a prototype, the electrical parameters are unknown. The parameters in question is the PM flux linkage constant, inductances and phase resistance. The resistance is uncovered with a simple resistance measurement and the permanent magnet flux linkage is determined from a no load test of the machine where the back EMF is recorded. The inductance determination of a synchronous machine can be performed in different ways and the literature describes the measurement of the self-inductance in depth, but there is a lack of information regarding mutual couplings and especially within a double set configuration. The measurement of these couplings are crucial in understanding the operation of the machine and to correctly model and simulate its behavior. The chosen inductance measurement method is used to measure the inductances within a single set, and is modified to measure the additional couplings from set to set.

4.1 Simulated Parameters

In order to have a simulation to compare the measurements with, a simulation model of the motor has been made in the program Ansys Maxwell 2D, that uses finite element analysis (FEA) to solve electromagnetic field problems. The main objective of the simulation model is to simulate *abc* inductances and estimate *dq* inductances. Furthermore, the back EMF from all phases are simulated to ensure them being sinusoidal, symmetric, 120° phase shifted and to verify that the angular displacement of set 1 and set 2 are 0°. All the simulations are conducted with a shaft speed of 2900 rpm. When the back EMF is recorded the motor is simulated without current in the windings. For the inductance, the motor is simulated with rated current applied to the windings. A single electrical period are simulated for each test and 50 data points are collected. The back EMF results are presented in figure 4.2.

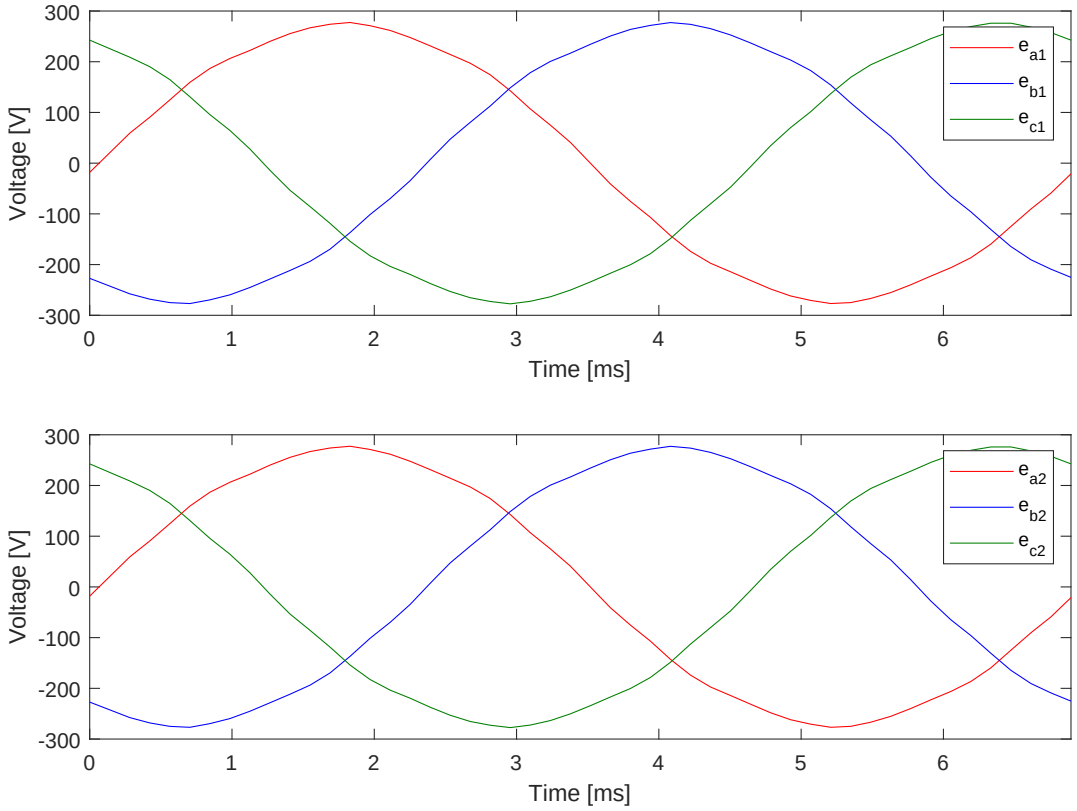

Figure 4.2: Simulated induced voltage in each winding set with $I_s = 0A$ from Ansys Maxwell

As seen on the figure, it is verified that the back EMF is sinusoidal, *abc* back EMFs are symmetrical and 120° shifted, and the displacement angle is 0°. From these data points the value of the PM flux-linkage can be calculated, as presented in appendix B and determined to be $\lambda_{PM,sim} = 0.3$ Wb.
With sinusoidal operation of the model verified, the inductances are simulated in the *abc* domain. In figure 4.3, the plot of all self-inductances are presented. The self-inductances show identical characteristics and the minimum and maximum inductance values occurs at the expected angle positions. Ansys Maxwell has the advantage that it can evaluate the self- and mutual inductances for each phase within both winding sets. By recording and extracting the inductance data for every *abc* inductance in an electrical period, it is possible to determine the *dq* inductances via reference frame transformation. The modified Clarke-Park transformation from equation 2.22 is applied to the data and the results is an electrical period of the *dq* inductances as seen in figure 4.4.

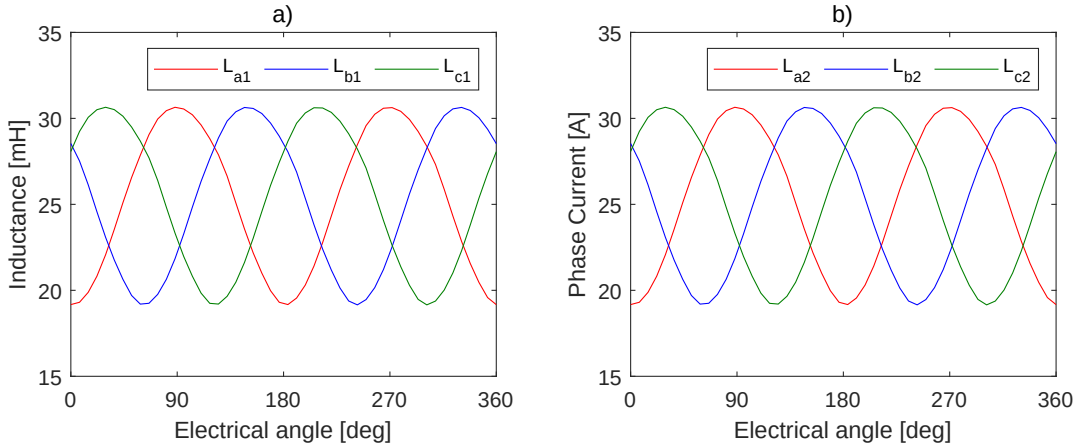

Figure 4.3: Simulated Self inductance for a) winding set 1 , b) winding set 2. from Ansys Maxwell

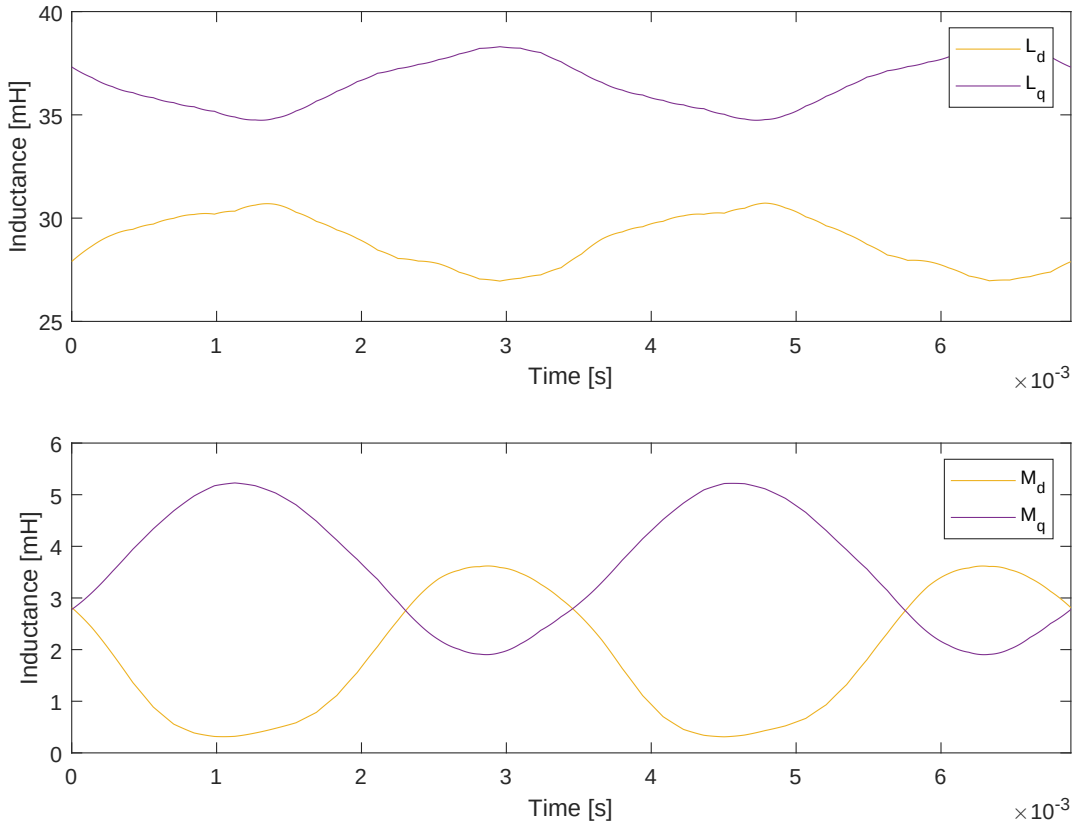

Figure 4.4: Simulated dq inductances from Ansys Maxwell

The inductances are not DC quantities. Therefore, the average values of each waveform in the figure are calculated to decide the values of L_d, L_q, M_d and M_q. This method of determining the dq inductances is referred to as the reference frame

transformation method. The average values of the dq inductances from the transformation are displayed in table 4.1.

Parameter	Value
L_d	28.88 mH
L_q	36.53 mH
M_d	1.88 mH
M_q	3.58 mH

Table 4.1: Average values of reference frame transformed dq inductances from Ansys Maxwell

4.2 Measured Parameters

A workflow similar to the simulation of parameters are employed for the measurement of the physical machine. Again, the first objective is to verify symmetric behavior of the machine, phase shift and angular displacement, which is proved by a no load back EMF test. Upon assembling the first test setup the phase resistance was also measured for each phase. The inertia is not measured and the value from the manufacturer is used. The viscous friction is not characterised either, as the effect of this parameter is negligible.
The prototype has all leads exposed, meaning there is access to both ends of all six leads, which makes for easy measurement of individual phases. The first test setup used is visualised in figure 4.5.

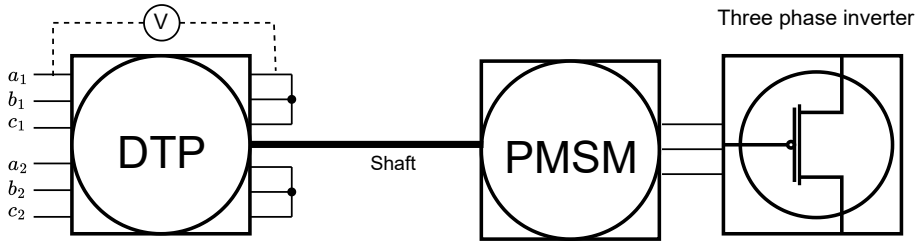

Figure 4.5: Test Setup 1: Back EMF Test of DTP Machine.

In this test setup the PMSM acts as a variable speed machine controlled using the dSPACE interface and the motor is driven at a constant speed. The back EMF induced by the PM in the DTP is measured between the phase terminals and the related neutral point. The test was performed at three different speeds: 500, 1500 and 2900 rpm and the results of the second test is presented in figure 4.6.

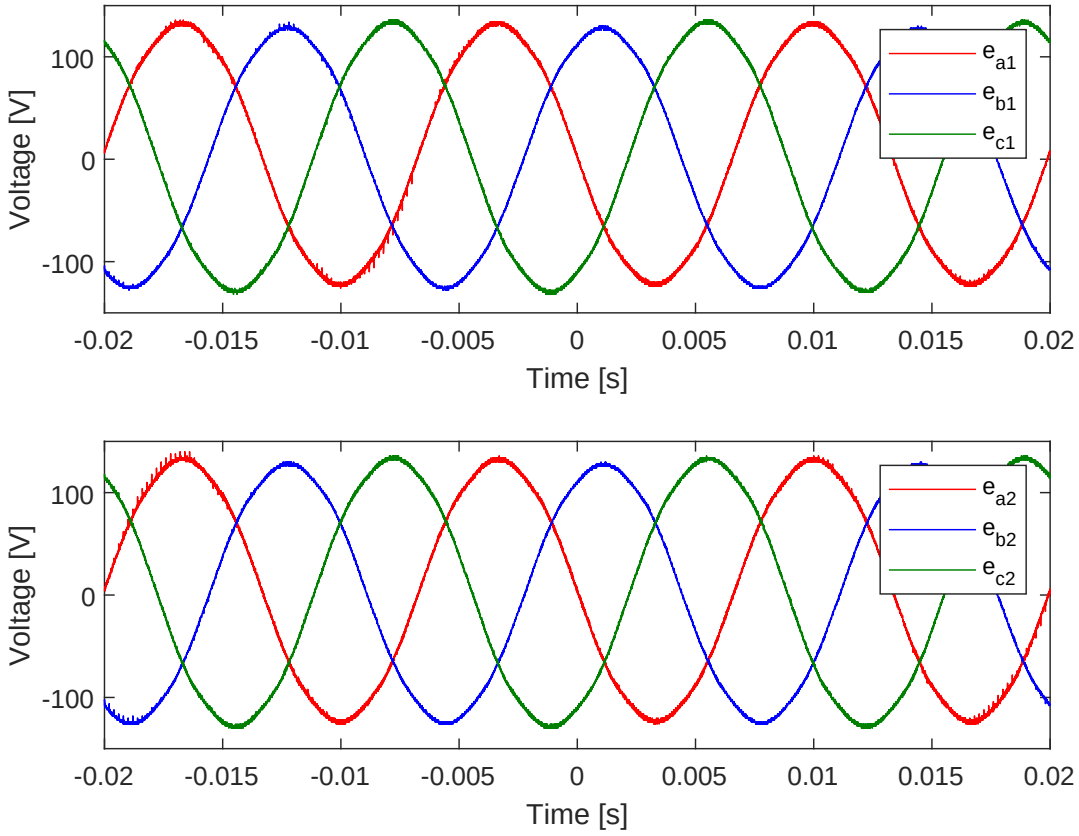

Figure 4.6: Induced voltage measured at DTP terminals in each winding set, at 1500 rpm.

The top plot is the voltage of the first set of windings and the bottom is the second set. From the sequence of voltages, it is verified that the labeling of the terminals are correct and that all phases are functional. The shape of the voltages is sinusoidal and the system is balanced as seen on the equal magnitude of all six phases. The parallel configuration of the two sets of windings shows in the plot as there is no angle displacement between the two sets. The flux-linkage from the PM was determined in appendix A.2 at the value of $\lambda_{PM} = 0.274$ Wb, which is 8.6% lower than the simulation. The difference might originate in the simulation being a calculation on the back EMF behavior in an ideal system. The difference is not investigated further and the PM flux-linkage constant obtained from the measurement is chosen as the parameter value.

4.3 Inductances

The inductance measurement follows the method called "Simple AC Measurement Method"[6], where a single stator phase is supplied by an AC voltage and the instantaneous voltage and current is recorded. Like the first test setup, access to both ends of all phases is crucial, as it allows for the excitation of one phase at a time. The phase is excited by an AC source connected to one of the stator phases as illustrated in figure 4.7.

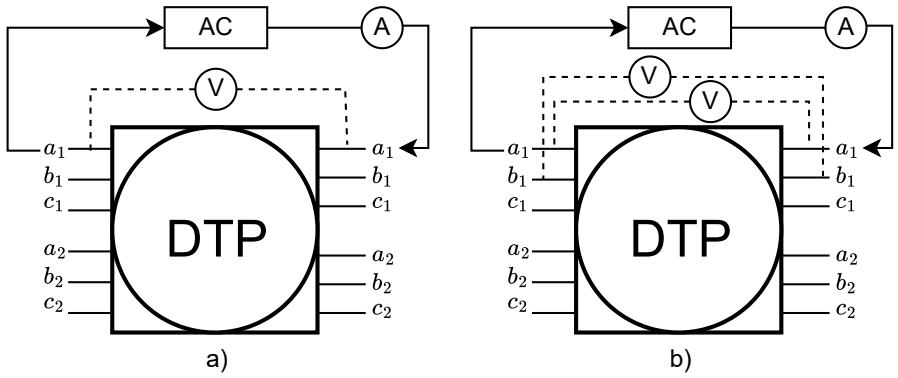

Figure 4.7: Test setup 2. a) self-inductance measurement phase a_1, b) mutual-inductance phase a_1 to b_1. Voltage and current measurements is pictured as V A in a circle.

In test setup 2 a), the voltage u_{in} and the current i_{in} applied to the phase under test is recorded. The equivalent of this circuit is shown in figure 4.8.

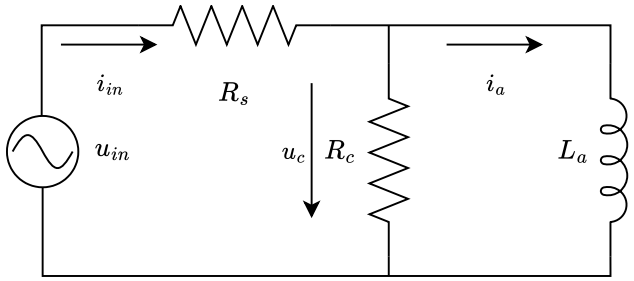

Figure 4.8: Equivalent circuit for measurement at steady state with AC excitation [6].

The objective is to calculate the current i_a through L_a which represents the inductance of the phase and to identify the voltage u_c which is the voltage drop across the parallel RL branch. Integrating this voltage yields the flux linkage and the flux linkage current curve can be plotted.

The test is performed at an input frequency of $50Hz$ and the data is captured during steady state. A single electrical period is extracted from the data and the fundamental signal of the current and voltage is calculated using an FFT, which yields a filtered signal. The core loss of the circuit is defined by the input power, input current and phase resistance. Using the core loss, the equivalent core resistance is determined and the currents in the parallel branches can be found. Hereafter the voltage u_c is integrated and the flux-linkage current curve can be drawn4.9. The full step by step calculation is available in appendix A.3.

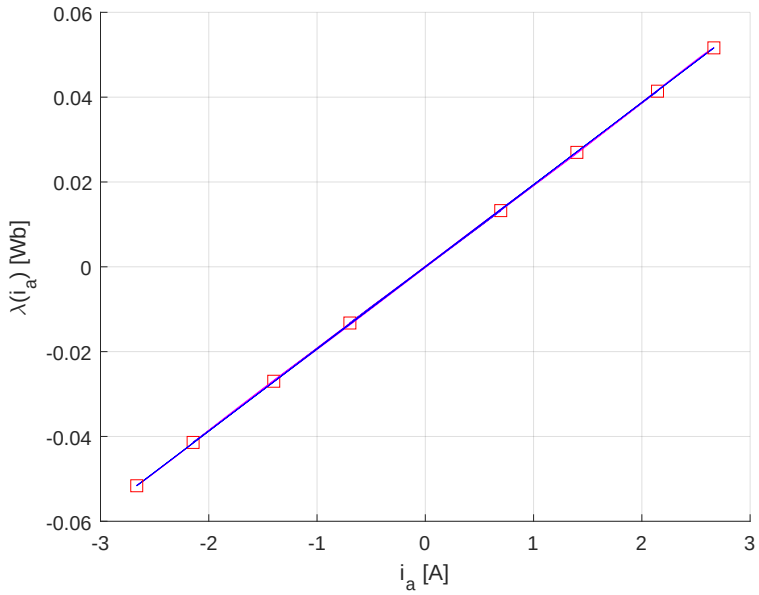

Figure 4.9: Flux linkage current loops of one rotor position, at different values of input current.

The above figure presents multiple datasets, each corresponding to increasing input current. The red dots indicate the vertices of the flux-linkage current loop. The two inner dots represent a pair of resulting minimum and maximum flux linkage values, and as the input current rises, these dots spread further apart. Since all measurements are aligned with increasing input current, there is no saturation, making the measurements within this current range suitable for inductance determination.
Performing a linear curve fitting and extracting the slope of the data yields an inductance value. When performing all the above for many different rotor positions the inductance as a function of rotor position can be drawn 4.10.

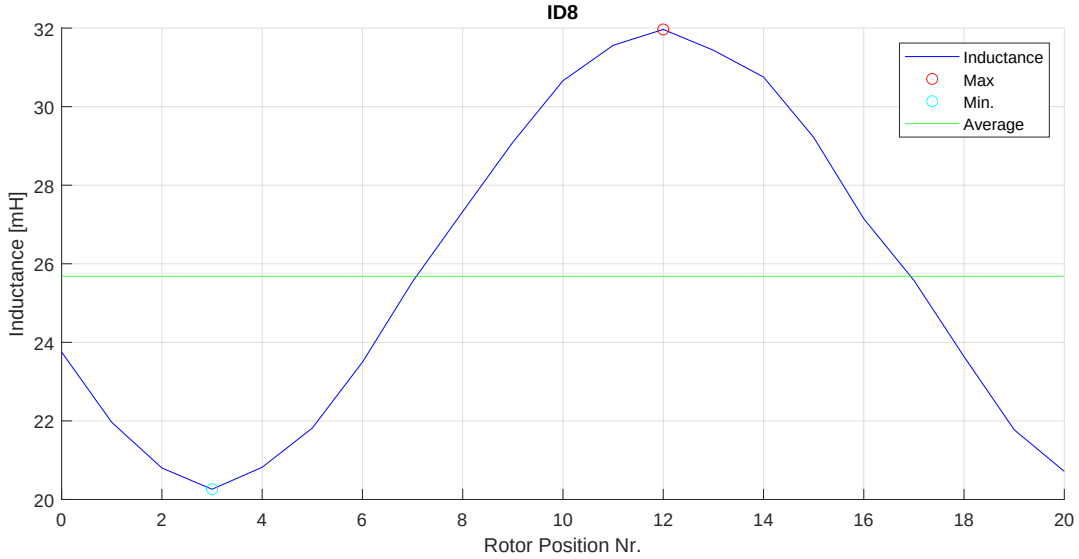

Figure 4.10: Phase $c1$ self-inductance as a function of rotor position. The x-axis is the number of different rotor positions.

The self-inductance of phase c_1 is pictured and the minimum, maximum, and average values of the inductance are recorded. The self-inductance is measured in several phases and the average value of all measurements represents the general parameter value, which is determined to be $L_s = 25.69$ mH. The data and calculation can be found in appendix A.3.
The measurement of the mutual inductance follows the same course of action as for self-inductance. However, the test setup 2 in 4.7 b) features an additional voltage measurement that captures the voltage induced in the winding under test. The extended equivalent circuit for mutual inductance measurement is seen in figure 4.11:

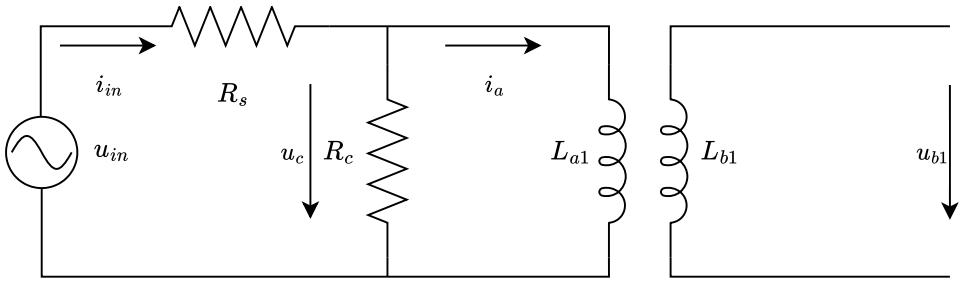

Figure 4.11: Extended equivalent circuit for mutual inductance measurement at steady state with AC excitation. This example is measuring the mutual inductance from phase $a1$ to $b1$.

In the diagram the current i_a is the flux-linkage producing current in phase $a1$ which induces a voltage in the second phase called u_{b1}. This current and the

induced voltage is used for calculating the flux-linkage vs current curve of the mutual inductance. All measurements are processed in appendix A by averaging the values of all symmetric inductances. In addition, the leakage inductance is also determined using the relation between self-inductance, average magnetization inductance and leakage inductance. All coefficients are presented in table 4.2.

	Single Set		Set to Set		Leakage	
Inductance	L_A	L_B	M_A	M_B	L_{ls}	Unit
Avg.	12.06	3.92	3.03	0.90	13.63	mH

Table 4.2: Average magnetizing inductance, average peak second harmonic and leakage inductance.

With the coefficients determined, the equations 2.23 from chapter two are used to calculate the *dq*-inductances from the measurements. In addition, the FEA simulated *abc*-inductances from figure 4.3 is also calculated using the same equations. The results are provided in 4.3.

	FEA Transformed	FEA Calculated	Measurement	Unit
L_d	28.88	27.50	25.83	mH
L_q	36.53	37.81	37.60	mH
M_d	1.88	1.78	3.18	mH
M_q	3.58	3.88	5.89	mH

Table 4.3: *dq* inductances from modified Clarke-Park transformation, calculated simulation and calculated measurements.

The tables features the reference frame transformed results from the table 4.1, the results from the FEA simulated *abc*-inductances and the results from the measurements. As anticipated, all *q*-axis inductances is larger than the *d*-axis inductances. Although there are minor differences between the outcomes, they are generally acceptable. The results presented in the table verifies the FEA simulation as being descriptive of the physical system and the coefficients from the measurement column is chosen as machine parameters.
It is preferable to calculate the simulated *dq* inductances using the same method as for the measured values, for the purpose of comparing the results, as demonstrated in the above table. Because the FEA simulation is validated in the above table, and the FEA reference frame transformed results also aligns with these results, this suggests that the modified Clarke-Park transformation is verified. With the inductances in place, the machine parameters needed to describe the motor behavior is completed.

4.4 Prototype DTP Machine Parameters

The electrical and the mechanical ratings are all listed in the table below 4.4. On the right-hand side of the table is the reference column, which indicates the appendix chapter that describes the raw data and calculations that results in the parameters that needed to by determined. The rest of the table is from datasheets.

Parameter	Symbol	Value	Unit	Reference
Rated Voltage (Line-line)	V_n	380	V	[18]
Rated Current	I_n	2.9	A	
Rated Power	P_n	3	kW	[18]
Rated Torque	T_n	9.9	Nm	
Rated Speed	n_n	2900	rpm	
Stator Resistance	R_s	2.44	Ω	A.1
Stator Inductance	L_s	25.69	mH	A.3
Flux Linkage from Permanent Magnets	λ_{PM}	0.274	Wb	A.2
Moment of Inertia	J	0.004	Kgm^2	
Number of Pole Pairs	N_{pp}	3	-	

Table 4.4: Parameters for DTP Machine.

The machine prototype is pictured below in figure 4.12. On the right side of the terminal block, the two winding sets with three phases each are placed, while on the left-hand side, the phases are connected to the two separate neutral points.

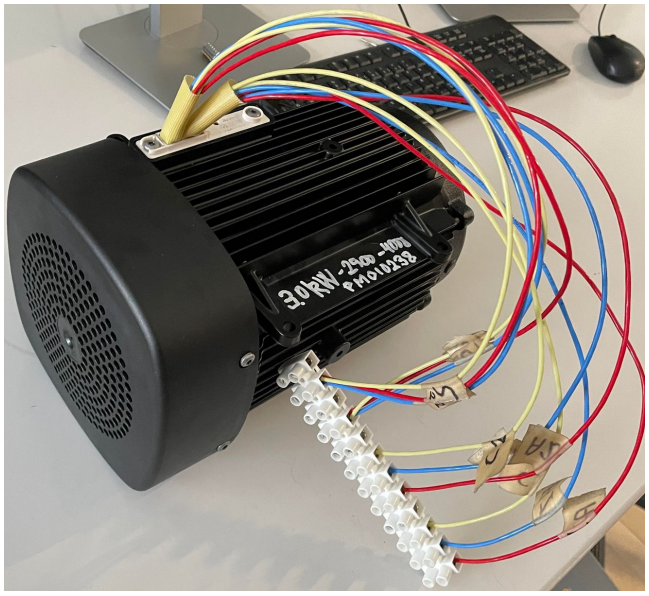

Figure 4.12: Grundfos MGE100-LA Saver2-small rewired to a DTP prototype.

Chapter 5

Implementation of Control

In this chapter, the physical system and its control are presented. Firstly, the conventional FOC is introduced, and the flow of information is highlighted in a block diagram. A simulation of the system, including the DTP and the inverters is presented.
Secondly, the experimental test setup is introduced through pictures and using a schematic overview of the setup. The setup is built in two different forms: one with two different DC links and one with a shared DC link. Results from simulation and experimental setup are compared.

5.1 Vector Control Method

Field Oriented Control (FOC) is a type of vector control used for instantaneous torque control of an AC motor [13]. The aim for FOC is to control the torque and magnetic flux separately. This is realised by reference frame transforming the stator current into dq-quantities and achieve independent control of i_d and i_q. The torque production of a PMSM is dependent on the size and direction of the stator current vector and therefore also the size of i_d and i_q. It is of interest to find the smallest stator current vector i_s which produces the most torque. This is known as Maximum Torque Per Ampere (MTPA) operation[19]. Implementing this operation on an IPMSM where the inductances are unequal $L_d \neq L_q$, requires a revisit to the torque equation 2.32 from previously.

$$T_e = \frac{3}{2} N_{pp}(\lambda_{pm}(i_{q1} + i_{q2}) + (L_d - L_q)(i_{d1}i_{q1} + i_{d2}i_{q2}) + (M_d - M_q)(i_{d1}i_{q2} + i_{d2}i_{q1})) \tag{5.1}$$

In contrast to a SM-PMSM, which only generates magnetic torque, the IPMSM also produces reluctance torque. Therefore the electrical torque equation consists of

two terms. The magnetic term is only dependent on q-axis currents, which is the flux-producing current linking with the flux from the rotor PM's. The reluctance term is dependent on a combination of d- and q-axis currents and since $L_d < L_q$ for the DTP machine, the d-axis currents has to have negative polarity to have the reluctance positively contribute to the torque [13].
Unfortunately, as the main focus of the project has not been efficient control of the DTP this form of IPMSM MTPA control has been neglected. The MTPA method used in this project is the proposed method for a SM-PMSM. With no difference in dq-inductances in such machine, the electrical toque equation can be reduced to the following:

$$T_{e,tot} = \frac{3}{2} N_{pp}(\lambda_{PM}(i_{q1} + i_{q2})) \tag{5.2}$$

The aim is to control i_d to be zero as any d-axis current only will lead to extra copper losses and will yield no torque, in an SM-PMSM.
The result of running the IPMSM in this manner is a less efficient control as the reluctance torque of the machine is not utilised. However, one can easily run the machine using this method and the block diagram to control the machine is presented in 5.1. Note that only SVM has been used for testing the FOC in this chapter.

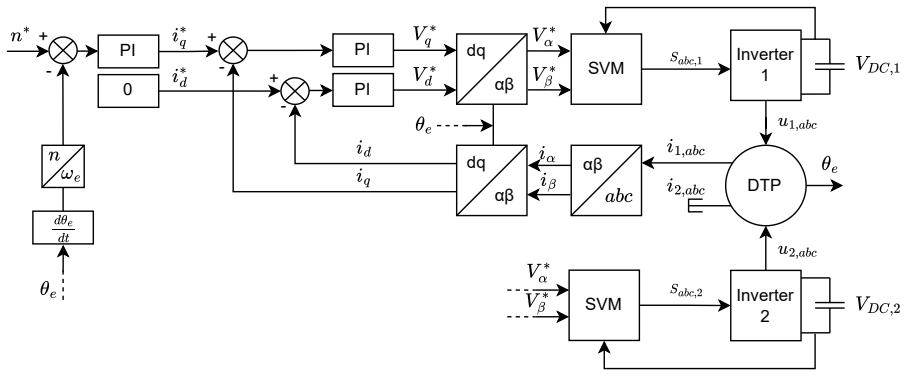

Figure 5.1: Block diagram of FOC implemented on the experimental setup.

This diagram shows how this FOC uses a total of three PI controllers. From left side, the first PI controller is introduced which is used for speed control. The PI controller searches to minimize the error between the speed reference and the measured speed, by controlling the stator current vector. Since the stator current is controlled by i_d and i_q, a PI controller is used for each dq current. These controllers are referred to as the current controllers.

The speed controller is connected in a cascade structure to the q-axis current controller, where the output of the speed controller is the reference to the q-axis current controller. The reference for the d-axis current controller is set to 0.
The output of the current controllers are the dq voltage commands that the inverter is responsible to produce. The voltage commands are fed to the inverter using SVM. Only the current measurements from the first set of windings is used in the current feedback loop.

5.2 Simulation model

A simulation model of the DTP with FOC has been made in MATLAB/Simulink. The model consist of a motor block simulating the DTP IPMSM and it is constructed with transfer functions based on the voltage equation in the dq frame presented in section 2.4. The parameters for the motor model is equal to the ones obtained in the laboratory, which was found in chapter 4.

The motor model has been modified to allow control using two inverters, enabling the implementation of the three different PWM schemes in the simulation model. The inverters are from the Simulink package *Simscape Electrical* and use IGBTs as transistors. The model is used to perform steady state and dynamic tests in order to verify the motor model against the experimental data gathered from the laboratory. The FOC block, containing the speed and current controllers, are called with an interrupt routine matching the sampling frequency of the physical system to simulate the experimental test setup as precise as possible.

5.3 Experimental Setup

The 'Drives Control Laboratory' at AAU Energy features several motor drive test stands with a PMSM and an induction machine acting as a variable load. The two machines are supplied by two separate inverters, which are controlled using the *dSPACE DS1103* system, that is programmed via MATLAB/Simulink environment [20]. This enables the user to draw block diagrams in Simulink and deploy them to the test setup via dSPACE. In figure 5.2 a screenshot of the ControlDesk UI is presented. The UI enables the user to modify variables in the control and plot measurements in real time.

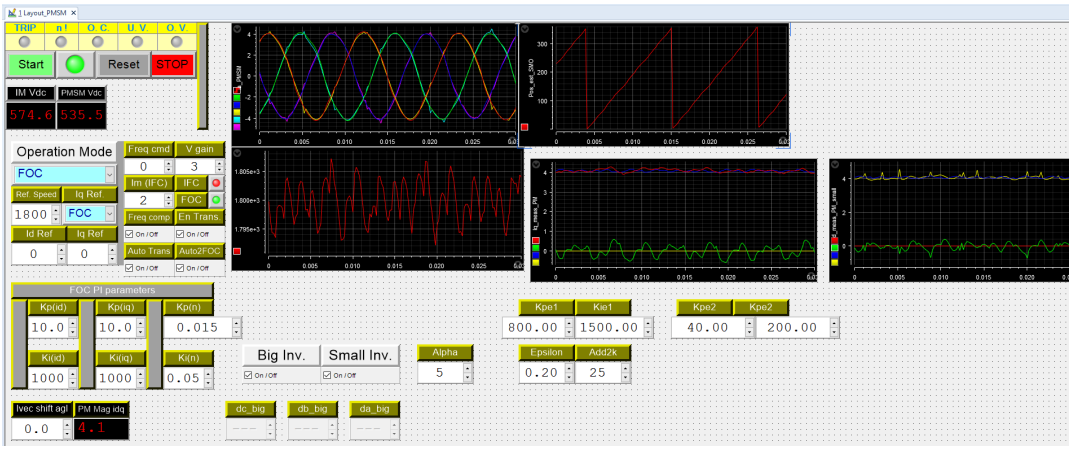

Figure 5.2: Screenshot from ControlDesk UI.

In addition to modifying the UI to fit the setup, the physical setup is also modified compared to the standardised test bench. The induction machine is replaced by the DTP machine and the two inverters is wired to a set of windings each in the DTP machine. This leaves the PMSM machine to act as a load by operating as a generator dissipating the energy into a variable transformer and a power-resistor bank. The load torque can be adjusted by changing the current flowing into the resistor bank using the variable transformer. The torque is calculated based on the power dissipated in the resistors and the mechanical speed. The test setup is sketched in figure 5.3.

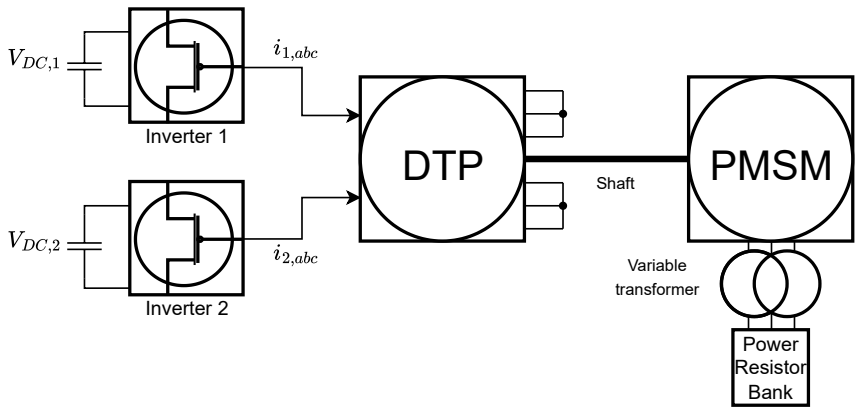

Figure 5.3: Test setup for FOC on DTP.

The two inverters are positioned on the left hand-side and are labeled *inverter* 1 & 2. This highlights that the two inverters are not identical, as one is rated for 15 kW and the other for 2.2 kW. [20]. Furthermore, the DC links are separate and are also

not identical. The experimental test setup for FOC on DTP is pictured in 5.4.

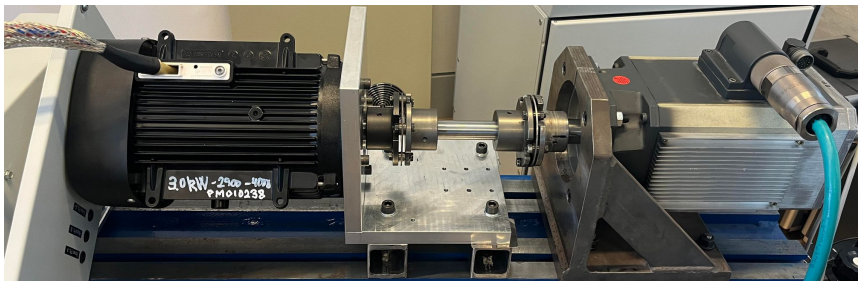

Figure 5.4: Experimental test setup for FOC. Left-hand side is the DTP and right-hand side is the PMSM.

Figure 5.5: From left to right: the two inverters, the transformer and the power-resistor bank.

It was underlined in the literature study 1.1, that the under underlying idea to enable simple transition from conventional three-phase to DTP, is that every aspect of the system is identical. The test-bench available for use unfortunately comes with two different inverters and DC links. When controlling the system according to figure 5.1 and feeding the exact same duty cycles to the inverters, the results is non-identical as seen in figure 5.6 *a)*.

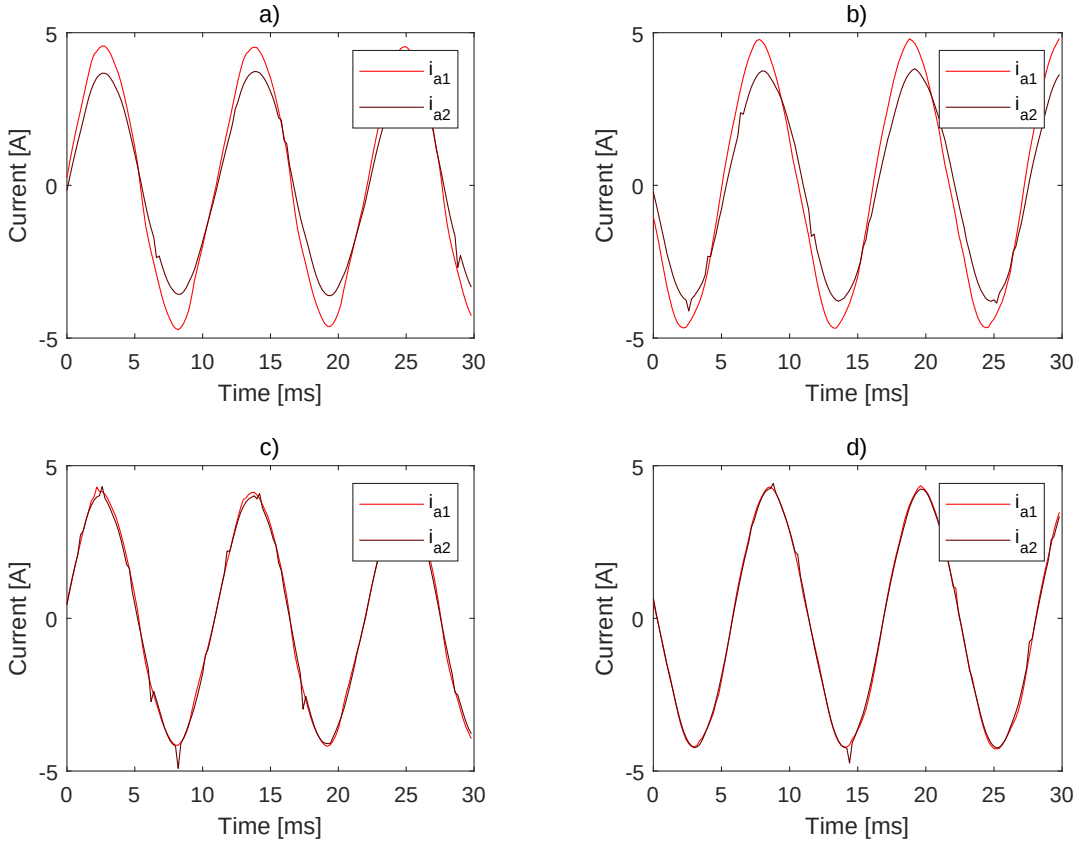

Figure 5.6: Current differences from set to set, with different controller and DC link configurations. a) One controller, two DC links. b) One controller, one DC link. c) Two controllers, two DC links. d) Two controllers, one DC link.

The phase-*a* currents from each set (i_{a1}, i_{a2}), is expected to be identical in phase and amplitude, but shows difference. The investigation into where this difference is rooted starts by verifying that the machine operation is correct and is able to produce identical currents it both sets. Therefore, a second current control loop is deployed for set 2, that uses the current and DC link measurements from set 2 as feedback.

The two currents control loops receives the same current reference from the speed controller and the results of using two controllers and two DC Links is presented in figure 5.6 *c)*. The system is able to produce identical currents from the two sets, which points to the machine operating under normal conditions. Next step is to investigate the DC link voltage. Normally, the test bench configuration features separate DC links, as one inverter is grid connected by a bi-directional converter, whereas the other is connected via a full bridge rectifier. The voltages is therefore not equal with the values of approximately 540V and 580V. The test setup is rebuild to feature a DC link comprised of two DC sources in series, with

the resulting voltage of 540V 5.7.

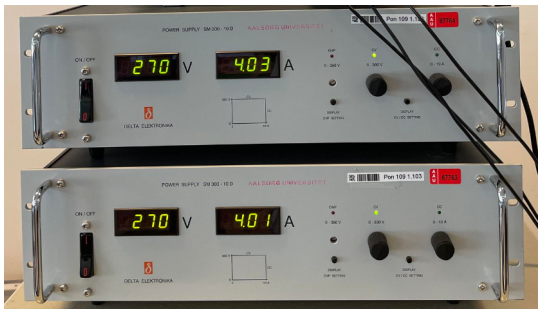

Figure 5.7: DC link by two DC sources in series.

In addition, this configuration also enables the midpoint of the the two sources to be accessed, which is used for CM voltage measurements. The result of using a single DC link voltage and a single current loop is presented in figure 5.6 *b)*. The results is exactly the same with a single DC link as for two. Again, the two controller configuration is deployed and the results is shown in *d)*. The two-controller configuration shows identical currents and therefore it can be excluded that the difference stems from the DC link. The last variable in the entire system, which is not identical is the inverters. As mentioned previously, the test stand features two different inverters. Because of time constraints, it was not possible two rebuild the cabinet and install to identical inverters. If the system would still produce currents of unequal magnitudes with two identical inverters, the system might have unbalanced current sharing, as some literature suggest [2]. In order to produce results the implementation settled on a two controller and one DC link configuration, as this behaved like the simulation model. The resulting control diagram is expanded as shown in 5.8, which is the control that was implemented on the setup.

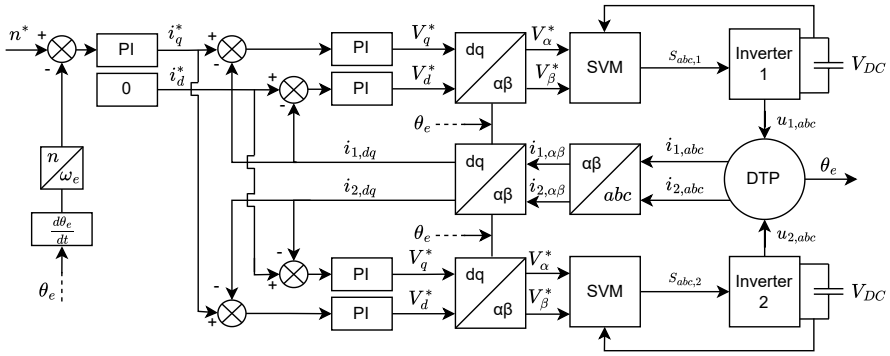

Figure 5.8: Block diagram of FOC using two current control loops.

5.4 Results

To verify the FOC and the model, the simulation and measurements are compared. The PI parameters for the speed and current loops where determined by manual tuning on the test bench. The parameters are presented in table 5.1.

	Speed	i_d	i_q
K_p	0.015	10	10
K_i	0.05	1000	1000

Table 5.1: PI parameters for FOC.

The results show steady steady operation and dynamic performance. The scope of the project is not efficiency or dynamic performance, however the control needs to be verified. The criteria for passing the tests are listed below:

Test	**Criteria**	**Conditions**
Steady State	Balanced currents, DC i_{dq} currents	1800 rpm, 9.4 Nm
Speed Ramp	Max. 2% OS	0-1800 rpm, 9.4 Nm
Load Step	Step 0-9.4 Nm	1800 rpm

Table 5.2: FOC test criteria.

The steady-state is tested by examining the speed and i_{dq} currents, as these are fundamental to the speed and current control loops. The *abc*-currents must be sinusoidal and equal in both sets. In addition, the *dq*-currents must resemble DC quantities as this is expected in the rotating reference frame.

The load torque is limited by the current limit of the power resistor bank and the torque rating of the DTP. At the operating speed of 1800 rpm, the maximum possible load torque, without exceeding the current limit of the resistor bank and the torque rating, was found to be 9.4 Nm.
In the speed ramp it is expected that the machine follows the ramp without oscillations and does not overshoot the final set point by more than 2%. The test is performed at full load of 9.4 Nm. The load step is performed when the machine is running at 1800 rpm in steady state and the load is stepped from 0-9.4 Nm. It is expected that the machine does not lose stability and regains speed to the set point of 1800 rpm.
In figure 5.9, the simulated steady state operation at 1800 rpm and a load torque of 9.4 Nm is presented.

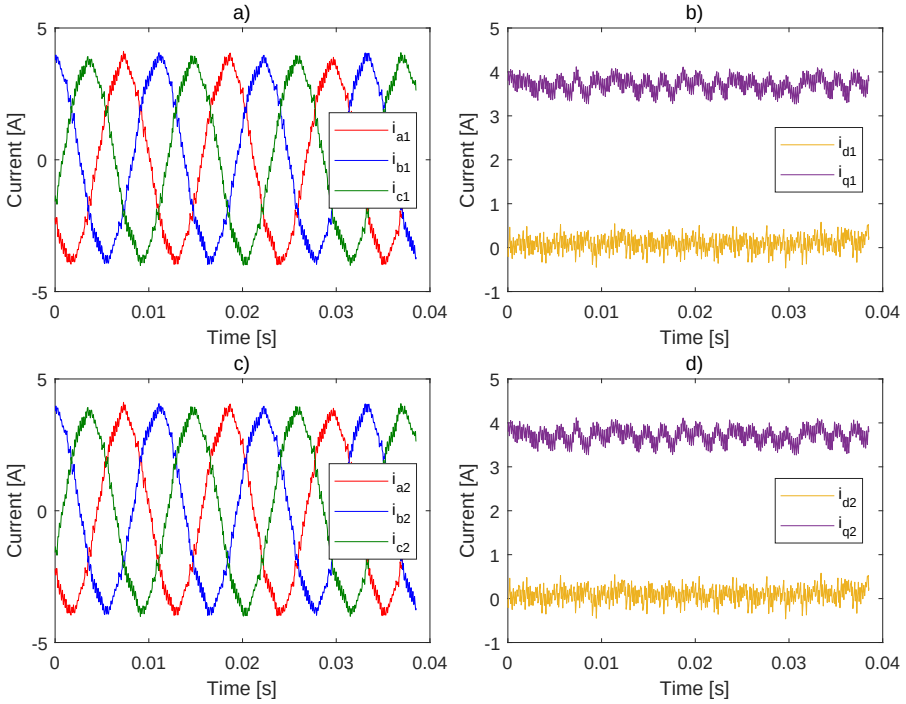

Figure 5.9: FOC steady state simulation. a) set 1 *abc* currents. b) set 1 *dq* currents. c) set 2 *abc* currents. d) set 2 *dq* currents.

The *abc* currents are sinusoidal and in phase for both sets, displaying no angular displacement between them. The high-frequency content in this simulation can stem from various sources, such as solver configuration or the switching action of the simulated inverters. However, this does not affect the validity of the results as they meet the steady state test criteria. The same applies to the *dq* currents, which exhibit the characteristic behavior of resembling DC quantities under steady-state conditions. The measured steady state results are presented in 5.10.

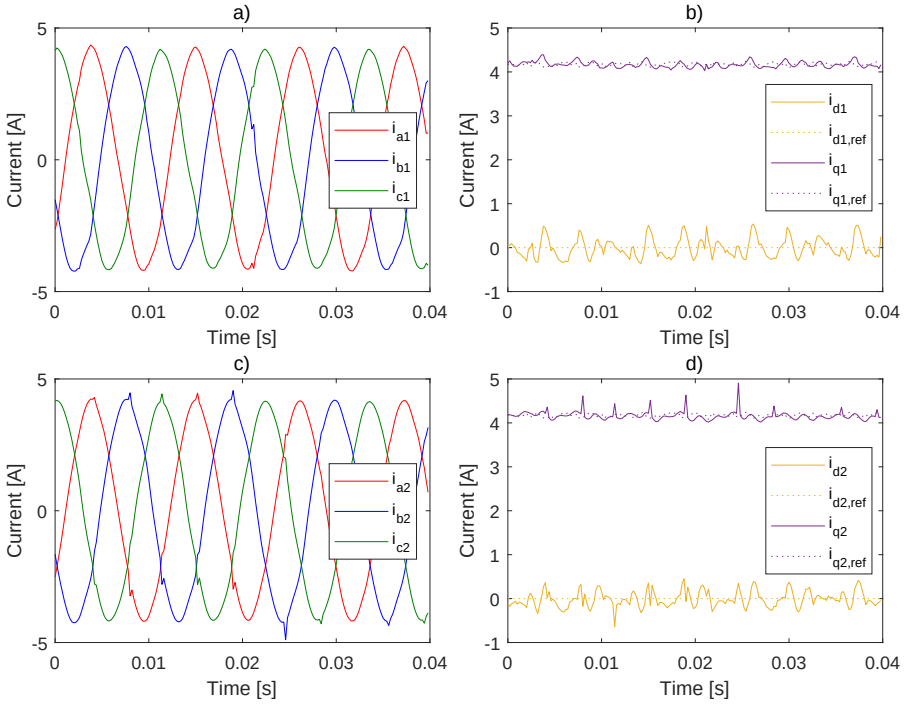

Figure 5.10: FOC steady state measurements. a) set 1 *abc* currents. b) set 1 *dq* currents. c) set 2 *abc* currents. d) set 2 *dq* currents.

The measurements shows smooth *abc*-currents in both sets, once again without angular displacement between sets. There is a small amount of noise in both sets, which could stem fromvarious sources. However, the amount and magnitude of this interference certainly does not compromise the validity of the results. The *dq*-current are tracking the set points and are within acceptable range in terms of oscillations. Furthermore, when the motor is operating at steady state with a load torque of 9.4 Nm, only small deviations in *dq* currents exist between the simulated and measured results. This further validates the motor model and the parameters found for the motor.
In figure 5.9 the speed ramp and load step for both the simulation and the measurements are presented.

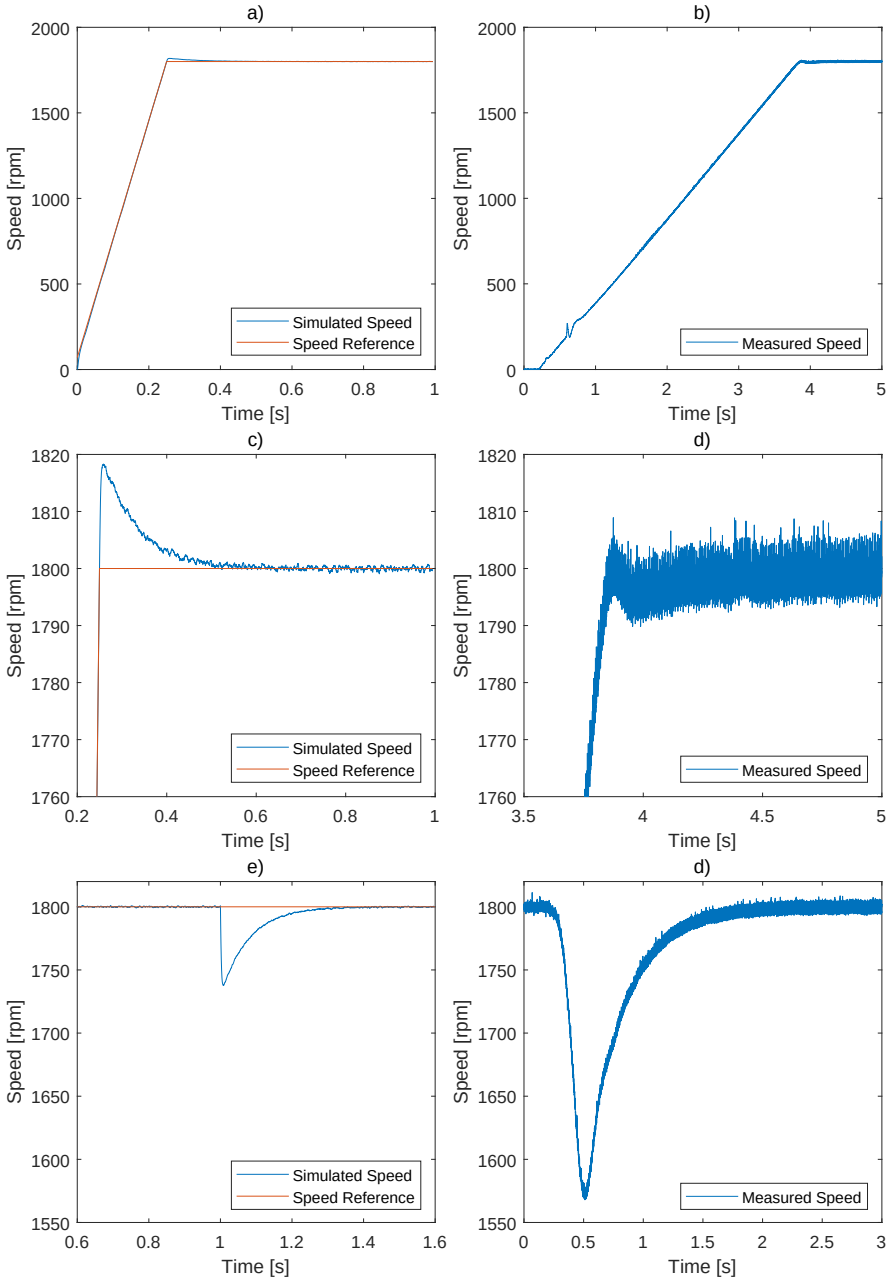

Figure 5.11: FOC results. a) simulated speed ramp. b) measured speed ramp. c) zoom - simulated speed ramp. c) zoom - measured speed ramp. d) simulated torque step. e) measured toque step.

The simulation and the physical machine can handle both speed ramping and load step. The top plot shows the entire ramping period, while the second row is a

zoomed view of the ramp reference ramp reaching the final set point. At plot e) it can be seen that the simulation overshoot the reference value by 1% and the measurement overshoot is even less. With the load step the simulation shows a speed decrease of 50 rpm, whereas the measurements decreases by over 200 rpm. None of them loses control and they both stabilises back to the reference speed of 1800 rpm. By these results the simulation and measurements is passing the test criteria. Moreover, the data also shows a clear resembles between simulation and implementation which verifies the simulation as a representation of the physical system.

Chapter 6

Implementation of PWM strategies

This chapter will describe the implementation of the three PWM schemes presented in chapter 3. First, the PWM schemes are implemented on the Simulink model to verify that they work in combination with the FOC. The currents will be evaluated to ensure that equal current distribution is obtained and the resulting CM voltage produced by each strategy is measured to verify the theory. Finally, the measurement obtained on the laboratory setup will be showed.

6.1 Simulation

All three schemes was able to control the motor and handle dynamics. As the equal current distribution and CM voltage are of interest and not the dynamics, all plots showed regarding the CM voltage and the current distribution are at steady state operation. The simulation is performed with a speed of 1800 rpm and a load torque of 9.4 Nm. The switching frequency for all three schemes is 5 kHz and DC-link voltage is 540 V. All PWM strategies are simulated with one current loop control and the inverters modulates the same voltage reference vector.

6.1.1 SVM with synchronized pulses

Figure 6.1 a) and b) shows the simulated CM voltage for SVM where identical pulses are sent to inverter 1 and 2. Plot a) verifies that the CM voltage reaches a maximum of $\pm V_{dc}/2 = \pm 270V$ as expected and b) shows the zoomed plot of V_{cm}. The zoomed-in view illustrates how the CMV changes each time the inverters switches to a new state.

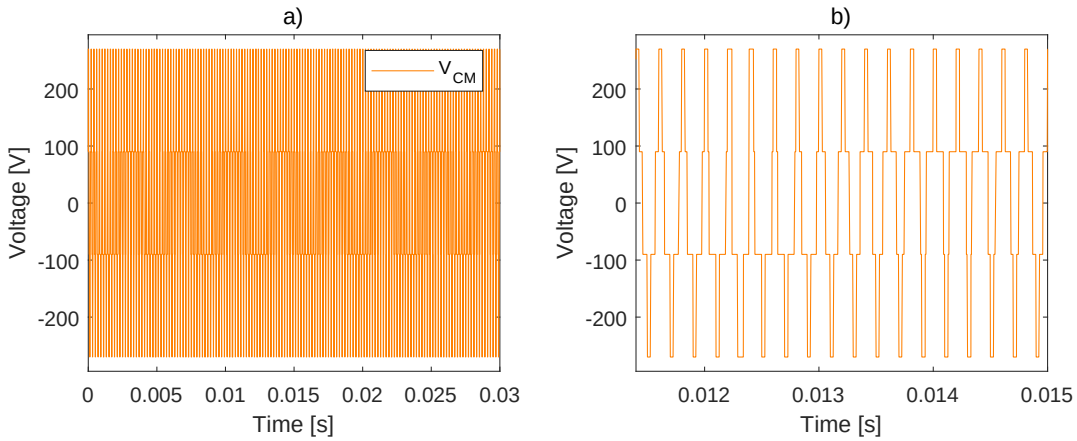

Figure 6.1: a) Simulated CM voltage with synchronized SVM operation b) With zoomed time axis.

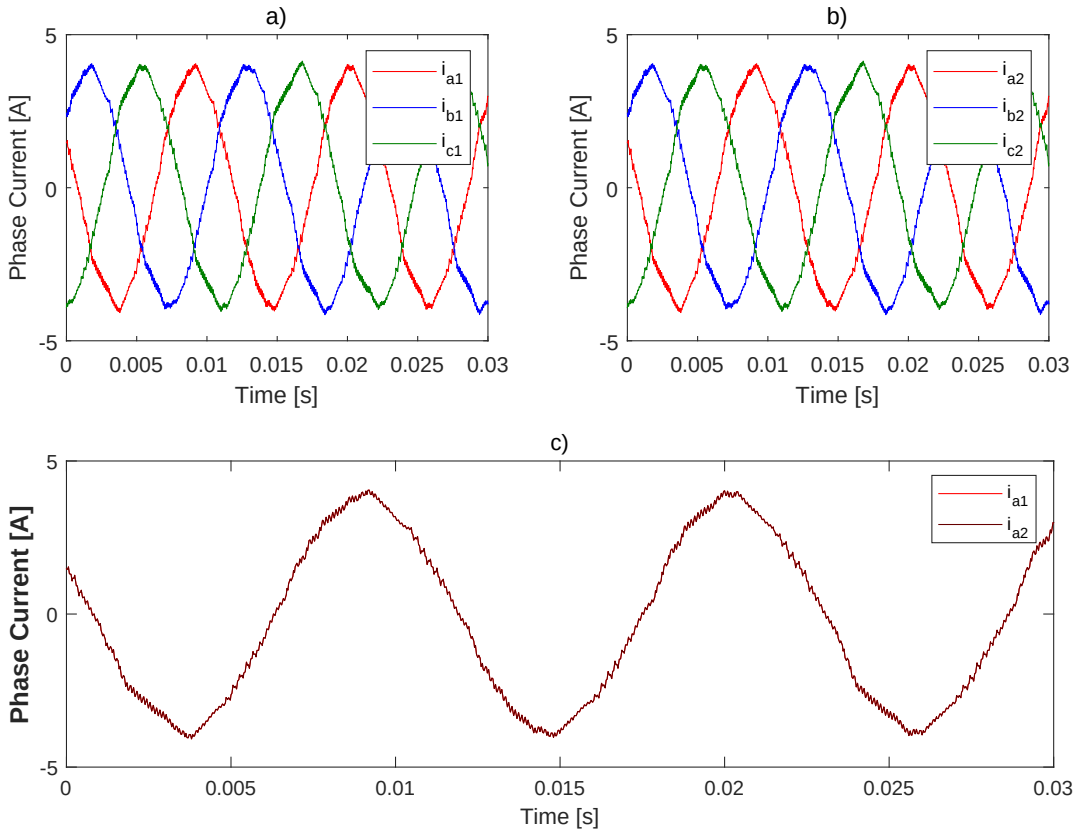

Figure 6.2: Simulated phase current for Synchronized SVM. a) winding set 1, b) winding set 2, c) i_{a1} and i_{a2}.

In figure 6.2 a) and b) all currents in both sets are plotted and it shows that all currents have same amplitude and the phases are 120° shifted for both sets. In

c), the i_{a1} and i_{a2} currents are plotted and are completely identical. This indicates that balanced currents in both winding sets are achievable when the SVM operates with synchronized pulses to the two inverters. Note that the simulation uses ideal inverters, so any unbalanced current sharing that could stem from the inverters will not be shown in the simulation.

6.1.2 SVM with interleaving

Figure 6.3 a) and b) shows the simulated CM voltage for SVM with interleaving. a) shows that the CM voltage has been reduced compared to synchronized SVM, with the CMV being a maximum of $\pm V_{dc}/6 = \pm 90$V. b) shows the zoomed plot of V_{cm}. The duration of the pulses changes at each instance, which indicates how the difference between the active times t_1 and t_2 changes constantly.
In figure 6.4 a) and b), all currents in both sets are plotted. Once again, it shows that all currents have same amplitude and the phases are 120° shifted for both sets. In c), the currents i_{a1} and i_{a2} are plotted and the interleaving method becomes visible as the current ripple is not in phase at all instances. Like the synchronized SVM, there is still no amplitude difference between the two currents which points to balanced currents in both winding sets when the SVM is operating with the interleaving scheme.

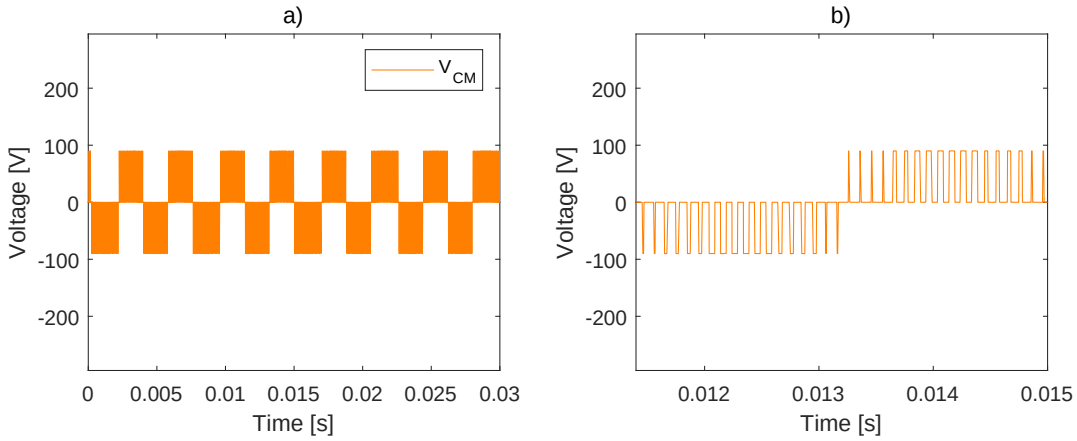

Figure 6.3: a) Simulated CM voltage with interleaved SVM operation b) With zoomed time axis.

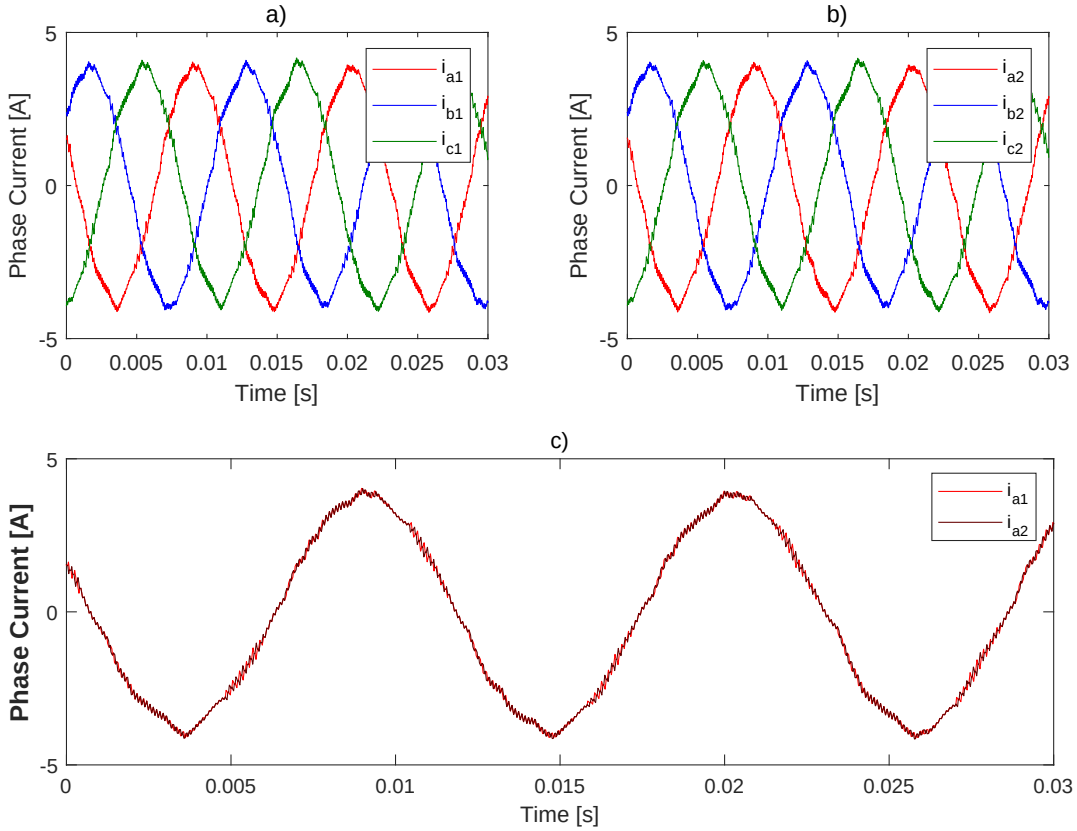

Figure 6.4: Simulated phase current for interleaved SVM. a) Winding set 1, b) Winding set 2, c) i_{a1} and i_{a2}.

6.1.3 ZCMV

Lastly, the implementation of the proposed ZCMV PWM strategy is presented. Figure 6.5 shows that the strategy can indeed eliminate the CM voltage, maintaining zero voltage throughout the entire period. However, the simulation is done without the implementation of dead time between gate signals. Therefore, the shift from a "0" to a "1" and vice versa happens instantaneously for the phase legs, enabling the criterion for zero CM voltage to be met with this PWM strategy.
Figure 6.6 (a) and (b) shows the phase currents for each set under steady conditions. The strategy delivers symmetrical three-phase sinusoidal currents to both winding sets. When comparing the i_{a1} and i_{a2} currents in (c) it can be observed that the current ripple is phase shifted. Furthermore, it can be observed that the two current signals are in phase, but not completely identical in amplitude. The peak is highest for i_{a1} in the positive half, while i_{a2} has the highest peak in the negative half. This suggests that a small offset exists between the two sets.

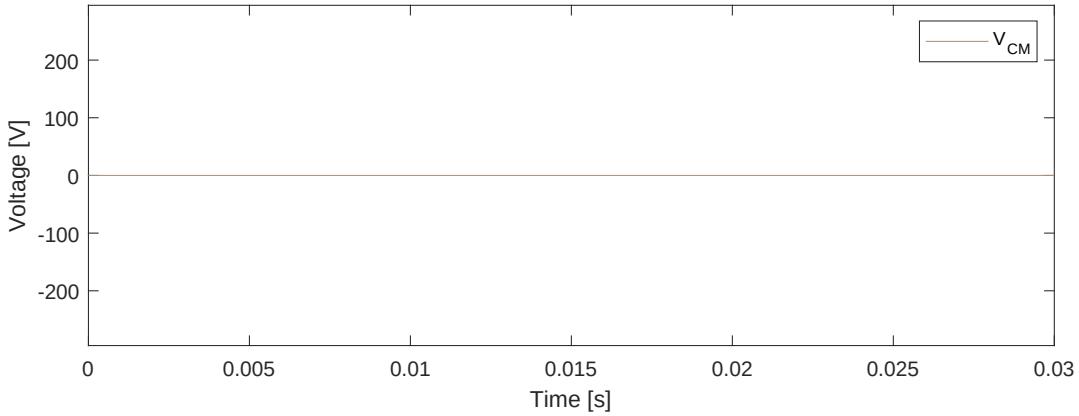

Figure 6.5: a) Simulated CM voltage with the ZCMV PWM strategy b) With zoomed time axis.

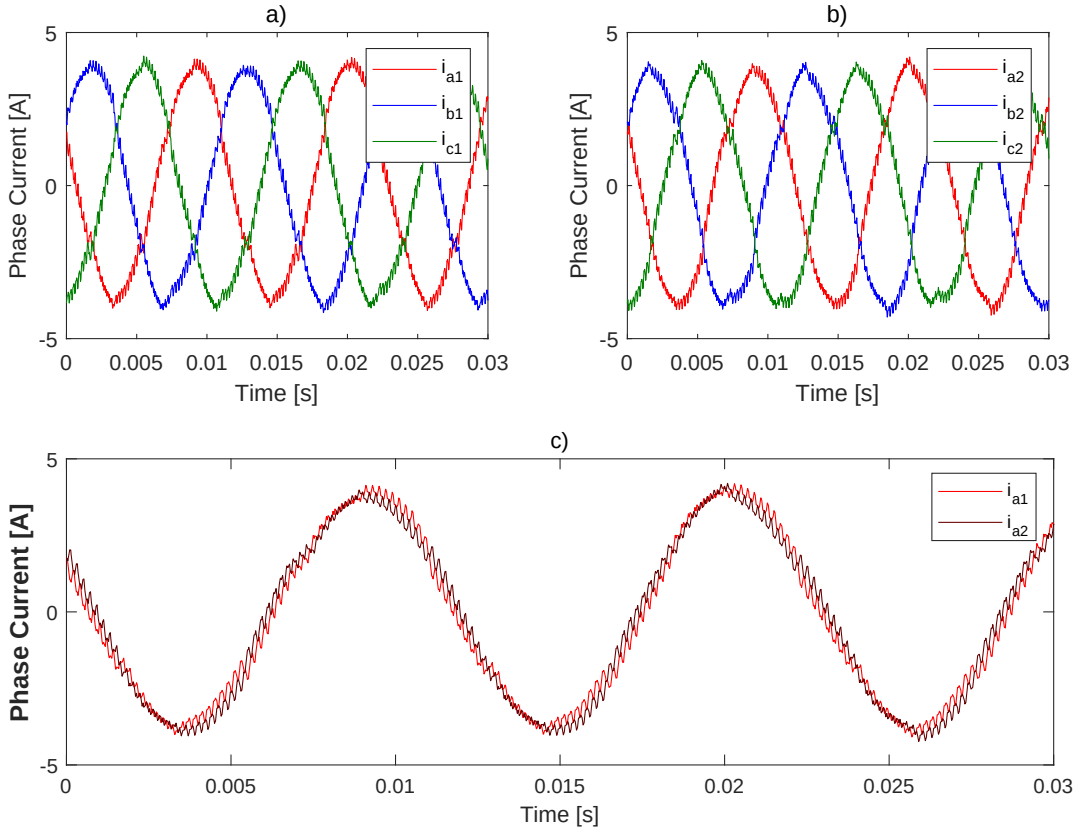

Figure 6.6: Simulated phase current for ZCMV scheme. a) winding set 1, b) winding set 2, c) i_{a1} and i_{a2}.

6.1.4 ZCMV with dead time

When operating a 2-level VSI, dead time is crucial for controlling the switches to prevent a short circuit condition. Dead time between the gate signals for each inverter leg is therefore implemented in the simulation model and the CM voltage is recorded. In total, 3 different dead times will be simulated to investigate the impact on the CMV:

- $2\mu s$
- $1\mu s$
- $0.5\mu s$

It is assumed that the transistor can change state significantly faster than the dead time for all simulations.

The simulation results show that the implementation of dead time have affected the CM voltage. The resulting voltage from the ZCMV algorithm have increased from non-existing to pulses of $\pm V_{dc}/6 = \pm 90$V, in all three dead time implementations as, seen from figure 6.7 (a), (c) and (e). In figure 6.7 (b), (d) and (f) a zoomed plot of a CM voltage pulse is shown. From the plot, it can be seen that the duration of the pulses equals the implemented dead time. The simulation results indicate that the performance of the ZCMV PWM strategy in reducing the CM voltage strongly depends on the dead time. The lower the dead time in the system, while still ensuring no shoot-through occurs, the shorter the total CM voltage pulses will be. However, the common mode voltage will not be completely eliminated in the case of dead time, suggesting that leakage and bearing current may still be present in the motor.

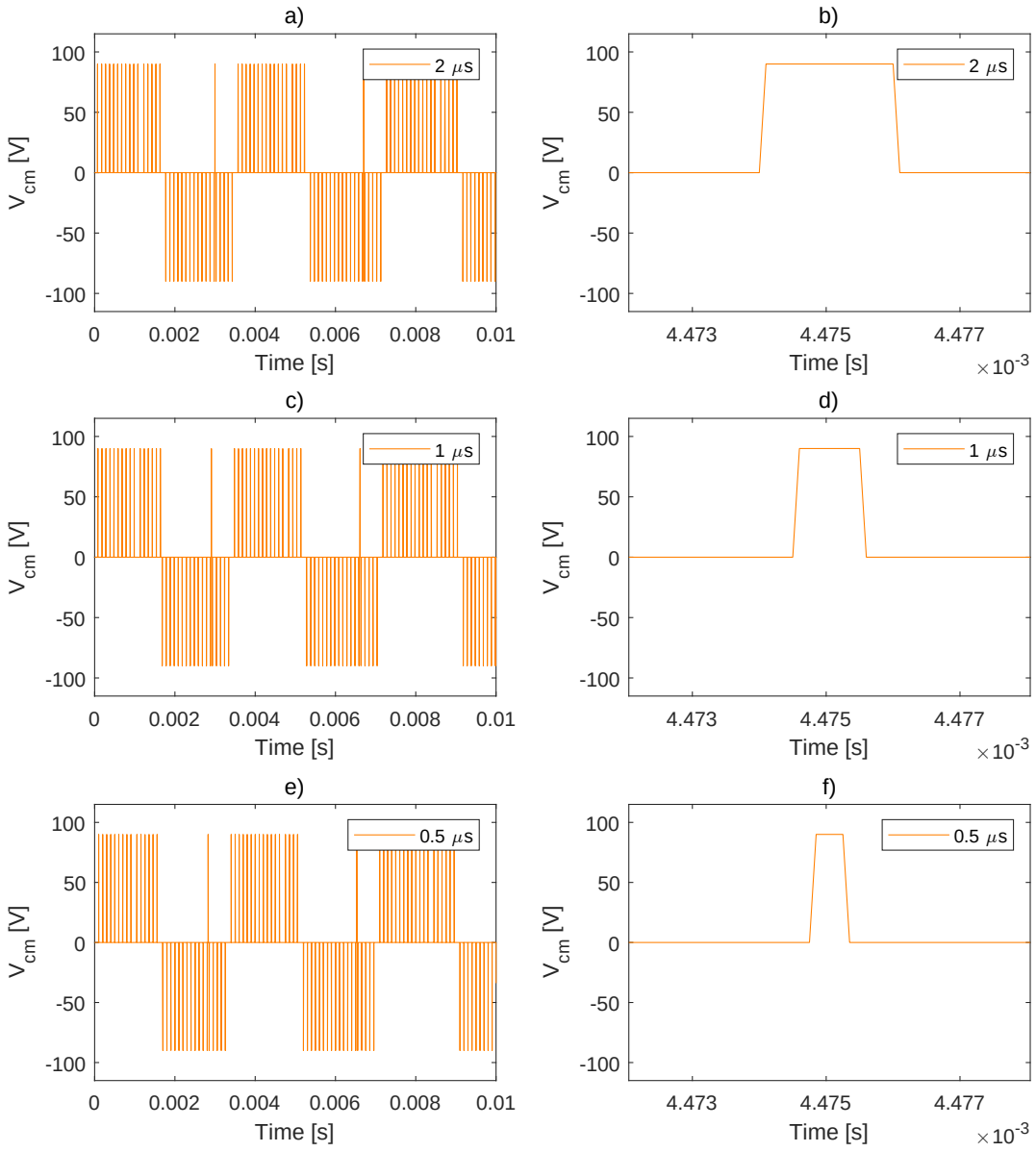

Figure 6.7: Simulated CM voltage with dead time. a), b) $2\mu s$. c), d) $1\mu s$. e), f) $0.5\mu s$

6.2 Leakage current

Recalling the CM circuit from figure 3.1 many capacitive couplings exitsted in the motor. These parasitic capacitances are unknown for the Grundfos motor which makes the unwanted inverter induced bearing currents difficult to simulate. However, investigating the characteristics of potential leakage current when operating under different PWM schemes remains relevant. Therefore, a new simulation

model is introduced. The simulation model is a simplified version of the HF CM circuit and is shown in figure 6.8. The model neglects the rotor side parasitic couplings and the grounding impedance and thereby only looks at the stator winding to frame CM loop. Furthermore HF pole voltages are replaced by the sub-CM voltage from each set V_{cm1} and V_{cm2}. The current running to ground is defined as the leakage current. In other words, the HF circuit on the rotor side are neglected and the assumption that if the leakage current formed from stator winding to frame is reduced, then the same case is true for corresponding current running in the bearings.

All sizes of the passive elements in the HF model for simulation are arbitrary values, which is strongly inspired by parasitic parameters values found in [8],[21]. The stray capacitor C_{sf} is 3 nF, $R_{sf} = 50\Omega$ and the Z_{cable} impedance consists of a resistive and inductive element with a value of 2.4Ω and 150μH.

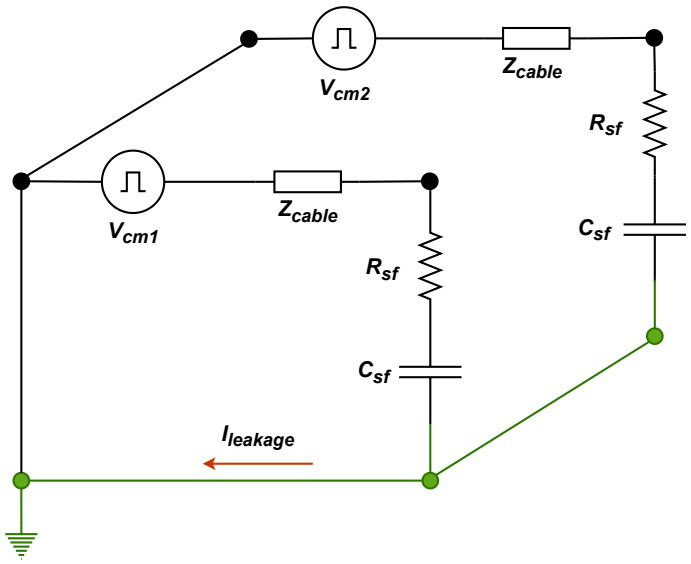

Figure 6.8: Simplified HF circuit.

The sub-CM voltage signals V_{cm1} and V_{cm2} are obtained from the steady state simulation, which was plotted in the above sections. Only one electrical period is simulated.

Figure 6.9 shows the simulation results of the leakage current for the three different PWM schemes. The highest leakage current is produced by the synchronized SVM operation with peak current exceeding 2 A. In comparison, the interleaving method have the leakage current peaking just over 1 A as a results of the reduced CM voltage. In the ideal case with no dead time, the ZCMV scheme can eliminate the leakage current as all rising and falling edges of the switching pattern are

aligned, meaning that the charge and discharge currents cancel out. The case of operating the ZCMV PWM scheme with different dead times was also tested and the results from it can be seen in figure 6.10. The results shows that the leakage current are present in all three cases but the current is decreasing with decreasing dead time.

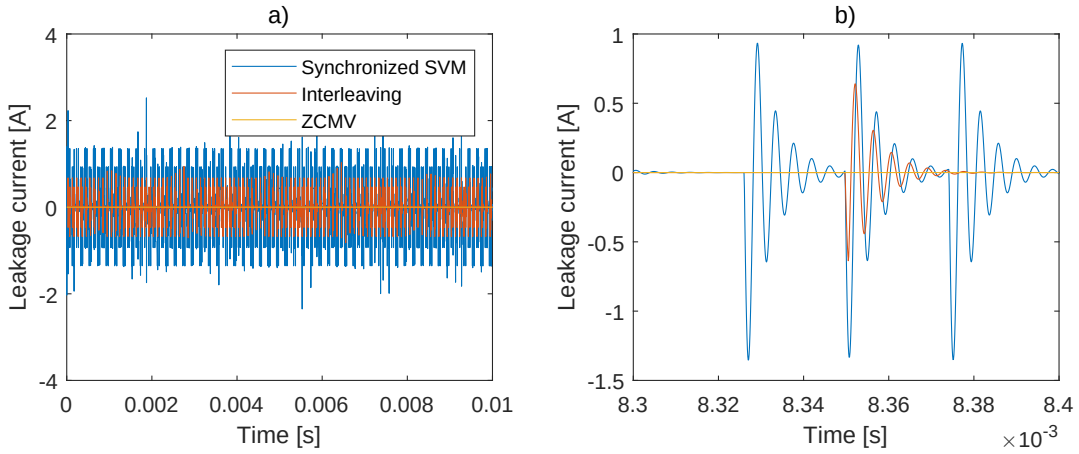

Figure 6.9: Simulated leakage current for the three PWM schemes.

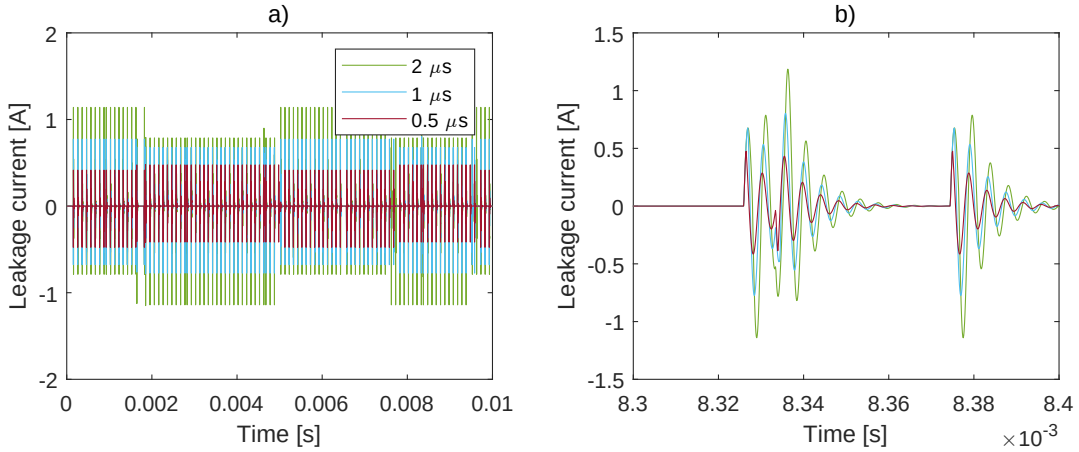

Figure 6.10: Simulated leakage current for the the ZCMV PWM scheme with three different dead times.

6.3 Experimental setup

The CM voltage and leakage current was measured on the test bench setup. The CM voltage measurement was performed by measuring voltages between the DC-link midpoint and the two separated neutral points on the motor, thereby extracting V_{cm1} and V_{cm2} created from each winding set. The total CM voltage can thereby be calculated from the two measurements.
The PWM scheme used is SVM operation with synchronized pulses. The DC-link voltage is 540V, switching frequency is 5 kHz and the motor is operating at 1800 rpm. The dead time for each inverter is $2\mu s$.

6.3.1 Common mode voltage measurement

From figure 6.11 (a) the measured neutral point voltages are displayed. The CM voltage from each set have six steps during one switching period and a total four different voltage levels are reached: $\pm V_{dc}/2$ and $\pm V_{dc}/6$ which confirms what was analyzed and simulated for SVM operation. However, it can also be viewed that the CM voltages signals are not aligned as expected, where a delay of $60\mu s$ exist between V_{cm1} and V_{cm2}. The signal for the total CM voltage is showed in (b) and it can be seen that the signal is stepping between $\pm V_{dc}/3 = \pm 180V$ and $\pm V_{dc}/6 = \pm 90V$ through a switching period.

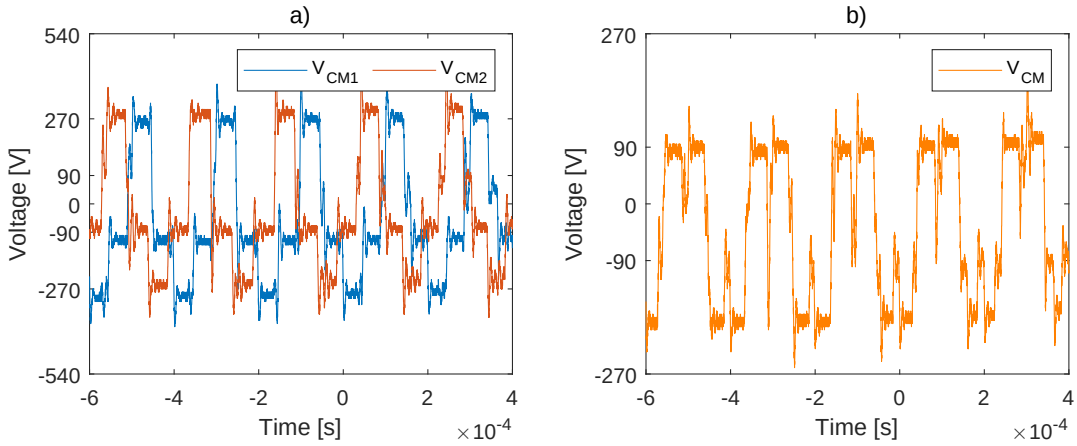

Figure 6.11: Measured CM voltage. a) Resulting CM voltage from each winding set, b) total CM voltage.

The delay between inverters was investigated on the setup. In order to do so, the duty cycle for each inverter was set to a constant of 0.5 and V_{aO1} and V_{aO2} was measured. As it can be seen on figure 6.12 the same delay exist between the phase voltages of each set. This suggest that the counter used for pulse generation in the two PWM block are not synchronized. As no solution on the software side were

found to synchronize the two PWM blocks, a new interface board is needed before the three PWM schemes can be tested. Due to time constraints it was not possible to design and implement a new control board before the deadline of the project.

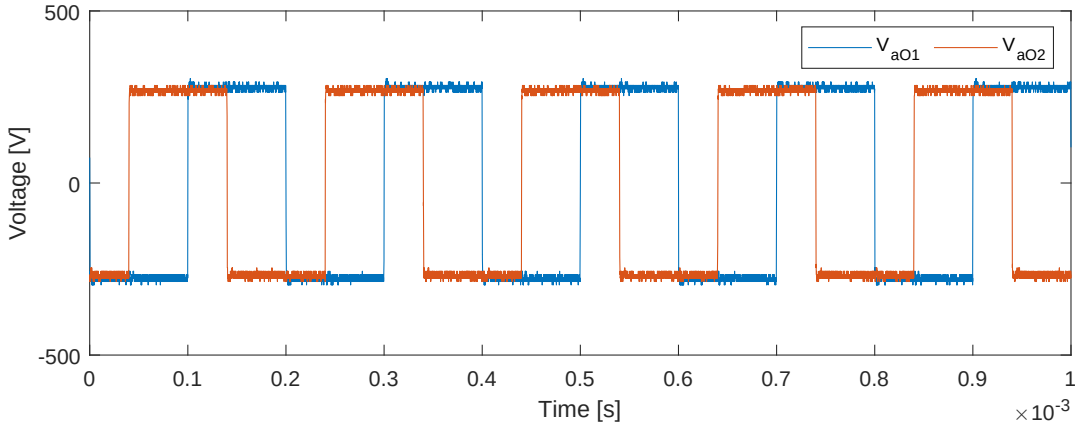

Figure 6.12: Measured voltages V_{a1O} and V_{a1O} when operating with a constant duty cycle of 0.5.

6.3.2 Leakage current measurement

The leakage current measurement was performed by connecting a current probe to the PE wire from the motor frame and the shields around the cable from the inverter. Since the PWM schemes could not be tested, the leakage current was observed only to understand its behavior and confirm its presence. From Figure 6.13 a), it can be seen that current is flowing through the PE, showing both positive and negative spikes with peak sizes exceeding $\pm$1A. In b), the plot is shown with a zoomed time axis. The current signal spikes, which results in oscillating behavior before it dampens back to 0 A.

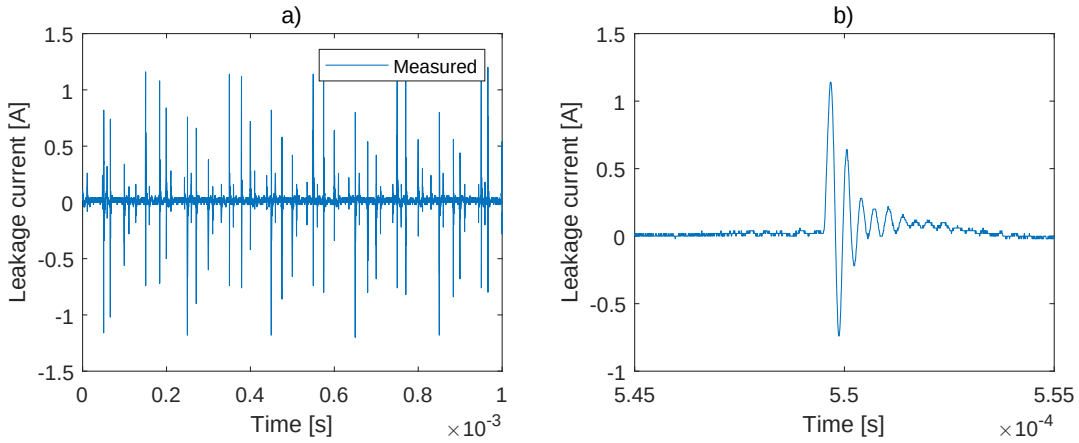

Figure 6.13: Measured leakage current.

The signal of the measured leakage current shows similar waveform tendencies, except in amplitude, as the simulated waveform. This indicates that the simplified HF simulation model, consisting of the sub-CM voltages and the RLC branches, can represent the behavior of the leakage current. However, further test with PWM schemes for CM voltage reduction must be made to see if the leakage current would have decreased before any validation of this simulation model can be made.

Chapter 7

Discussion

In this chapter, the project and the obtained results are discussed. The results are evaluated in light of the problem statement, and subsequently, the DTP is examined in terms of its advantages and disadvantages.
The determined parameters are acceptable as the results conformed with the simulations and only a single value raises a question: the leakage inductance. The leakage inductance constitute to 46% of the self-inductance. This amount of leakage inductance seems high and it may result in the prototype being less magnetically efficient when its operated as a DTP.
This type of problem might stem from the stator construction and winding arrangement. Recall that this prototype is two three-phase sets that are mirrored on opposite sides around the rotor profile. The information regarding such multi-phase machines are limited and it is difficult to find some leakage inductance values to compare the results to. In the multi-phase literature review [1] there is a comparison of different winding configurations and their corresponding angular displacements. It can be observed that the 0° angular displaced machine is the only winding configuration with the sets positioned on opposite sides of the rotor. Two other angular displacements are illustrated and their sets are mixed and positioned adjacent to each other around the stator. Unfortunately, there are no inductance values available with these different winding arrangements, which could otherwise leave a clue to whether or not the winding configuration is the root of the leakage inductance.
The transition from the standardized motor bench test setup to the dual-inverter DTP test bench brought many insights. The general idea was to rebuild and integrate the DTP machine into the existing setup. The primary reason to use the test bench is the simple and efficient software setup, which enables the user to deploy control algorithms directly from Simulink to the setup. Considering the project's scope, which involves parameter determination, FOC, and different PWM implementations within the constraints of a single semester, it appeared to be the right

solution with the best chances of success. In hindsight, this approach led to a series of problems and overlooked the importance of the general underlying idea: that every aspect of the setup needs to be identical. The system must have identical inverters, DC link and winding sets and this setup only provided the latter. Especially, in the context of the CM voltage reduction techniques, which relies on the phenomenon of canceling pulses by aligning opposite polarity pulses.
Therefore, using two identical inverters would be beneficial in relation to synchronisation of pulses but also in relation to current distribution. From the results in section 5.3 it was discovered that the two sets were not producing the same phase currents when executing the same duty-cycle using only a single DC link. Therefore, a second current control loop was implemented to have a balanced current distribution and to create FOC results. It is still unknown whether two identical inverters would yield equal current sharing. The literature suggest that unbalanced current sharing is common in DTP machines because small inherent asymmetries between the winding sets and the VSI's can cause uneven currents. A DTP machine performs with the best torque quality, stator MMF and efficiency if the currents are sinusoidal and equal in both sets [22]. Therefore, achieving equal and balanced current sharing is an important topic for future research on this machine.
In the investigation in regards to CM voltage, only simulation results was obtained. It showed that the proposed ZCMV PWM scheme under ideal conditions could completely remove the CM voltage and suppress the leakage current in the simplified HF model. When dead time was taken into account the scheme was producing a CM voltage with voltage pulses that had same duration as the dead time. With dead time implemented, the simulated leakage current was still reduced for the ZCMV scheme compared to the synchronized SVM scheme, but had similar current peaks to SVM with interleaving. The simulation model is still a much simplified version of the HF circuit, parameters did not fit actual motor and the validity of the results are questionable. However, a problem arises for the ZCMV scheme if unbalanced currents in each set exist. As mentioned, the test results extracted on the test bench showed that the motor had some problems with maintaining same current level. This only occurred when one current loop controller was used. When using two current loop controllers the two sets were balanced.

The potential consequence of a second current controller is that the two inverters are not modulating the same voltage reference. The ZCMV PWM strategy is highly dependent on having one voltage reference for both inverters to utilize its advantages in regards to CM voltage reduction. If different references was sent to the pulse generation of the ZCMV scheme, the immediate alignment of on and off switching would not be met, as the duty cycles for inverter 1 and 2 may not be the same.

Another drawback of the ZCMV is the limited modulation index compared to a conventional SVM. SVM enables a higher modulation index compared to the ZCMV PWM strategy, resulting in better utilization of the DC-link voltage. The asymmetrical gate pulses needed for ZCMV can also further complicate the practical implementation compared to SVM. In addition, once SVM is implemented, the adding of interleaving between inverters is simple in order to reduce CM voltage.

7.1 Future Work

The starting point of future work would be implementation of the PWM strategies in the laboratory. The test bench needs to be modified in two ways before this implementation is possible: two identical inverters and a new interface board. The importance of two identical inverters has been discussed throughout the thesis. Furthermore, it is still unknown if the prototype machine suffers from unbalanced current sharing before the inverters are identical and this should also be investigated thoroughly.
The interface board is a technical detail on the test setup. The AAU motor laboratory [20] uses a specially designed interface board between the Simulink/dSPACE setup and the inverters. The gate signals is generated by passing duty cycle values from Simulink to a dSPACE PWM block and then the interface board produces the gate signals for each inverter. Because the dSPACE PWM block only takes a duty cycle as an input, it is not possible to take control over the switch pattern, which is needed to implement the ZCMV strategy. By designing a new interface card, it might be possible to use a DAC to switch in a specific pattern and implement the ZCMV strategy.
If the ZCMV strategy could be implemented, it would open up the possibility of investigating the CM voltage and measuring whether the reduction that the simulation showed is present in the experimental setup. It would be interesting to implement the control with different dead times and observe if the effect is as pronounced as the simulation suggests.
The primary purpose of deploying a ZCMV strategy is to suppress the CM voltage, which in theory should reduce bearing currents as seen in the simulation. It would be interesting to measure the actual bearing current within the machine and it should be investigated if this is possible. Determining the parasitic capacitances and other parasitic impedances in the motor is also of interest to improve the precision of the simulation model of the HF CM circuit.
In relation to the DTP prototype in general a study into the leakage inductance and the mechanical construction could be are research topic. In the original project proposal from Grundfos, it was suggested that one of two main focuses could be chosen: control of the machine and CMV reduction techniques or motor design and dynamic simulation. With the findings of this thesis in mind, it would

be beneficial to launch an investigation in to the motor construction and leakage inductance. Maybe this investigation could undercover the impact is has on the machine performance when rewiring a conventional PMSM into a DTP.
In regards to the three PWM schemes the advantages and disadvantages regarding motor operation, such as Total Harmonic Distortion, torque ripple, and other factors, are also important to investigate. Since ZCMV is not well documented, future work could involve comparing the different PWM strategies while considering various motor operation criteria. ZCMV operation might introduce unwanted behavior in terms of THD of the current or could offer superior performance concerning torque ripple. All this is unknown, but plays an important role when it comes to reliability of the motor.

Chapter 8

Conclusion

This thesis aimed to explore the workings of a DTP machine and the potential benefits by using two inverters for the control. Grundfos provided a prototype of such machine, as they have an interest in using existing hardware to meet increasing power demands. This save the cost of designing and implementing new inverters for use in their pumps.
Initial literature study into the machine modelling, resulted in a DTP machine model that describes the inductances and the extra couplings that arises when using two sets of three-phase windings compared to a conventional PMSM. In addition, a Clark-Park reference transformation was detailed that enabled the *abc*-quantities of the machine to be transformed to *dq* domain. The inductance matrix in the *dq*-domain showed a clear magnetic interaction between the two sets, which does not occur in the conventional PMSM.
In order to characterise the DTP prototype the parameters of the machine had to be determined. The flux linkage from the permanent magnets and the inductances were simulated using FEA and measured on the machine. The chosen inductance measurement method was used to measure and calculate the self-inductance in the prototype and was modified to measure mutual inductances as well. The results of simulation and experimental measurements aligned and this validated the parameters values.
In addition, the inductances were also determined using the extended Clark-Park transformation. The results showed great resemblance to the calculated *dq* inductances and this verifies the extended Clark-Park transformation that was needed to employ FOC on the DTP machine.
A Simulink model was used to validate FOC on the DTP machine. The intention was to employ MTPA for IPMSM that utilises both the inherent magnetic and reluctance torque in the machine. When implementing the FOC on the experimental test setup, the MTPA was implemented for a SM-PMSM, which results in no utilization of the reluctance toque and therefore a less efficient control. The FOC was

validated under both steady state and dynamic conditions. The dynamic tests was a speed ramp and a load step and both the simulation and the experimental tests fulfilled the test criteria.
The use of two inverters opens the possibility to suppress CM voltage within the machine. An extensive study into CM voltage and PWM schemes to mitigate this phenomenon was detailed in the report. The SVM scheme with synchronized gate signals demonstrated the highest amplitude of CM voltage compared to the two other strategies. A simple yet effective way to reduce the CM voltage with SVM operation is interleaving the gate operation between the two inverters. Theory indicated that the CM voltage could be reduced to $V_{dc}/6$ which was validated through simulation. The last PWM scheme, ZCMV, showed promising results in the simulation, where it completely removed the CMV voltage in an ideal simulation. However when dead time was incorporated into the simulation model, results revealed that the CM voltage was dependent on dead time.
A simplified simulation model focusing on the stator winding to frame CM loop provided insights in leakage current behaviour. The simulation results indicated that synchronized SVM operation resulted in the highest leakage currents, while the interleaving method and ZCMV schemes reduced these currents. Measurements on the motor test bench showed expected CM voltage steps under SVM operation but revealed a delay between gate signals. Investigation showed unsynchronized pulse generation from the two inverters, though they were supposed to be synchronized. In order to solve this problem, a new control board is needed for the inverters and the time constraints prevented the implementation.
Due to synchronization issues between the software PWM blocks and time constraints, the experimental verification of all PWM schemes was incomplete. In conclusion, further experimental validation is needed to confirm CM voltage simulation results.

Bibliography

[1] Ziqiang Zhu et al. "Advances in Dual-Three-Phase Permanent Magnet Synchronous Machines and Control Techniques". In: *Energies* 14.22 (2021). ISSN: 1996-1073. DOI: 10.3390/en14227508. URL: https://www.mdpi.com/1996-1073/14/22/7508.

[2] J. Karttunen et al. "Dual three-phase permanent magnet synchronous machine supplied by two independent voltage source inverters". In: (2012), pp. 741–747. DOI: 10.1109/SPEEDAM.2012.6264448.

[3] M. Andriollo et al. "Analysis of Double Star Permanent Magnet Synchronous Generators by a General Decoupled d-q Model". In: *2007 IEEE International Electric Machines Drives Conference*. Vol. 1. 2007, pp. 7–12. DOI: 10.1109/IEMDC.2007.383544.

[4] Samuli Kallio et al. "Decoupled d-q Model of Double-Star Interior-Permanent-Magnet Synchronous Machines". In: *Industrial Electronics, IEEE Transactions on* 60 (June 2013), pp. 2486–2494. DOI: 10.1109/TIE.2012.2216241.

[5] Akira Satake, Yuriko Okamoto, and Satoru Kato. "Design of Coupling Cancellation Control for a Double-winding PMSM". In: *IEEJ Journal of Industry Applications* 6.1 (2017), pp. 29–35. DOI: 10.1541/ieejjia.6.29.

[6] Kaiyuan Lu, Peter Rasmussen, and Ewen Ritchie. "Investigation of Flux-Linkage Profile Measurement Methods for Switched-Reluctance Motors and Permanent-Magnet Motors". In: *Instrumentation and Measurement, IEEE Transactions on* 58 (Oct. 2009), pp. 3191 –3198. DOI: 10.1109/TIM.2009.2017154.

[7] Jun-Kyu Park, Se-Hyun Rhyu, and Jin Hur. "Shaft-to-frame voltage mitigation method by changing winding-to-rotor parasitic capacitance of IPMSM". In: *2017 IEEE Energy Conversion Congress and Exposition (ECCE)*. 2017, pp. 3571–3576. DOI: 10.1109/ECCE.2017.8096635.

[8] Abraham Marquez Alcaide et al. "Common-Mode Voltage Mitigation of Dual Three-Phase Voltage Source Inverters in a Motor Drive Application". In: *IEEE Access* 9 (2021), pp. 67477–67487. DOI: 10.1109/ACCESS.2021.3072967.

[9] Yafei Ma et al. “Common-Mode Voltage Elimination of Dual Three-Phase Motor with Different Angular Displacements”. In: *IEEE Transactions on Industrial Electronics* 71.6 (2024), pp. 5431–5442. DOI: 10.1109/TIE.2023.3292863.

[10] Dong Jiang, Zewei Shen, and Fei Wang. “Common-Mode Voltage Reduction for Paralleled Inverters”. In: *IEEE Transactions on Power Electronics* 33.5 (2018), pp. 3961–3974. DOI: 10.1109/TPEL.2017.2712369.

[11] Zewei Shen et al. “Dual-Segment Three-Phase PMSM With Dual Inverters for Leakage Current and Common-Mode EMI Reduction”. In: *IEEE Transactions on Power Electronics* 34.6 (2019), pp. 5606–5619. DOI: 10.1109/TPEL.2018.2866338.

[12] Sang-Hoon Kim. “Chapter 7 - Pulse width modulation inverters”. In: *Electric Motor Control*. Ed. by Sang-Hoon Kim. Elsevier, 2017, pp. 265–340. ISBN: 978-0-12-812138-2. DOI: https://doi.org/10.1016/B978-0-12-812138-2.00007-6. URL: https://www.sciencedirect.com/science/article/pii/B9780128121382000076.

[13] Sang-Hoon Kim. “Chapter 5 - Vector control of alternating current motors”. eng. In: *Electric Motor Control*. Elsevier Inc, 2017, pp. 203–246. ISBN: 0128121386.

[14] *ANALYSIS OF ELECTRIC MACHINERY AND DRIVE SYSTEMS. Third Edition*. IEEE, 2013. ISBN: 978-1-118-02429-4.

[15] A. von Jauanne and Haoran Zhang. “A dual-bridge inverter approach to eliminating common-mode voltages and bearing and leakage currents”. In: *IEEE Transactions on Power Electronics* 14.1 (1999), pp. 43–48. DOI: 10.1109/63.737591.

[16] Annette Muetze and Andreas Binder. “Techniques for Measurement of Parameters Related to Inverter-Induced Bearing Currents”. In: *IEEE Transactions on Industry Applications* 43.5 (2007), pp. 1274–1283. DOI: 10.1109/TIA.2007.904413.

[17] Zewei Shen et al. “Common-Mode Voltage Elimination for Dual Two-Level Inverter-Fed Asymmetrical Six-Phase PMSM”. In: *IEEE Transactions on Power Electronics* 35.4 (2020), pp. 3828–3840. DOI: 10.1109/TPEL.2019.2933446.

[18] Grundfos. *Grundfos Product Selection*. https://product-selection.grundfos.com/uk/products/mge-mle/mge100la-98971049?pumpsystemid=2301068326&tab=variant-specifications. Accessed on April 2, 2024.

[19] Wissing, M. B., Ferm, V., Eikenes, B. *PMSM Sensorless Control Using Higher Order Sliding Mode Observer. Aalborg Universitet (2023)*. https://kbdk-aub.primo.exlibrisgroup.com/permalink/45KBDK_AUB/a7me0f/alma9921565412305762. 15-5-2024.

[20] AAU Energy. *DRIVES CONTROL LABORATORY*. https://www.energy.aau.dk/laboratories/drives-control-laboratory. Seen: 20-03-2024. 2024.

[21] Oliver Magdun and Andreas Binder. "High-Frequency Induction Machine Modeling for Common Mode Current and Bearing Voltage Calculation". In: *IEEE Transactions on Industry Applications* 50.3 (2014), pp. 1780–1790. DOI: 10.1109/TIA.2013.2284301.

[22] Jussi Karttunen et al. "Decoupled Vector Control Scheme for Dual Three-Phase Permanent Magnet Synchronous Machines". In: *IEEE Transactions on Industrial Electronics* 61.5 (2014), pp. 2185–2196. DOI: 10.1109/TIE.2013.2270219.

[23] MathWorks. *Permanent magnet synchronous motor with sinusoidal flux distribution*. https://se.mathworks.com/help/sps/ref/pmsm.html. Seen: 4-2-2024. 2024.

Appendix A

Motor Parameters Measurements

A.1 Resistance

The resistance is measured at an ambient temperature at approximately 22°C and without heating up the motor by running it.

	Resistance
a1	2.4 Ω
b1	2.4 Ω
c1	2.5 Ω
a2	2.4 Ω
b2	2.45 Ω
c2	2.5 Ω

Table A.1: Resistance measurement pr. phase and average value.

The average value of the phase resistance is $R_s = 2.44\Omega$.

A.2 Back EMF test

The flux-linkage constant is calculated using the back EMF constant, which is given by the following equation [23]:

$$e_{ph} = k_e \omega_m \tag{A.1}$$

where e_{ph} is the peak voltage induced in the windings by rotating the DTP and recording the generated terminal voltage, at the mechanical speed ω_m which yields the back EMF constant k_e. The flux linkage of the permanent magnets is then found by the relation between the constant and the number of pole pairs N_{pp} is the machine:

$$\lambda_{PM} = \frac{k_e}{N_{pp}} \tag{A.2}$$

	$ACRMS$	rpm	V_{peak}	ω_m	k_e	λ_{PM}
c2	30.25	500.00	42.78	52.36	0.82	0.272
b2	30.30	500.00	42.85	52.36	0.82	0.273
a2	30.40	500.00	42.99	52.36	0.82	0.274
c2	91.20	1500.00	128.98	157.08	0.82	0.274
b2	91.50	1500.00	129.40	157.08	0.82	0.275
a2	91.70	1500.00	129.68	157.08	0.83	0.275
c2	176.00	2900.00	248.90	303.69	0.82	0.273
b2	176.50	2900.00	249.61	303.69	0.82	0.274
a2	177.00	2900.00	250.32	303.69	0.82	0.275
a1	30.30	500.00	42.85	52.36	0.82	0.273
b1	30.35	500.00	42.92	52.36	0.82	0.273
c1	30.35	500.00	42.92	52.36	0.82	0.273
a1	91.40	1500.00	129.26	157.08	0.82	0.274
b1	91.60	1500.00	129.54	157.08	0.82	0.275
c1	91.50	1500.00	129.40	157.08	0.82	0.275
a1	176.40	2900.00	249.47	303.69	0.82	0.274
b1	176.90	2900.00	250.17	303.69	0.82	0.275
c1	176.70	2900.00	249.89	303.69	0.82	0.274

Table A.2: Back EMF measurement pr. phase at speeds: 500, 1500 and 2900 rpm. Calculated average flux linkage from permanent magnets λ_{PM}.

The average value of the flux linkage from the PM is: $\lambda_{PM} = 0.274$Wb.

A.3 Inductance

A.3.1 Flux-linkage vs. Current Curve Calculation

A single phase is exited by an AC voltage u_{in} at $f = 50Hz$, which leads to the following equivalent diagram presented i figureA.1.

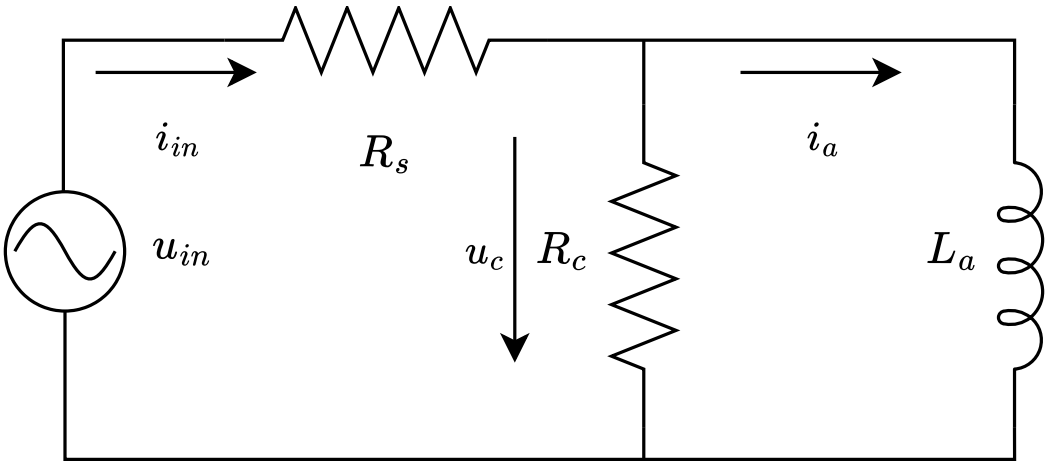

Figure A.1: Equivalent circuit for measurements at steady state with ac excitation (Diagram from [6]).

First, the core loss resistance is calculated by the input power and phase resistance R. The average input power is calculated by integrating the product of the voltage and current of a fundamental period and divide it by the period $T = \frac{1}{f}$:

$$P_{in} = \frac{1}{T} \int_{-T/2}^{T/2} u_{in}(t) i_{in}(t)\, dt \tag{A.3}$$

then the average power of the core loss is calculated

$$P_c = P_{in} - R_s \left(\frac{i_{in,peak}}{\sqrt{2}} \right)^2 \tag{A.4}$$

To get the voltage across the parallel RL brach the voltage drop across the phase resistance must be deducted

$$u_c(t) = u_{in}(t) - R_s i_{in}(t) \tag{A.5}$$

The core resistance is calculated

$$R_c = \frac{\left(\frac{u_{c,peak}}{\sqrt{2}}\right)^2}{P_c} \tag{A.6}$$

The current through the inductor is calculated

$$i_a(t) = i_{in}(t) - \frac{u_c(t)}{R_c} \tag{A.7}$$

The flux produced by the inductor over the fundamental period is calculated by integrating the voltage across it

$$\lambda_{total} = \int_{-T/2}^{T/2} u_c(t)\, dt \tag{A.8}$$

The DC component, which corresponds to the flux linkage that is produced by the permanent magnets, is removed from the total flux by deducting the average value of the flux-linkage:

$$\lambda_{avg} = \frac{\lambda_{total}}{T} \tag{A.9}$$

The flux-linkage generated by the inductance and the AC voltage is calculated:

$$\lambda_L = \lambda_{total} - \lambda_{avg} \tag{A.10}$$

The flux-linkage and current loop can then be plotted as seen in figure A.2.

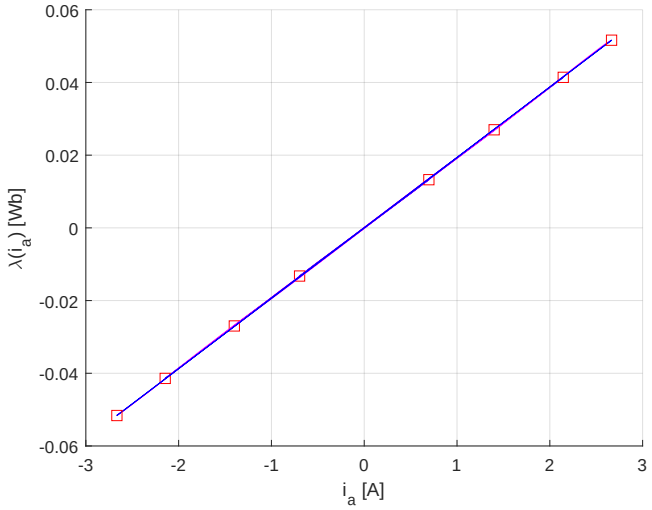

Figure A.2: Flux-linkage current curve.

The vertices of this loop is the minimum and maximum flux linkage. Performing linear regression and extracting the slope of the line yields the value of the inductance:

$$L = \frac{d\lambda_L}{di_a} \tag{A.11}$$

Performing all the above at multiple rotor positions yields all the inductances and the plot is seen in figure A.3.

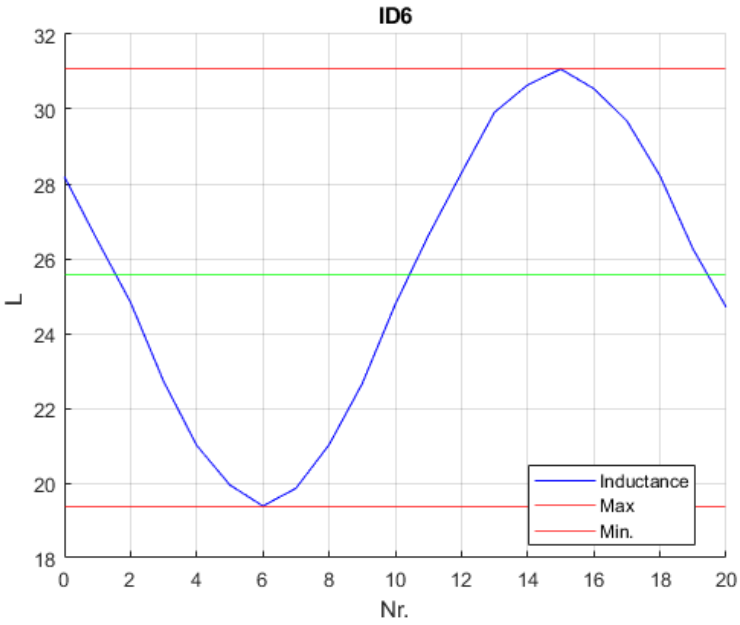

Figure A.3: Inductance versus position. Top red line is maximum value, bottom is minimum and the green is the average. Y-axis is inductance $[mH]$ and x-axis is rotor position in Nr. of measurements.

As seen on the figure, the x-axis is the number of inductance calculation, meaning there has been performed 20 inductance calculations at 20 different positions. The electrical position is unknown since the encoder malfunctioned. This has no effect on the measurements because only the min-, max- and average values are needed from this data to characterise the inductance over an electrical period.

A.3.2 Inductance Measurements

All inductance measurements is presented in figure A.4:

ID	3		4		5		6		7		8		
Inductance	min	max	min	max	min	max	min	max	min	max	min	max	Avg.
a1a1	19.4	31.16	19.4	31.17			19.38	31.07					25.26333
a1b1	-8.11	-3.52											-5.815
a1a2							0.68	2.56					1.62
a1b2					-2.92	-2.17							-2.545
a1c2							-3.12	-0.5					-1.81
c1c1									20.26	31.95	20.26	31.97	26.11
c1b1									-8.12	-3.51			-5.815
c1b2									-3.07	-2.21			-2.64
c1a1											-7.82	-5.1	-6.46
c1a2											-3.22	-0.52	-1.87

Figure A.4: Inductance Measurements.

Averaging the four different inductances:

		Measurements				Average	Min.	Max.
Single Set	Self	25.26333	26.11			25.69	19.74	31.46
	Mutual	-5.815	-5.815	-6.46		-6.03	-8.02	-4.04
Set-to-Set	Set2set Self	1.62				1.62	0.68	2.56
	Set2set Mutal	-2.545	-1.81	-2.64	-1.87	-2.22	-3.08	-1.35

Figure A.5: Average Inductance Measurements.

From the row 'Single Set Self' the average phase self-inductance is noted as:

$$L_s = L_{aa} = L_{bb} = L_{cc} = 25.69mH \tag{A.12}$$

The leakage inductance can be expressed as the difference between self-inductance and mutual inductance in a single set of windings. From the relation between self-inductance and average magnetization inductance the leakage inductance can be determined [14]:

$$L_s = L_{ls} + L_A \tag{A.13}$$

Where L_A is the average magnetizing inductance and L_{ls} is the leakage inductance. This equation described how a part of the flux is not linking with its own windings, resulting in a leakage flux that links elsewhere fx. the stator iron. The average mutual-inductance in a single set can be described by this magnetizing inductance:

$$L_{ab} = L_{bc} = L_{ca} = -\frac{1}{2}L_A \leftrightarrow L_A = L_{ab}(-2) \tag{A.14}$$

$$\tag{A.15}$$

And the leakage inductance is therefore determined:

$$L_{ls} = L_a - L_A \leftrightarrow L_{ls} = L_a - L_{ab}(-2) \tag{A.16}$$

Using the average self inductance and mutual values (marked by red on figure A.5 the leakage is calculated:

$$L_{ls} = 25.69 - ((-6.03)(-2)) \tag{A.17}$$

$$L_{ls} = 13.63mH \tag{A.18}$$

With the leakage inductance is known, the average magnetization value L_A and second harmonic amplitude L_B for a single set, as well as set to set, be determined. The results are displayed in table A.3:

	Single Set		Set to Set	
	L_A	L_B	M_A	M_B
Self	12.06	5.86	1.62	0.94
Mutual	12.06	1.99	4.4325	0.87
Avg.	12.06	3.92	3.02625	0.90

Table A.3: Average DC and 2nd Harmonic Inductance values from measurements.

Using the results displayed in the table and leakage inductance, the *dq* inductances can be calculated using equation 2.23:

Parameter	**Value**
L_d	25.83 mH
L_q	37.60 mH
M_d	3.18 mH
M_q	5.89 mH

Table A.4: Average values of measured *dq* inductances.

Appendix B

Motor Parameters Simulation

B.1 BEMF Calculation

Induced phase voltages recorded at zero current, corresponding to spinning the motor without supplying the stator.

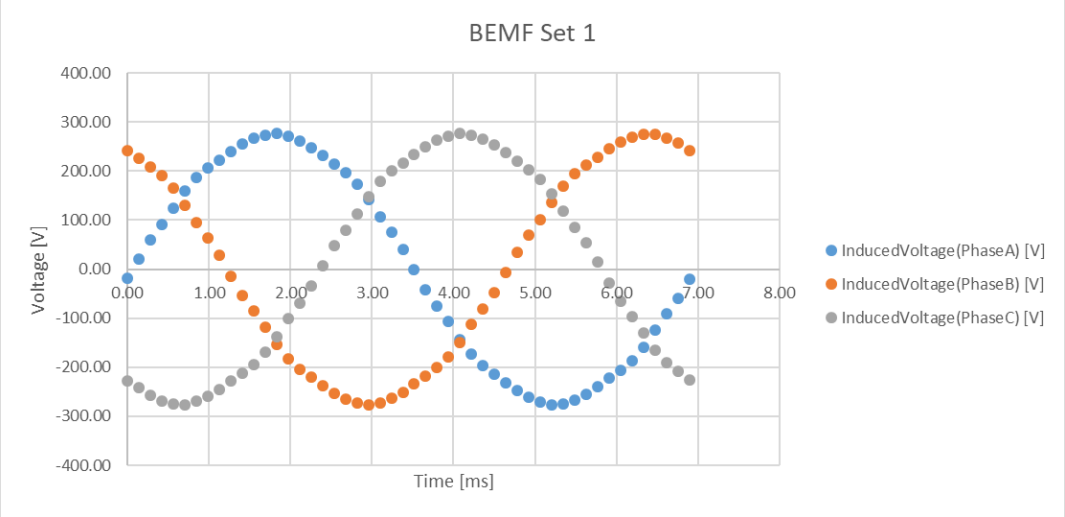

Figure B.1: Induced phase voltages set 1.

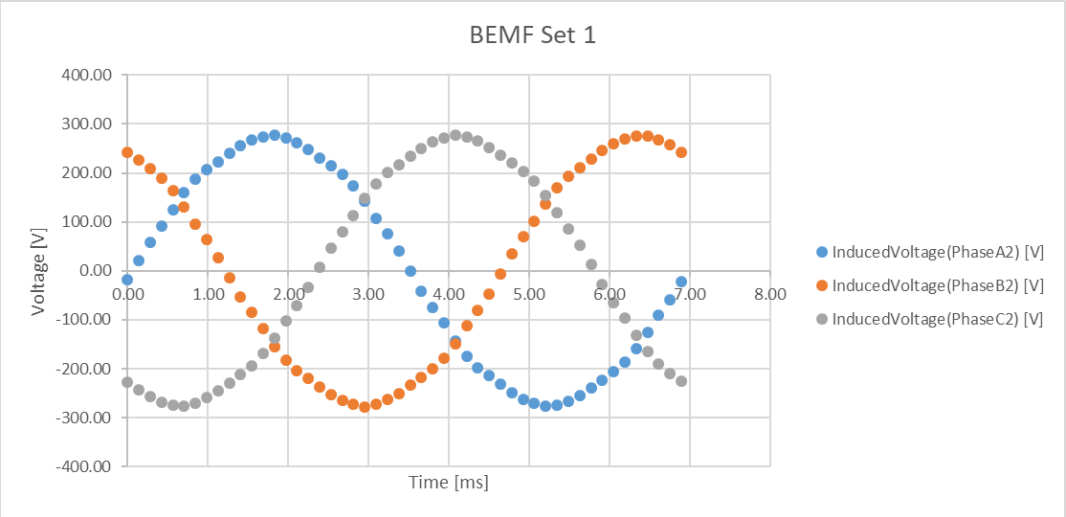

Figure B.2: Induced phase voltages set 2.

The min- and max peak voltage values are calculated:

	A1	B1	C1	A2	B2	C2
min	-276.80	-277.44	-276.84	-276.80	-277.44	-276.84
max	277.40	276.00	277.22	277.40	275.99	277.22
peak	277.10	276.72	277.03	277.10	276.71	277.03

Table B.1: Min- and max. values of peak induced voltage pr. phase.

The flux-linkage is calculated at the rated speed as described in A:

k_e	λ_{PM}
0.912447	0.304149
0.9112	0.303733
0.912218	0.304073
0.912451	0.30415
0.911181	0.303727
0.912211	0.30407
Average	0.303984

Table B.2: Flux-linkage constant from PM calculated from simulation.

The average flux-linkage from the PM is $\lambda_{PM} = 0.3$ Wb.

Appendix C

dq to DQ

A further transformation is suggested in [4] to eliminate the coupling terms between dq_1 and dq_2 reference frames that exist due to the mutual inductances derived in L_{T1}. The transformation matrix from dq to the final DQ reference matrix is obtained:

$$T_2 = k \begin{bmatrix} 1 & 0 & 1 & 0 \\ 0 & 1 & 0 & 1 \\ 0 & 1 & 0 & -1 \\ -1 & 0 & 1 & 0 \end{bmatrix} \tag{C.1}$$

There the coefficient $k = \frac{1}{2}$ to enable the amplitude to be invariant. Combining the Clarke-Park transformation matrix $T_1(\theta)$ and C.1 the full *abc*-DQ transformation matrix can be found:

$$T_{DQ} = \frac{1}{2} \begin{bmatrix} T(\theta) & T(\theta) \\ T(\theta + \frac{\pi}{2}) & T(\theta - \frac{\pi}{2}) \end{bmatrix} \tag{C.2}$$

The new inductance matrix can be calculated:

$$L_{DQ} = T_{DQ}(\theta) L_{dq} T_{DQ}(\theta)^{-1} \tag{C.3}$$

Note that the only inductances are on the diagonal of the matrix.

$$L_{DQ} = \begin{bmatrix} L_{D1} & 0 & 0 & 0 \\ 0 & L_{Q1} & 0 & 0 \\ 0 & 0 & L_{D2} & 0 \\ 0 & 0 & 0 & L_{Q2} \end{bmatrix} \tag{C.4}$$

From C.4 there are no mutual coupling between DQ_1 and DQ_2. The inductances in the DQ reference frame can be defined as:

$$\begin{cases} L_{D1} = L_d + M_d \\ L_{Q1} = L_q + M_q \\ L_{D2} = L_q - M_q \\ L_{Q2} = L_d - M_d \end{cases} \tag{C.5}$$

The transformation matrix from C.2 can be used to transform all electrical parameters in the machine model into the DQ reference frame. The voltage eqautions when applying $T_{DQ}(\theta)$ are as followed:

$$\begin{bmatrix} u_{D1} \\ u_{Q1} \\ u_{D2} \\ u_{Q2} \end{bmatrix} = \begin{bmatrix} R_s & 0 & 0 & 0 \\ 0 & R_s & 0 & 0 \\ 0 & 0 & R_s & 0 \\ 0 & 0 & 0 & R_s \end{bmatrix} \begin{bmatrix} i_{D1} \\ i_{Q1} \\ i_{D2} \\ i_{Q2} \end{bmatrix} + p \begin{bmatrix} \lambda_{D1} \\ \lambda_{Q1} \\ \lambda_{D2} \\ \lambda_{Q2} \end{bmatrix} + \omega_e \begin{bmatrix} -\lambda_{Q1} \\ \lambda_{D1} \\ -\lambda_{Q2} \\ \lambda_{D2} \end{bmatrix} \tag{C.6}$$

$$\begin{cases} u_{D1} = R_s i_{D1} + \frac{di_{D1}}{dt} L_{D1} - \omega_e L_{Q1} i_{Q1} \\ u_{Q1} = R_s i_{Q1} + \frac{di_{Q1}}{dt} L_{Q1} + \omega_e (L_{D1} i_{D1} + \lambda_{pm}) \\ u_{D2} = R_s i_{D2} + \frac{di_{D2}}{dt} L_{D2} - \omega_e L_{Q2} i_{Q2} \\ u_{Q2} = R_s i_{Q2} + \frac{di_{Q2}}{dt} L_{Q2} + \omega_e (L_{D2} i_{D2}) \end{cases} \tag{C.7}$$

C.0.1 Torque equation

From equation C.1 the current in DQ reference frame can be defined as:

$$\begin{cases} i_{D1} = \frac{(i_{d1} + i_{d2})}{2} \\ i_{Q1} = \frac{(i_{q1} + i_{q2})}{2} \\ i_{D2} = \frac{(i_{q1} - i_{q2})}{2} \\ i_{D2} = \frac{(i_{d2} - i_{d1})}{2} \end{cases} \tag{C.8}$$

The flux linkage will be:

$$\begin{bmatrix} \lambda_{D1} \\ \lambda_{Q1} \\ \lambda_{D2} \\ \lambda_{Q2} \end{bmatrix} = \begin{bmatrix} L_{D1} & 0 & 0 & 0 \\ 0 & L_{Q1} & 0 & 0 \\ 0 & 0 & L_{D2} & 0 \\ 0 & 0 & 0 & L_{Q2} \end{bmatrix} \begin{bmatrix} i_{D1} \\ i_{Q1} \\ i_{D2} \\ i_{Q2} \end{bmatrix} + \begin{bmatrix} \lambda_{pm} \\ 0 \\ 0 \\ 0 \end{bmatrix} \tag{C.9}$$

Combining the new expression for the current and the flux linkage with the torque equation for the PMSM:

$$T_e = \frac{3}{2} N_{pp} (2\lambda_{mpm} i_{Q1} + 2(L_{D1} - L_{Q1}) i_{D1} i_{Q1} + 2(L_{D2} - L_{Q2}) i_{D2} i_{Q2}) \tag{C.10}$$

Assuming $L_{D2} = L_{Q2}$ the torque equation ends up looking like:

$$T_e = 3N_{pp}(\lambda_{mpm} i_{Q1} + (L_{D1} - L_{Q1}) i_{D1} i_{Q1}) \tag{C.11}$$

Appendix D

Comparator for ZCMV PWM Strategy

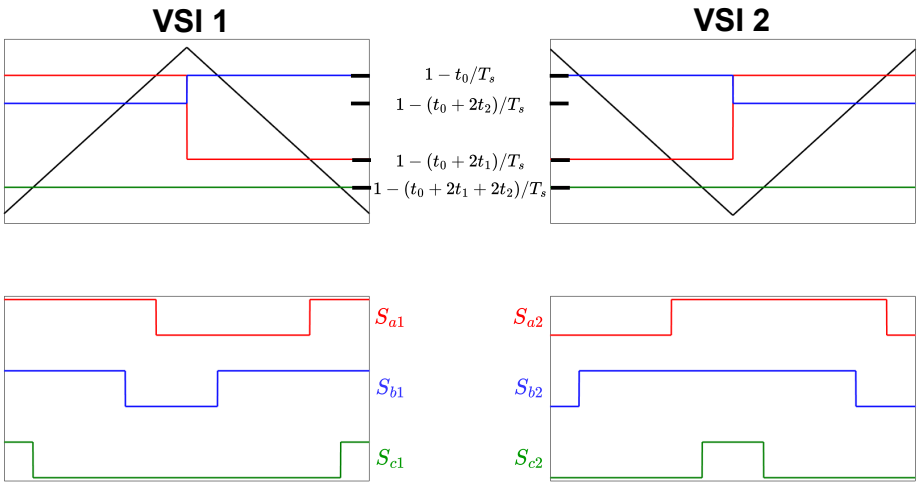

Figure D.1: Sector 2.

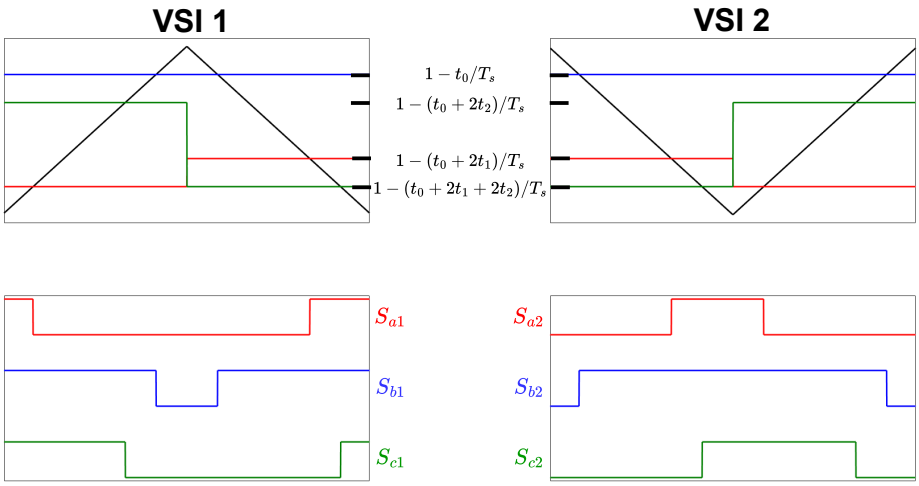

Figure D.2: Sector 3.

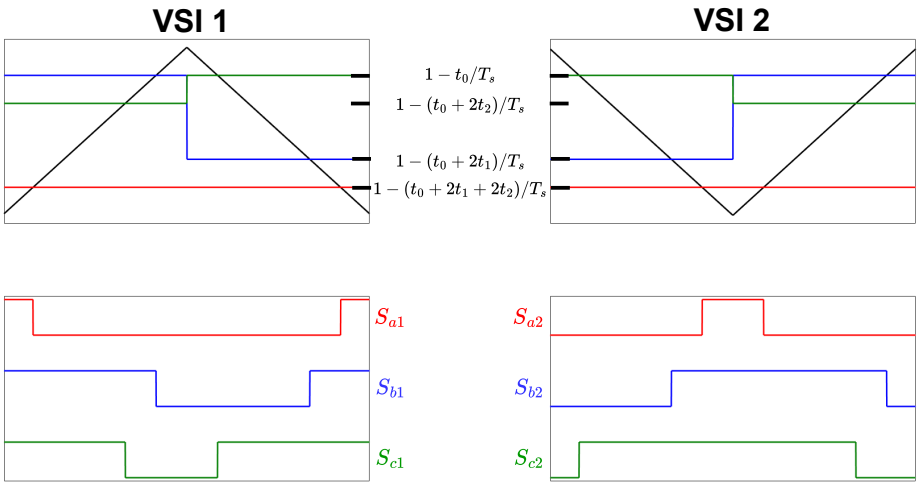

Figure D.3: Sector 4.

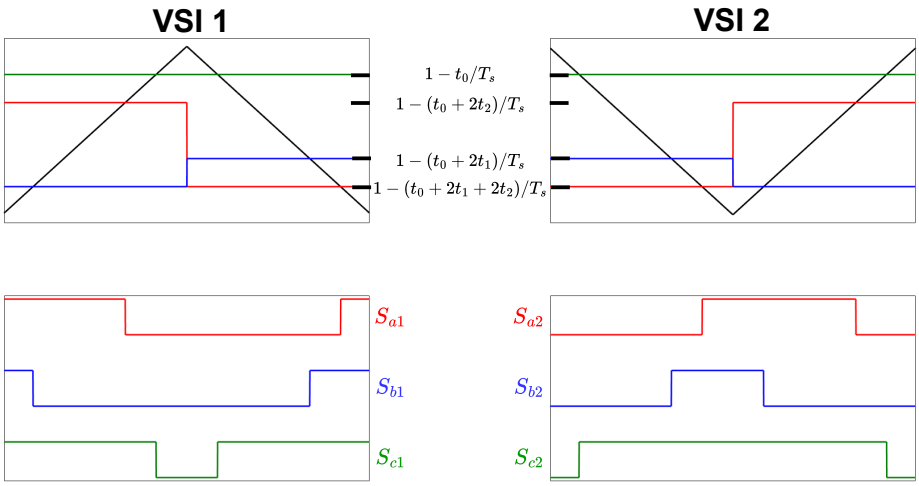

Figure D.4: Sector 5.

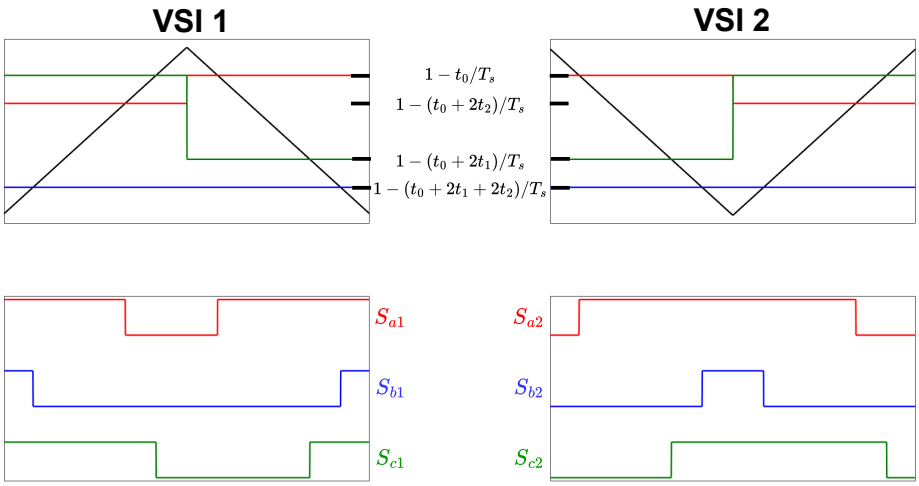

Figure D.5: Sector 6.